International Journal of Polymer Science

Recent Developments in Polymer Composites for Electronic Industries

Lead Guest Editor: Adam Khan M
Guest Editors: Winowlin Jappes JT, Temel Varol, and Madindwa Mashinini

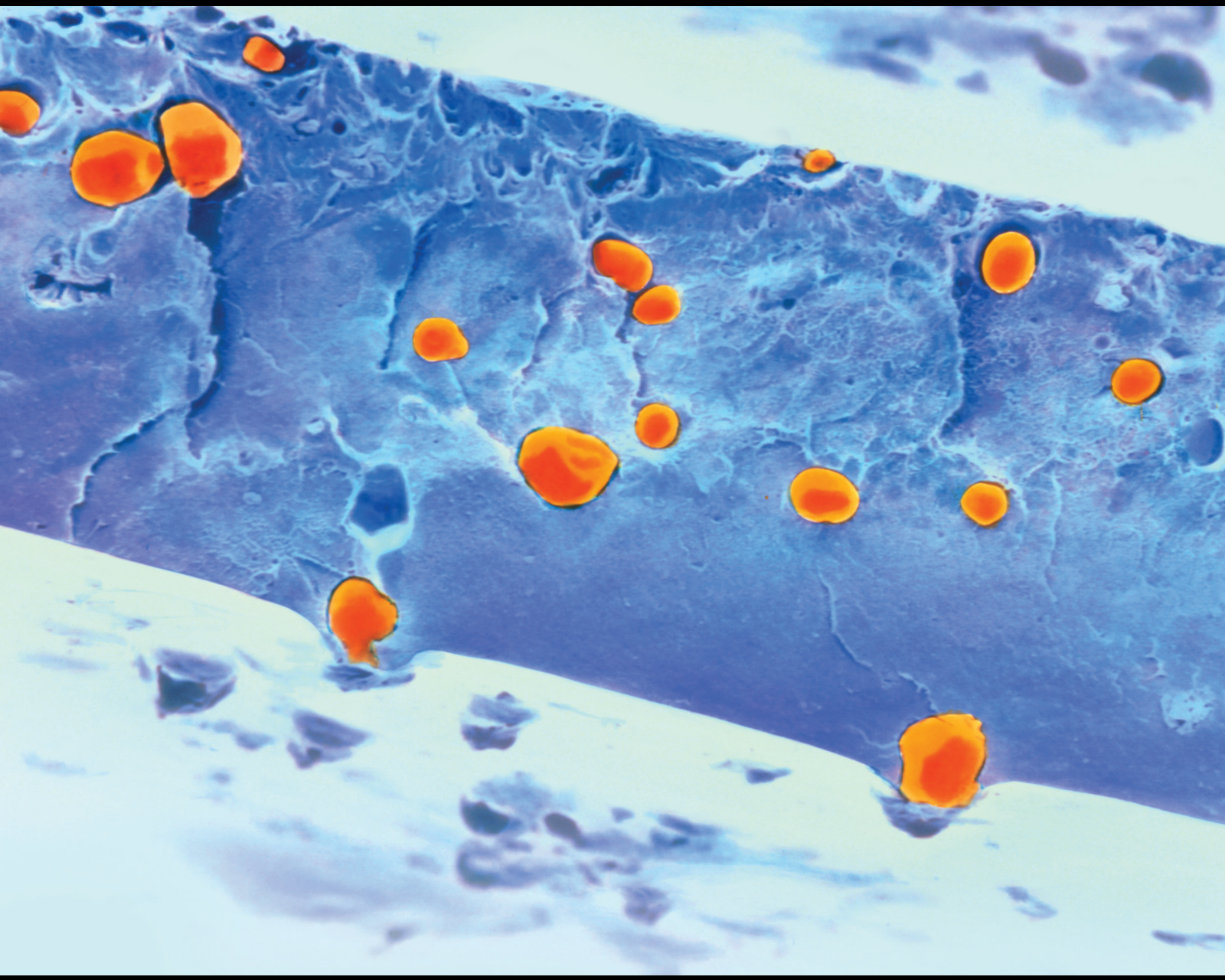

Recent Developments in Polymer Composites for Electronic Industries

International Journal of Polymer Science

Recent Developments in Polymer Composites for Electronic Industries

Lead Guest Editor: Adam Khan M
Guest Editors: Winowlin Jappes JT, Temel Varol, and Madindwa Mashinini

Chief Editor

Academic Editors

Contents

Hindawi
International Journal of Polymer Science
Volume 2023, Article ID 1392115, 8 pages
https://doi.org/10.1155/2023/1392115

Research Article

Design and Fabrication of Metallic-Conductive Polymer-Based Hybrid Film Interconnections for Stretchable Electronic Devices

M. Sucharitha,[1] **Reena Thomas**,[2] **B. Jyothi**,[3] **Edeh Michael Onyema**,[4] **and Gashaw Bekele**[5]

[1]*School of Electronics Engineering, VIT-AP University, Amaravati, Andhra Pradesh, India*
[2]*Noorul Islam Centre for Higher Education, Kumarcoil, Thuckalay, India*
[3]*Electronics and Communication Engineering, Malla Reddy College of Engineering and Technology, Hyderabad, India*
[4]*Department of Vocational and Technical Education, Faculty of Education, Alex Ekwueme Federal University, Ndufu-Alike, Abakaliki, Nigeria and Saveetha School of Engineering, Saveetha Institute of Medical and Technical Sciences, Chennai, India*
[5]*Department of Information System, WOLLO University, Kombolcha Institute of Technology, Kombolcha Post Box No. 208, Ethiopia*

Correspondence should be addressed to Gashaw Bekele; gashaw.bekele@wu.edu.et

Received 8 September 2022; Revised 31 December 2022; Accepted 5 April 2023; Published 29 June 2023

Academic Editor: Adam Khan M

Stretchable circuit is a technological innovation that has transformed the microelectronic landscape due to its enormous applications in the field of medicine. The consistency or durability of health monitoring devices can increase the dependability with which non-invasive clinical measures are collected. Metal–conductive polymer (CP) hybrid interconnects and metal–polyimide dual-layered interconnects were all produced as stretchable interconnections. Stretchable substrate for all of the interconnects was selected as soft elastomer polydimethylsiloxane (PDMS). However, the PDMS substrate presents challenges because it is temperature sensitive, limiting the process temperature. The extreme hydrophobic nature of the PDMS surface makes it difficult to deposit components that contain water and results in poor adhesion with different metals. Following the development of processes for fabricating materials on the PDMS substrate, methods for resolving these issues were investigated.

1. Introduction

Polydimethylsiloxane (PDMS) is a polymer made of SiO $(CH_3)_2$ repeating siloxanes, as a stretchy substrate, as shown in Figure 1. The hydrogen bond formed between both the silanol group on the silica surface and oxygen in PDMS gives it a high adherence to silica [1]. A PDMS solution is spun-coated at 500 rpm for seconds on top of Si to achieve sufficient thickness. It is then dried for 2 hours at 90°C. Before the metal was evaporated with an e-beam, an oxygen plasma treatment was conducted for a brief period. Gold (Au) is ductile, heavily conductive, and insoluble to oxidation, it was selected as the metallic film in this case. To improve adhesion even further, a thin layer of Cr or Ti, i.e., approximately 5 nm, may be evaporated well before Au. Wet etching and photolithography were used to pattern the metallic thin film (MTF). The hydrophobic properties of PDMS substrate are one of the fabrication process difficulties. This PDMS characteristic causes the deposited conductor to adhere poorly. According to Figure 1, the oxygen plasma continues to change the layer of the PDMS substrate by oxidizing CH_3 in the outer chains, and thus changing the PDMS surface from hydrophobic to hydrophilic [2].

Next-generation flexible transparent devices using poly(3,4-ethylenedioxythiophene) (PEDOT): polystyrene sulfonate (PSS) conductive films were developed. However, as a result of defect formation or incomplete layer, electrodes exhibit extremely high mechanical deformation and low electrical conductivity. This is a significant and appealing Conductive Polymer (CP) with unique properties such as outstanding solution fabrication ability and dispersibility, extremely good chemical and electrochemical stability, high and controllable conductivity, good optical transparency, and biocompatibility.

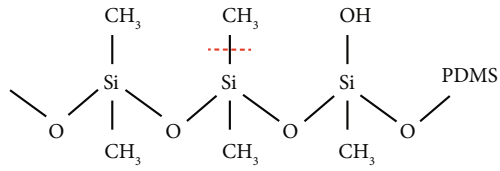

Figure 1: OH-bond to transform PDMS surface.

It is available commercially in organic electronics, including electronic chemosensors.

Annona reticulata dry leaf is used to make negative charge Au and Ag nanoparticles, which are then used to make TF of PEDOT:PSS nanomaterials. The layout and morphological characteristics of nanocomposite vary significantly with respect to the type and concentration of nanoparticles. The complicated PEDOT:PSS CP is the most investigated CP for textile applications. Since this is widely available in dispersion version, which is compatible with existing textile processing applications. Organic Electrochemical Transistors (OECTs) are an adaptable category of biosensing elements because of their sensitivity, potential cost, and system integration benefits. The electrical properties of this electrode are said to be heavily influenced by the film's construction. Out-of-plane longitudinal detachment between adjoining PEDOT domains and mutational reinterpretations in-plane process segregation may occur due to film processing. The operation of OECTs is thickness-dependent, which is explained as how the thickness of the film promotes microstructure tuning all through long-lasting thermal annealing (LTA) in controlled atmosphere. The creation of a PEDOT:PSS polymeric film for use in flat panel displays, control boards, and other optoelectronic is a significant advancement.

New composite materials that display high electrical conductivity and mechanical softness still encounter challenges in terms of chemical degradability, stability, and compatibility with current Micro-electro-mechanical Mystem (MEMS)/ Complementary Metal-oxide-semiconductor (CMOS) technology. Through a variety of methods, this research offers solutions to these problems. Composites are the well-liked choice for stretchable interconnects. It displays greater stretchability and higher electrical conductivity. Their high contact resistance due to the dielectric polymer matrix is one of the disadvantages. The proposed composite includes PEDOT:PSS as the polymer matrix and graphite flakes as the conductive filler to reduce contact resistance and sheet resistance. This composite can provide better stretchability compared to carbon-based composites.

2. Related Works

By integrating polyvinylcycamide with PEDOT:PSS, Ma et al. [3] reported an intrinsically flexible conductive composite film with high electrical properties and minimal damage in challenging environments. It has flexibility properties and substantially improved electrical conductivity. A wearable touch panel device has been fully integrated with the composite film. Gao et al. [4] described the use of PEDOT:PSS and its composite materials in sensors and electrochemical, which detect the presence of gaseous chemical analytes or liquid-phase analytes such as inorganic compounds ions, pH, ammonia (NH_3), hydrogen peroxide, CO_2, CO, NO_2, and organic solvent vapours such as acetone, methanol, and others. The optimization of PEDOT structural, PSS architectural, and morphological properties, as well as composites with other additives, was extensively discussed.

According to Sarkar et al. [5], the examination of shape and film thickness with infrared can demonstrate the films' composite composition. With an increase in nanoparticle concentration, the composite films' in-plane DC conductivity is moderately improved. Electrical responses based on impedance spectroscopic analysis depend on nanoparticle absorption. Structure changes take place after the composite is created. Tseghai et al. [6] developed a method on PEDOT:PSS-based textiles semiconductor, their techniques of implementation in textiles, and their own applications. One method for increasing the mechanical adaptability of CPs is to create a nanoparticle out of common resource polymers with high versatility and stretchability, such as polyurethane. These conductive fibres have been created utilizing solution spinning or electrospinning techniques. And this can be applied to cloth via coating/dyeing, printing, and monomer polymerization. Conductive textiles based on this criterion have been used to make actuators, sensors, interconnections, antennas, storage devices, and energy harvesting devices.

Ji et al. [7] described an innovative organic–inorganic material made of phosphomolybdic acid and PEDOT:PSS as having good solvent corrosion resistance and great hydrophilicity with the printed top Ag nanowires and active layer. Fully coated translucent tools with spray-coated Ag nanowire top electrodes and doctor-blade-coated layers outperformed cells with a thermally evaporated MoO_3 layer in terms of overall performance and Average Visible-light Transmittance (AVT). The highest Power Conversion Efficiency (PCE) was 5.01%, with an outstanding average visible light transmittance of 50.3% (with a PCE of 5.77% and AVT of 19.5%). D'Angelo et al. [8] compared the response of OECTs to LTA with similar channel thickness that had undertaken a quick annealing. This process increased the amplification capacity of OECTs, as demonstrated. The LTA procedure resulted in firmer charge carrier modulation on thinner layers and combined solution processing ability to manipulate the microstructure with the impact of post-deposition processing.

Kleber et al. [9] presented a new transparent hydrogel system composed of the synthesised hydrogel and the CP:PEDOT as a protective coating for brain interfaces. The composite material has the ability to form an interpenetrating network and to be linked covalently with the surface electrodes. It can also be photolithographically shaped just to affect specific electrode places. With the help of the disclosed material, it is feasible to modify the surface of neural probes, combining the advantageous characteristics of conducting polymer hydrogel (CPH) with the superior qualities required for higher quality brain microelectrodes. The effort of Zabihi and Eslamian [10]

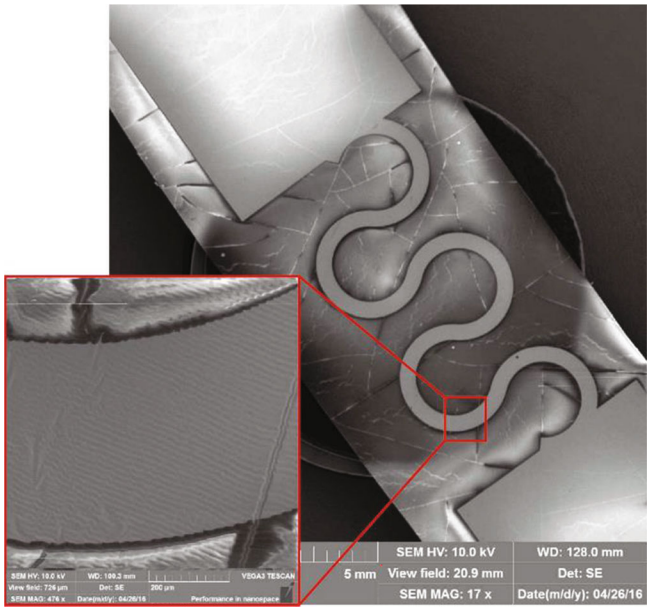

Figure 2: A SEM of a patterned Au interconnect on a PDMS substrate.

to substitute the expensive and restrictive conductive oxides used for the electrodes in Thin Film Diode (TFDs) is demonstrated. The spray-on transparent graphene electrode (TGE) have surface and film coverage and morphological characteristics that are comparable to or superior to PEDOT. A perovskite solar cell with a PCE of 3.54% was used as a proof-of-concept. As contact electrodes for printed organic field effect transistors, Sanyoto et al. [11] used dimethyl sulfoxide (dmso) as a dopant, and the optimum field effect accessibility for diketopyrrolopyrrole-thieno[3,2-b]thiophene organic field effect transistors (DPPT-TT OFET) was $0.49 \times 0.03\,\text{cm}^2$ V.

Kraft et al. [18] proposed a conducting polymer-based ink for flexible interconnections. Wide area handling is flexible, non-invasive, and maskless due to the tunability of inkjet printing paradigm. The imprinted PEDOT:PSS-based interconnections can withstand stresses of more than 100% and have conductivity in the range of $700\,\text{S cm}^{-1}$. Iron (Fe) nanoparticles were used by Zhang et al. [19] as the conducting polymer and polycaprolactone (PCL) as the insulation material for the creation of degradable conducting polymer coatings that made up the interconnects. Under varied degrading settings, the electrical characteristics of the composite were examined. At 17% Fe concentration, electric percolation was seen, while larger content fractions showed more consistent resistance during the duration of physical deterioration. The implementation of chip interconnect by utilizing polymer-based optical waveguides was introduced by Nieweglowski et al. [20]. They offered polymer-based methods for optical connection among waveguides and electronic devices. This strategy relied on bendable substrate with integrated rectangular polymeric optical waveguides. These are investigated as a direct incorporation of polymer waveguides utilizing the dicing technique.

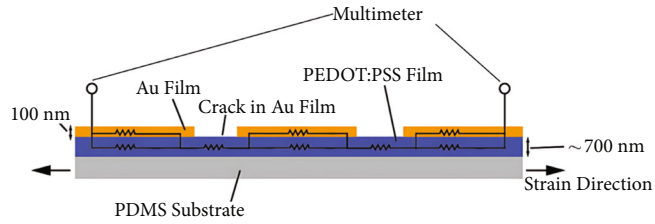

Figure 3: Schematic cross-section view of Au-PEDOT:PSS.

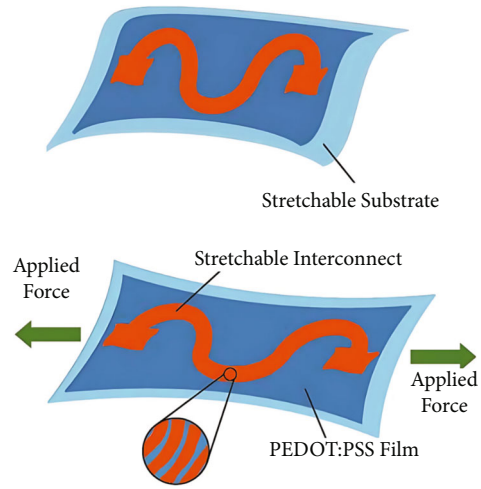

Figure 4: Schematic of strain applied on interconnect with PEDOT:PSS.

3. Materials and Methods

The significant interfacial stress was created between the PDMS substrate and the deposited metallic layer. The metallic coating develops an intrinsic stress during the metal deposition process. This stress tries to release after the film is deposited. The metallic sheet releases the stress since PDMS is a soft substrate, which causes cracks. Deposition rate (DR) is defined as the increment in multi-film thickness (MFT) with respect to the fabrication time. As per the experimental analysis, lower metal DR of 0.4 nm/s can help to reduce internal stress [12]. The DR was therefore marked, and the Au deposited has a thickness of 50 nm. When viewed under a microscope, the density of fissures created within the formed layer dramatically decreased. Plasma treatment based on oxygen over PDMS was examined for varying lengths of time to further enhance the procedure. To protect the moisture, etch of the Au layer, a photoresist surface was used. After a 15-second soak in potassium iodide (KI) solution, the Au was wet inked. A scanning electron microscope (SEM) image obtained using ZEISS GeminiSEM 560 is used to examine the patterned connections as illustrated in Figure 2. Significant folds on the deposited PDMS substrate and Au film can be seen in the highly enlarged SEM image. This surface shape could be attributed to the PDMS substrate's elasticity, which resulted the surface to contract and expand during the metal deposition process [13].

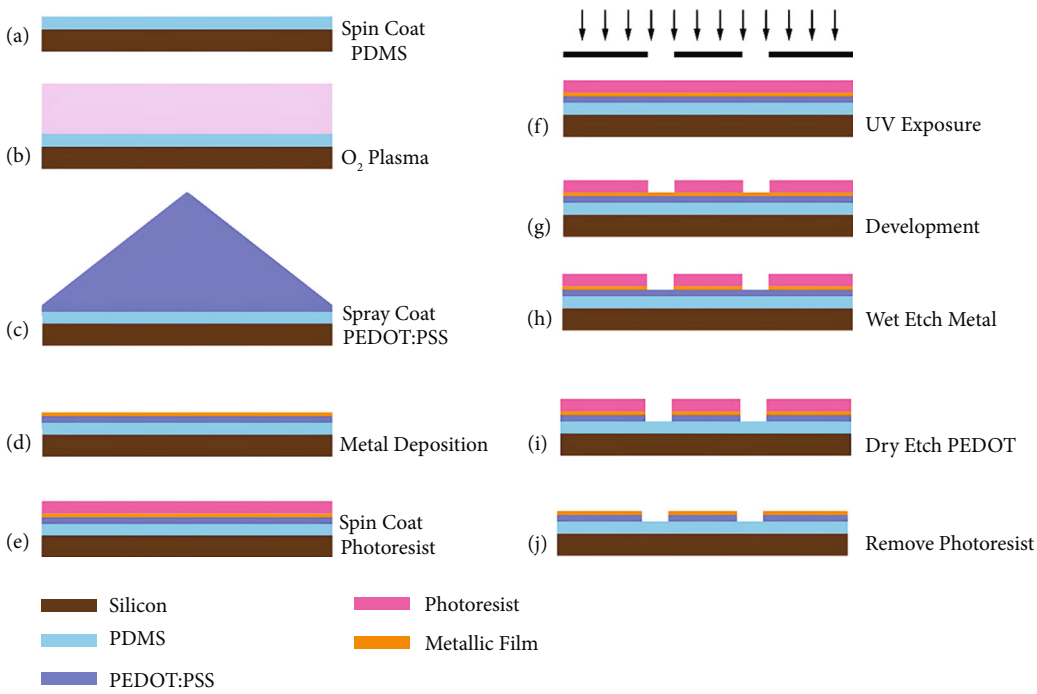

Figure 5: Flow of fabrication process involving spray-coated PEDOT:PSS.

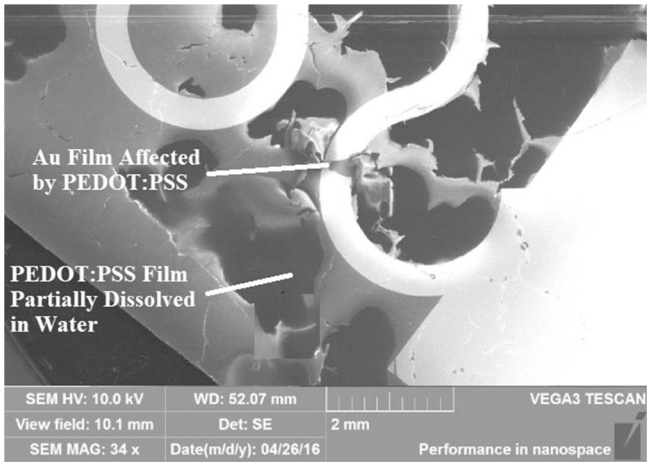

Figure 6: SEM image of fabricated IC with Au film in PEDOT:PSS.

Table 1: Changes in morphology of Ti–Au films under different conditions.

Metal process	Condition	Roughness
Ti–Au (10–50 nm)	O_2 plasma 10 s at 80 W	Rq: 17.3 nm Ra: 14.4 nm
Ti–Au (10–50 nm)	O_2 plasma 30 s at 80 W	Rq: 10.7 nm Ra: 8.9 nm
Ti–Au (10–50 nm)	O_2 plasma 60 s at 80 W	Rq:2.21 nm Ra: 1.75 nm

3.1. Metallic-Conductive Polymer Hybrid Film Interconnects. Soft conductors have been researched as a potential solution to the metallic conductor cracking problem. This film has a moderate electrical conductivity when compared to metallic conductors. Such CPs are also moisture-sensitive, which makes long-term stability difficult. A hybrid construction with metal–CP interconnects was suggested to solve these problems. The metal can perform as a barrier against contaminants as well as enhance the hybrid structure's electrical conductivity. External strain-induced cracks in the top MTF, as shown in Figures 3 and 4, will not surely result in an interruption in the electrical connection. The metallic islands continue to form the electrical conduct path, but they are only loosely connected. HTC Instruments DM-15S TRMS multimeter is used to measure conductivity and resistance.

A conductive polyelectrolyte complex is the PEDOT:PSS. Positively charged PEDOT serves as the conductive component, and the PSS component balances the doping charges and facilitates PEDOT's water dispersion [14]. PSS is good in preventing conductive PEDOT molecules from connecting with one another and reducing the electrical conductivity [15, 16]. The schematic representation of interconnect on a polymer base while applying strain is depicted in Figure 4. Here force is applied from both ends, and the morphology of the interconnect changes without affecting the electrical properties.

3.2. PEDOT:PSS Spray Coating. Figure 5 illustrates the development of spray coating of PEDOT:PSS solution over a substrate of PD. The PEDOT:PSS solution was sprayed using compressed N_2 gas. 5% isopropanol (IPA) was mixed to make it easier to coat the PDMS substrate. 10 seconds of O_2 plasma treatment can significantly increase the angle of contact between the solution and the surface of PDMS. This makes it simpler to spread the PEDOT:PSS over the PDMS substrate. You can run spray coating multiple times to change the PEDOT:PSS thickness of film. Based on the

Table 2: Comparison of morphology change of Au under various plasma conditions.

Metal (50 nm)	Process	Duration	AFM surface	Roughness
Au	No plasma	Nil	Rq: 11.6 nm Ra: 9.5 nm	Rq: 7.65 nm Ra: 3.02 nm
Au	O_2 plasma	10 seconds	Rq: 10.7 nm Ra: 8.9 nm	Rq: 11.4 nm Ra: 10.11 nm
Au	O_2 plasma	20 seconds	Rq: 2.21 nm Ra: 1.75 nm	Rq: 6.52 nm Ra: 6.12 nm
Au	O_2 plasma	30 seconds	Rq: 1.42 nm Ra: 0.98 nm	Rq: 4.42 nm Ra: 6.78 nm

interferometer (Leitz Ergolux) measurement, each spray coating run produces a thick PEDOT:PSS film.

PEDOT:PSS film delaminates and dissolves, as seen in Figure 6. The top Ti–Au coating will be further pulled away from the substrate by the PEDOT:PSS film delamination. 50 nm thick MTF layer is deposited over the polymer layer. A possible solution to this problem is to switch from wet to dry etching of metal, depending on the clean room's capabilities.

Due to its hydrophobicity, the purified PEDOT:PSS that was purchased is difficult to deposit directly on the PDMS substrate because it is dispersed in water. Despite giving the PDMS substrate enough oxygen plasma treatment, the solution has a tendency to separate from the substrate while spinning. Three low-boiling-point solutions were separately combined to help the solution spread uniformly. The PDMS substrates are initially placed on 1.5 cm × 2 cm square-shaped glass slides and exposed to plasma state O_3 for 60 seconds at an intensity of 80 W. Both Au and PEDOT:PSS films are put under a lot of strain during the peeling process, which causes the films to crack even before they are put to the test.

4. Results and Discussions

To further improve the process, an oxygen plasma treatment on PDMS was investigated under varied durations. A comparison between the plasma condition and substrate surface morphology of Ti–Au films has been investigated, as listed in Table 1. Confirmed by atomic force microscopy (AFM) (Nanoscope, Scan Asist Mode, Brucker Icon AFM, U.S) measurement, the surface roughness reduced from 17.3 to 10.7 nm after increasing the duration of oxygen plasma from 10 to 30 seconds. After 60 seconds of exposure, the surface becomes smooth, with a roughness of 2.21 nm. However, the cracks in the resulting film can still be noticed. Observed from an optical microscope, the density of cracks was reduced. The square root of the sum of the squares of the different heights and depths from the mean line (0.5) is defined as root mean square roughness (Rq). The surface's average roughness is termed as Ra.

A further study was conducted to investigate the effect of depositing pure Au layer on top of PDMS. A comparison between the plasma condition and substrate surface morphology for Au films has been investigated, as listed in Table 2. The surface roughness reduced from 11.4 to 6.52 nm after increasing the duration of oxygen plasma from 10 to 30 seconds. After 60 seconds of exposure, the surface becomes smooth, with a roughness of 4.42 nm. No cracks have been observed on all the samples in which the metal was deposited under different plasma conditions [22]. However, under the AFM scanning, the nano-scale cracks can be found. A short time (10 and 30 seconds) plasma does not benefit the Au film to significantly reduce the cracks. 60 seconds of oxygen plasma resulted in a crack-free metallic film on PDMS substrate.

The difference in thickness is visible for all of the samples. The sheet thickness increases with the increase in number of runs through which the polymer material is applied to the substrate. The thickness remains constant at 700 nm and the application process is stopped at that point. The variation in thickness with respect to number of runs is illustrated in Figure 7.

A sheet resistance measurement device is used to gauge the PEDOT:PSS film's sheet resistance. By lengthening the spray runs, the measurement picks up a slight decrease in sheet resistance. The resistance varies between 3000 and 1000 Ohms. As the number of spray runs increases, the resistance decreases. This is an indication of the increment in conductivity of the polymer material used for interconnections. The variation in sheet resistance with respect to spray runs is illustrated in Figure 8.

After accounting for the thickness and sheet resistance measurements, it can be noted that the developed polymer material is well suited for the development of interconnects. Figure 9 shows the optical image of a sprayed 700 nm thick PEDOT:PSS film on a PDMS substrate obtained using Celestron TETRAVIEW 5MP digital microscope. It has a resistivity of about 0.0072 Ohm metre.

Figure 10 shows the fitted curve values vary greatly (standard error). This could be due to the probe's shaky interaction with the specimen surface. Since the sample's surface is soft, the metallic probes had no problems penetrating it [17]. The resistance of Pristine PEDOT:PSS varies from 1270 to 3300 Ohm, when the distance between the interconnects is varied from 10 to 30 mm.

Meanwhile, the AFM measurement was used to find morphology [21]. The doped-graphite powder effect increased the surface roughness. About 8.5 nm of depth and as a result is an increase in overall roughness from 3.84 to 6.31 nm. The electrical characteristics of composite were carried out with the help of an I–V characteristics probe station. The transfer line measurement (TLM) is used to measure the sheet resistance and contact resistance. As shown in Figure 10, proposed polymer-based interconnect provides better linear fitting for resistance respect to the varying distance when compared to un-doped PEDOT:PSS film [23].

The polymeric composite design benefits from both the fillers' high conductivity and the polymers' softness [24]. It displays a high elastic modulus, but the majority of polymers, which are also soft and supple like human skin which are insulating. When compared to its metallic equivalent, the polymer connector has less roughness. In comparison to metallic interconnects, such polymer composites

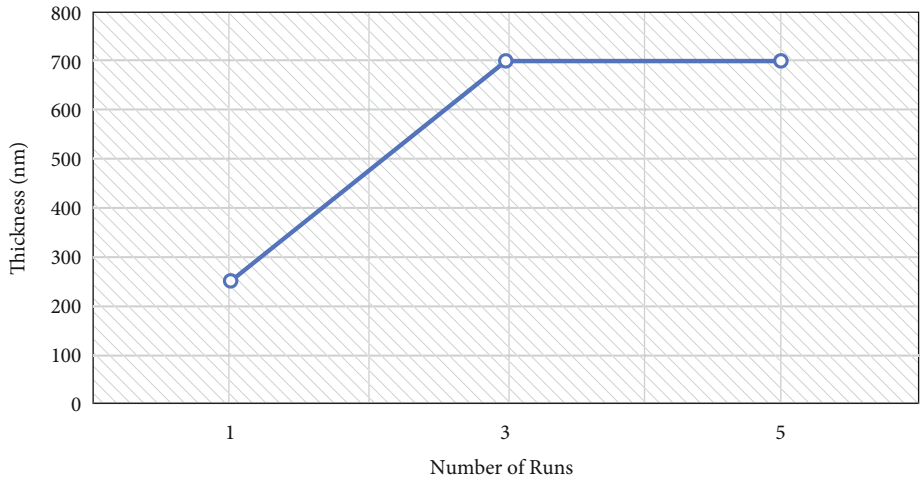

Figure 7: Thickness measurement.

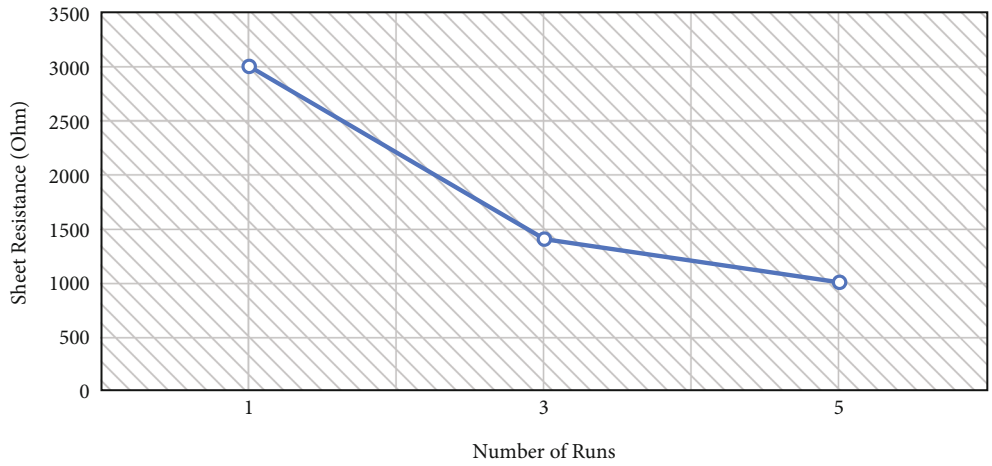

Figure 8: Sheet resistance measurement.

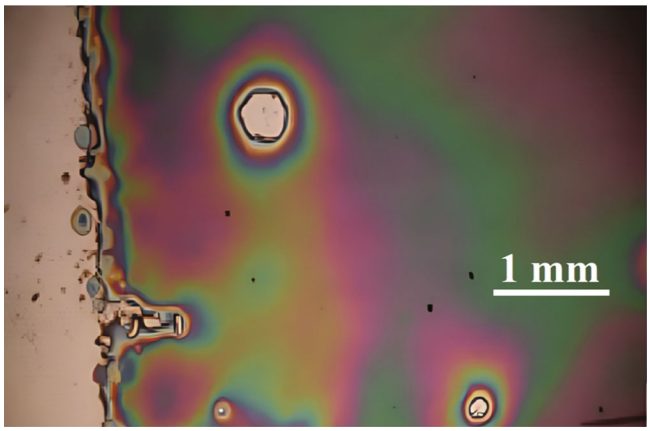

Figure 9: Optical image of PEDOT:PSS on PDMS substrate.

have higher stretchability values. As distance increases, the interconnection's resistance changes continuously [25]. Due to their availability, higher conductivity, and cost-effectiveness, polymers are frequently employed as conductive fillers. However, in practice, bigger conductors are more expensive, and manufacturing technologies also have a limit on how thick they can be. The fabrication approach increases the polymer interconnects' durability while being very cost-effective.

5. Conclusion

This paper discussed the fabrication of polymer-based stretchable interconnects using various conductive materials. As a substrate for all types of interconnects, the elastomeric polymer PDMS was used. Au films have long been employed in conventional electronic devices as standard conductors. To deposit 50 nm MTF on soft substrates, an optimized fabrication process was developed. Microfabrication technology is used in the procedures. Resolution (up to 5 m), flexibility, and reproducibility are all advantages of these processes. Spin coating provides solution for uneven thickness on PDMS substrate. In order to create a hybrid conductive film, a second metallic layer was to be deposited on the PEDOT:PSS film. As a result, manufactured interconnect resolution falls short

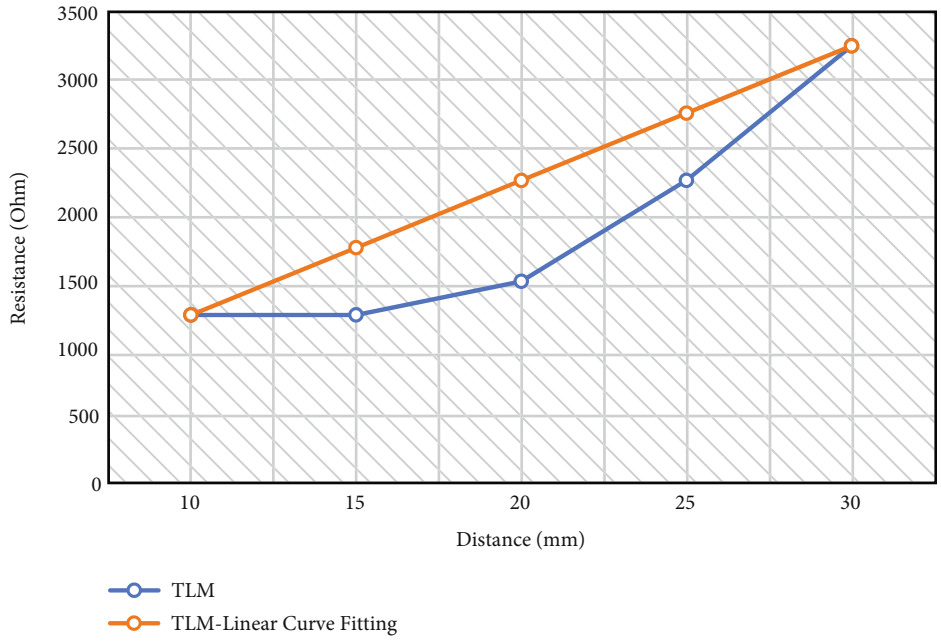

Figure 10: Measurement results with TLM-linear curve fitting.

of that of microfabrication. To enhance the resolution and flexibility of composite-based interconnect fabrication, the screen-printing process is being improved. The polyimide must undergo etching in O_2 plasma setting as well as to wet etching the pattern metal layer. As the interconnects must be transmitted from such a carrier semiconductor to polymer substrate, the fabrication process becomes much more complicated. The synthesis of composite-based ink for screen printing interconnections is a future goal. Screen printing cannot be performed using the present PEDOT:PSS composite. On the basis of the composite's encouraging electromechanical responses to strain, more advancements in size reduction are envisioned. The integration of stretchy interconnects with multiple sensor modulus in a greater sensing density is another goal of future research. The sensors are now integrated separately, which takes a lot of time and makes the procedure less reproducible. For the integration of various sensors, the more efficient approach needs to be investigated.

Data Availability

Data supporting this research article are available from the corresponding author or first author on reasonable request.

Conflicts of Interest

The authors declare that they have no conflicts of interest.

References

[1] L. Yu, *The Adhesion of Poly(Dimethylsiloxane) to Silica Substrates*, Master of Applied Science Thesis submitted to Department of Chemical Engineering, MC Master University, Canada, 2014, https://hdl.handle.net/11375/15402, Accessed 10 July, 2022.

[2] B. Miliare, M. Thomas, A. Ferreira, H. Xu, M. Holesinger, and V. I. Vullev, "Dependence of the quality of adhesion between poly(dimethylsiloxane) and glass surfaces on the conditions of treatment with oxygen plasma," *Langmuir*, vol. 24, no. 22, pp. 13218–13224, 2008.

[3] C. Ma, H. Luo, M. Liu et al., "Preparation of intrinsic flexible conductive PEDOT: PSS@ ionogel composite film and its application for touch panel," *Chemical Engineering Journal*, vol. 425, article 131542, 2021.

[4] N. Gao, J. Yu, Q. Tian et al., "Application of PEDOT: PSS and its composites in electrochemical and electronic chemosensors," *Chemosensors*, vol. 9, no. 4, p. 79, 2021.

[5] S. Sarkar, A. C. Bhowal, R. Kandimalla, and S. Kundu, "Structural and electrical behaviours of PEDOT: PSS thin films in presence of negatively charged gold and silver nanoparticles: a green synthesis approach," *Synthetic Metals*, vol. 279, article 116848, 2021.

[6] G. B. Tseghai, D. A. Mengistie, B. Malengier, K. A. Fante, and L. Van Langenhove, "PEDOT: PSS-based conductive textiles and their applications," *Sensors*, vol. 20, no. 7, p. 1881, 2020.

[7] G. Ji, Y. Wang, Q. Luo et al., "Fully coated semitransparent organic solar cells with a doctor-blade-coated composite anode buffer layer of phosphomolybdic acid and PEDOT:PSS and a spray-coated silver nanowire top electrode," *ACS Applied Materials and Interfaces*, vol. 10, no. 1, pp. 943–954, 2018.

[8] P. D'Angelo, G. Tarabella, A. Romeo et al., "PEDOT: PSS morphostructure and ion-to-electron transduction and amplification mechanisms in organic electrochemical transistors," *Materials*, vol. 12, no. 1, p. 9, 2019.

[9] C. Kleber, M. Bruns, K. Lienkamp, J. Rühe, and M. Asplund, "An interpenetrating, microstructurable and covalently attached conducting polymer hydrogel for neural interfaces," *Acta Biomaterialia*, vol. 58, pp. 365–375, 2017.

[10] F. Zabihi and M. Eslamian, "Low-cost transparent graphene electrodes made by ultrasonic substrate vibration-assisted spray coating (SVASC) for thin film devices," *Graphene Technology*, vol. 2, no. 1, pp. 1–11, 2017.

[11] B. Sanyoto, S. Kim, W. T. Park et al., "Solution processable PEDOT:PSS based hybrid electrodes for organic field effect transistors," *Organic Electronics*, vol. 37, pp. 352–357, 2016.

[12] S. Tinku, E. Iacob, L. Lorenzelli, and R. Dahiya, "Surface characterization of polydimethylsiloxane: an AFM study," *2015 XVIII AISEM Annual Conference*, pp. 1–4, Trento, Italy, 2015, https://ieeexplore.ieee.org/document/7066787.

[13] S. J. Yu, Y. P. Du, Y. D. Sun, Q. L. Ye, and H. Zhou, "Wrinkling patterns in metal films sputter deposited on viscoelastic substrates," *Thin Solid Films*, vol. 638, pp. 230–235, 2017.

[14] S. Timpanaro, M. Kemerink, F. J. Touwslager, M. M. De Kok, and S. Schrader, "Morphology and conductivity of PEDOT/PSS films studied by scanning-tunneling microscopy," *Chemical Physics Letters*, vol. 394, no. 4–6, pp. 339–343, 2004.

[15] X. Crispin, F. L. E. Jakobsson, M. Berggren, and E. Al, "The origin of the high conductivity of poly(3,4-ethylenedioxythiophene)-poly(styrenesulfonate) (PEDOT–PSS) plastic electrodes," *Chemistry of Materials*, vol. 18, no. 18, pp. 4354–4360, 2006.

[16] D. J. Lipomi, J. A. Lee, M. Vosgueritchian, B. C.-K. Tee, J. A. Bolander, and Z. Bao, "Electronic properties of transparent conductive films of PEDOT:PSS on stretchable substrates," *Chemistry of Materials*, vol. 24, no. 2, pp. 373–382, 2012.

[17] T. Takano, H. Masunaga, A. Fujiwara, H. Okuzaki, and T. Sasaki, "PEDOT nanocrystal in highly conductive PEDOT:PSS polymer films," *Macromolecules*, vol. 45, no. 9, pp. 3859–3865, 2012.

[18] U. Kraft, F. Molina-Lopez, D. Son, Z. Bao, and B. Murmann, "Ink development and printing of conducting polymers for intrinsically stretchable interconnects and circuits," *Advanced Electronic Materials*, vol. 6, no. 1, p. 1900681, 2020.

[19] T. Zhang, M. Tsang, D. Lin, M. Kim, and M. G. Allen, "Electrical interconnects fabricated from biodegradable conductive polymer composites," *IEEE Transactions on Components, Packaging and Manufacturing Technology*, vol. 9, no. 5, pp. 822–829, 2019.

[20] K. Nieweglowski, L. Lorenz, S. Lüngen, T. Tiedje, K.-J. Wolter, and K. Bock, "Optical coupling with flexible polymer waveguides for chip-to-chip interconnects in electronic systems," *Microelectronics Reliability*, vol. 84, pp. 121–126, 2018.

[21] S. Gupta, W. T. Navaraj, L. Lorenzelli, and R. Dahiya, "Ultra-thin chips for high-performance flexible electronics," *npj Flexible Electronics*, vol. 2, no. 1, p. 8, 2018.

[22] Y. Yao, H. Dong, and W. Hu, "Charge transport in organic and polymeric semiconductors for flexible and stretchable devices," *Advanced Materials*, vol. 28, no. 22, pp. 4513–4523, 2016.

[23] Y. Hou, D. Wang, X.-M. Zhang, H. Zhao, J.-W. Zha, and Z.-M. Dang, "Positive piezoresistive behavior of electrically conductive alkyl-functionalized graphene/polydimethylsilicone nanocomposites," *Journal of Materials Chemistry C*, vol. 1, no. 3, pp. 515–521, 2013, no. March.

[24] I. Moreno, N. Navascues, M. Arruebo, S. Irusta, and J. Santamaria, "Facile preparation of transparent and conductive polymer films based on silver nanowire/polycarbonate nanocomposites," *Nanotechnology*, vol. 24, no. 27, p. 275603, 2013, (1–11).

[25] K. K. Kim, S. Hong, H. M. Cho et al., "Highly sensitive and stretchable multidimensional strain sensor with prestrained anisotropic metal nanowire percolation networks," *Nano Letters*, vol. 15, no. 8, pp. 5240–5247, 2015.

Hindawi
International Journal of Polymer Science
Volume 2023, Article ID 9645190, 9 pages
https://doi.org/10.1155/2023/9645190

Research Article

Reinforcement of Nanocellulose as Green Agent in the Electronic Applications Associated with the Composites of Polymer Matrix

Manjunathan Alagarsamy,[1] S. R. Barkunan,[1] N. Jayapal,[2] A. Murugan,[3] P. Muralikrishnan,[4] and Perumalla Janaki Ramulu[5]

[1]*Department of Electronics and Communication Engineering, K. Ramakrishnan College of Technology, Trichy, Tamil Nadu 621112, India*
[2]*Department of Electronics and Communication Engineering, Kongunadu College of Engineering and Technology, Trichy, Tamil Nadu 621215, India*
[3]*Department of Electronics and Communication Engineering, M. Kumarasamy College of Engineering, Karur, Tamil Nadu 639113, India*
[4]*Department of Electronics and Communication Engineering, K. Ramakrishnan College of Engineering, Trichy, Tamil Nadu 621112, India*
[5]*Department of Mechanical Engineering and Center for Advanced Manufacturing Engineering, Adama Science and Technology University, Post Box 1888, Adama, Oromia State, Ethiopia*

Correspondence should be addressed to Perumalla Janaki Ramulu; perumalla.janaki@astu.edu.et

Received 23 July 2022; Revised 20 September 2022; Accepted 8 October 2022; Published 19 April 2023

Academic Editor: Temel Varol

Due to their profusion, high durability, and rigidity, lesser weight and biodegradable nature nanocellulose (NC) is observed as the challenging tasks for the aspirants in making of the green composites. The continuous network of the cellulose nanoparticle connected through hydrogen bonding is happened mainly due to the reinforcing effect allocated to the mechanical reoccurrence phenomenon of the NC. When comparing with the nanocrystalline cellulose, the NC has significant convincing progress in the durability and rigidity, and the aspect ratio of the NC is higher than that of the NC crystal. The reinforcement effect of NC is the characteristic of the NC polymer interaction as well as the reinforcement effect eventualizing through stress transfer at the NC–polymer interface. Thus, the concentration of the reinforcement particle rises to the saturation level due to the frailty of the NC reinforcement constituent and due to surface compliance between the matrix and the filler. Due to its structural firmness and mechanical behaviors, the NC compounds are used in many industrial applications like tissue engineering, food packaging, and electronic applications. The stretchable electronic systems and instruments are awaiting the maximal attention due to its essential applications in certain domains, such as robotics artificial intelligence, brain control and machine interface, clinical devices, and health care electronic monitoring devices. In addition to that, when realizing the operational performance of electronic devices, the electronic instruments and systems must be physically expandable and flexible. The proposed study deems the technique of reinforcing the NC compounds as green agent in electronic applications, which has been associated with the composites of polymer matrix. The elongation could be achieved through the formulation of composition via elastomers. In addition, it is being focused on the illustration of functional soft development of materials that is inclusive of the conductive intrinsic polymers for the elongated electrodes and electrothermal conversion and vice versa, occupying the maximal area along with tactile sensing elements.

1. Introduction

Due to the environmental agitation, reduction in fossil resources, and rise in the manufacturing cost of the synthetic polymer material, many researchers are aiming to work on the biocomposite. Basically, green polymeric composites are environmentally safe, completely degenerative, and maintainable. The growth of green polymer composite would evade

Table 1: Summary of nanocellulose-essential and capable-trendy applications.

Essential nanocellulose features	Applications	Properties
Nanofiber cellulose (NCF)	Sectional automatic interiors	Maximal tensile strength
	Antireflective-coated films	Better dispersion
	Substrates to determine the activity of cellulose	Equal competence to real time cellulose substance
	Material reinforcement in polymeric vector substance	Maximal strength
Nanocrystalline cellulose (NCC)	Reinforcement of paper	Minimal toxic behavior
	Adaptive and controllable delivery of drug	Maximal aspect ratio
	Applications in biomedical imaging	
	Applications in various domains of electronics	
Nanobacterial cellulose (NBC)	Bioclinical applications	Minimal toxic to a cell membrane
	Artificial layered skin	Very pure substance
	Binder in the production of paper	Peak modulus and peak crystalline envelope
	Optically characterized opaque film	Maximal peak hydrophilicity

the disposal limitation of the plastic polymer composites. This method is proven very tedious and profitless, and it provides a bad impact on the environment [1]. Several non-renewable resources are needed for the manufacturing of the plastic component. The reinforced cellulose derivative is present in the green polymeric component due to this nature that it is capable of gaining improvement in the mechanical and electrical properties as well as the biodegradability of the polymeric substance, leading to the rise in the mechanical nature of the substance, less density, and presence of the cellulose component. Compared to the inorganic mineral, they have less bonding effect and are also best suited to produce less specific weight. With the change in the chemical nature associated with the degradation of the polymer, it might occur with the changes in the composition of the green composites [3]. Thus, leading to the drop in the structural and mechanical properties and reformation of the substance, it tends to do favor for the environment. The green polymeric components are used in many applications, such as production of the large number of products with minimal life process or the product, which are used once preexisting to dispersal [2]. The foremost step to be carried in improving the interfacial adherence between different components is that modifying the cellulose as reinforcement agent as well as the polymer matrices, leading to the augmentation of the mechanical, barrier, and the resistance nature. With the methods of dewaxing, acetylation, silane treatment, and peroxide treatment, the modification of the surface is done [4]. Therefore, to improve the mechanical strength and the reinforcement effect of the polymeric composite development of the nanocomposites is main task. Nanocomposite comprises the nanosized reinforcement element, having a dimension of 100 nm. Knowing the biological origin acquirement of the nanoelement from the various renewable resources is possible. These nanocomposites and green composites have a distinct property [5].

1.1. Nanomaterial-Multifunctional Nanocellulose. Cellulose is considered one of the most important polymers on the earth. The cellulose has the following properties that it does not have color and smell, and it is a non-toxic polymer, with high mechanical property, hydrophilicity, biocompatibility, high absorption capacity, and changeable optical appearance [6]. The cellulose does not exist in an isolated manner and is formed by the group of cellulose chain producing fibers. Due to the wider intensity of the OH bond in the structure, there exists the hydrogen bond in the structure. The morphological hierarchy is also called as the elementary fibrils, and they are combined into a larger unit called microfibrils later and are modified into a fiber structure. In the cellulose structure, various regions are formed; the highly ordered regions are called as crystalline and the disarranged order amorphous [7]. The nanocellulose (NC) structure is obtained from the extraction of the crystalline structure. Thus, the obtained nanoparticle may vary in size range having a diameter of 5–30 nm and with the length of 100–500 nm, or the length may vary from several micrometers. The nanoparticle is an elongated rod-shaped structure, they are composed of nanoparticles, and the single rod is considered as the rigid cellulosic crystal [8]. The best quantified NC is used in various applications. The lists over the trendy and essential NC applications are shown in Table 1. The various forms of the NC are opaque films, paper, hydrogels, aerogels, and sphere-shaped particles [9].

2. NC Synthesis Process

Figure 1 depicts the procedure incurred for the production of the NC. The NC is produced by the use of hydrolysis process, with the cellulose material under specific time, temperature, and agitation. The NC preparation includes the following aspects, that is, the ratio of the acid to cellulosic fiber to that of the nature of the acid [7]. The dimension of the NC is defined mainly by the origination of the cellulose; it also depends on the acid species, acid concentration, time, and temperature acquired for the hydrolysis process. Dialysis process is carried toward the distilled water in order to prevent spreading of the free acid molecules [10]. Depending on the origin of the cellulose fiber, specified hydrolysis process and separation process are performed. The rod-like nanoparticle may have size range of about 5–20 nm, and it may also vary from 100 nm to numerous micrometers, respectively [11]. The process, such as dissolving, catalyzing,

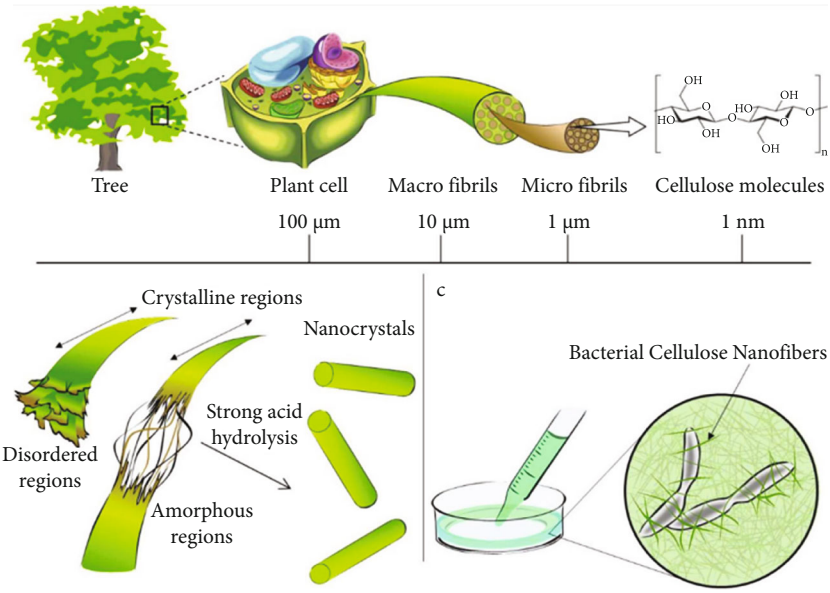

Figure 1: Traditional technique in synthesizing nanocellulose in the form of crystals [7].

and hydrolysis of cellulose, is carried by the usage of the ionic liquid. The newer version of the ionic liquid has been discovered; it is composed of the hydrogen bond donor molecule with that of the halide salts.

2.1. NC Property and Its Applications. The characteristics of the NC may differ from that of the classical material with regard to its morphology, geometric dimension, high specific surface area, alignment, orientation, and toxicity. It has the physical property merely the same as that of perfect crystals. The crystalline nature of NC provides no pattern of chain folding. The strength and the modulus are given by 7 and 140–150 GPa, respectively [12]. From the architectural representation, NC comprises the homopolysaccharide with β -1,4 anhydro-D-glucopyranose unit with varying hydroxyl groups 101 and 102. The OH groups are helpful in the formation of the hydrogen bond, and it plays a key role in the production of the semicrystalline packing and fibrillary, which reigns the objective of the cohesive component. Therefore, to perform surface functionalization, the OH groups are awarded with NC having various reactive surfaces. The NC is considered less toxic [13, 14].

3. Reinforcement in Composite System

The measurable effects are produced by adding the rigid particle with that of polymer material namely increased stiffness, depletion in the thermal expansion coefficient, and rise in the creep resistance and fracture toughness [15].

3.1. Principle and Theory. The factors that affect the mechanical behaviors of the components are its size, shape, and the aspect ratio. While determining the mechanical property of the non-spherical NC, the following parameter to be considered is its orientation with respect to its applied stress. Likewise, with the variation in the shape of the particle, the mechanical performance of the reinforced polymer gets affected [16]. This effect mainly occurs in the non-spherical shaped NC composite. Hence, several studies proved that the crystal structure of the NC produces better reinforcement comparative to that of the fiber-shaped structure [17]. The various compositions of the nanoparticle are arranged very densely compared to the monodispersed nanoparticle, thus leading to the formation of the agglomerates. Therefore, to yield larger moduli, the aggregated particle transfers large sum of load comparative to that of the primary particles [18]. NC particle is composed of multiple hydroxyl groups that stimulate both the physical and chemical relationships between the matrices and the NC, thus resulting in rise in the strength of the material. The strength and the stiffness of the material are increased by its dispersion quality.

3.2. Reinforcement of the NC in Synthetic Polymer Composites. The reinforcement effect of NC is distinguished by its crystalline and amorphous nature. The cellulose chain in the crystalline region accords to the stiffness and elasticity of the material, whereas for the amorphous region, it bestows to the plasticity and elasticity in case for the bulk material. The coefficient of the NC is obtained by the combination of the amorphous and crystalline domain. The wet NC is used to get better mechanical property of the material.

3.3. Performance of Mechanical Properties over the NC/Epoxy Composites. Epoxy components are generally malleable, and they get break down at large stress and strain. Basically, the strength and the coefficient of the material get raised by addition excess weight of about 0.3–0.6%. This growth is mainly due to the reunion of the epoxy component. The capacity of the epoxy composites is mainly dependent on the strength and the stiffness of the material. If the epoxy reunion gets poor, there arises a problem in carrying external load. There occurs an excitement between the NC and the epoxy when the bonding between them gets stronger. This, in turn, increases the coefficient of the composite. When the required

amount quantity of the NC is added to the saturated volume, it ends with poor stresses and strains. Due to intermodular forces, NC usually forms bundle of aggregates having the aspect ratio less than the discrete dispersal particle. The surface functionalization is registered to increase the wettability of the NC facet. This leads to raise in interfacial interaction between the epoxy composites, whereas the salination of the NC decreases the nature of the brittleness of the composites, thus leading to betterment in the coverage of the NC; at the higher temperature, the reinforcement effect is achieved. Grafting helps in improving the dispersion of the NC in the epoxy matrix. The toughness nature is persuaded by the hyperbranched polymer structure because of the wide interaction between the composites.

3.4. Performance of Mechanical Properties over NC Polyurethane Composites. The polyurethane material basically has high flexibility and high deformation property. The mechanical behaviors of the polyurethane are affected by adding NC at when the strain at the break decreases Young's modulus and the strength of the certain levels. The coefficient of the polyurethane is grown by 253% by adding 4 wt% filler. Composites get increased, leading to the increase in the NC in the form of fiber and crystals. The strong interfacial bonding occurs with the rise in the tensile strength. When comparing with NCC to that of NCF, NCC has much higher tensile strength because of the emergence of the interconnected network. The origination of the interconnected cellulose network tends to rise in the increased filler content. The emergence of network in NC is attributed to the flexibility as well as the aspect ratio. It leads to reunion of the NCF and polyurethane as they avoid the movement of the polymer chain, which results in high strength and high numerical coefficient value. Due to the flexible nature of the NCF, there is an occurrence of several inter hydrogen bonds. The physical reunion occurred mainly due to hydrogen bonds. This tends to influence the mechanical behaviors of the composites [19]. The formation of hydrogen bond takes place with the HS and SS of the urethane group. The hydrogen bonds form when linking the polyurethane molecule and NC. With the addition of the NC to that of the NC polyurethane, the viscosity gets increased.

3.5. Performance of Mechanical Properties over NC Polyester Composites. The tensile strength of the polyester composite is between 831 and 987 MPa. This occurs with the addition of 6 wt% of the NC. Further adding NC with the polyester matrix has given rise to the tensile strength with the 10% of 4 wt% filler loading. The tensile strength increases because of the reduced volume fraction of the polyester component. When disputing the mechanical property of the composites, the acquirement of the NC interconnections bond is being obtained. These networks are capable of enacting as a load bearing component.

3.6. Mechanical Performance of NC Polyethylene Composites. With the addition of filler, the gradual increase in the strength and the Young's modulus is obtained by the polyethylene composites. Thus, this increment in these parameters says there is no variation between the NCC and the NCF. The rigidity of the NC comes up with the decrease in the elongation of breakup.

3.7. Reinforcement of NC in Biopolymeric Composites. The main phenomenon to be considered for achieving best mechanical property of the composite is good interfacial interaction and stress transfer within NC and polymer matrix. NC may best accompany with the aqua; hence, biopolymer matrix is best suited for the dispersion process. The selection of the biopolymer is one of the main aspects in this process.

3.8. Mechanical Aspect of NC Polyvinyl Alcohol Composites. The tensile strength of the polyvinyl alcohol may be 73 MPa. The tensile strength of the NC is increased by 3–5%. The mechanical property of the composite is increased by the intermolecular force between the NC and the polyvinyl alcohol. The reduction in the dispersion of the composite leads to the reduction in the tensile strength of the composite [20, 21].

3.9. Mechanical Performance of NC Gold Polyvinyl Alcohol. The existence of the polyvinyl alcohol on the base of the NC tends to increase the ductile nature of the composite. The crosslink is formed between the NC and the gold polyvinyl alcohol due to the presence of the gold particle on the NC, thus leading to the formation of the better polymer chain with increased strength and the coefficient value.

3.10. Performance of Mechanical Properties over NC Epoxy Polyvinyl Alcohol Polyacrylamide Composites. When there is less bonding between the NC, this poly acrylamide is capable of producing better tensile strength. The process of synthesizing a minimal quantum of graphene oxide has been depicted in Figure 2(a), and its formulation of nanocomposite film has been depicted in Figure 2(b). The hydrogen bonding takes place at all of these places with the presence of the NC. This hydrogen bonding takes place between the NC and the polymers. The chain mobility gets decreased due to this effect.

3.11. Mechanical Performance of Chitosan Composites. Chitosan has been used in lot of studies due to its composition; it has 1–5 wt% with the tensile property of NCF, having the young modulus of about 150% and with the composition of NCF of 12.4%. There are two factors involved in this process: one is interaction of the polymer with the nanocrystal and the other is the reinforcement effect. The interfacing of matrix and the filler is best carried with the anionic sulfate group of the NCF and the cationic group of chitosan, whereas with the composition of 12.4 wt%, NCF is not much suitable to perform the strengthening of the tensile strength. The tensile strength has been increased from 85 to 120 MPa with the gradual rise in the filler component of about 0–20 wt%. Thus, elongation at break is decreased from 20 to 6 wt%. If the component containing more than 20% of NCC, then there is a decrease in the tensile strength as well as the elongation at break point. The illustration of polyacrylamide scheme characterized with cross-linked structure has been depicted in Figure 3.

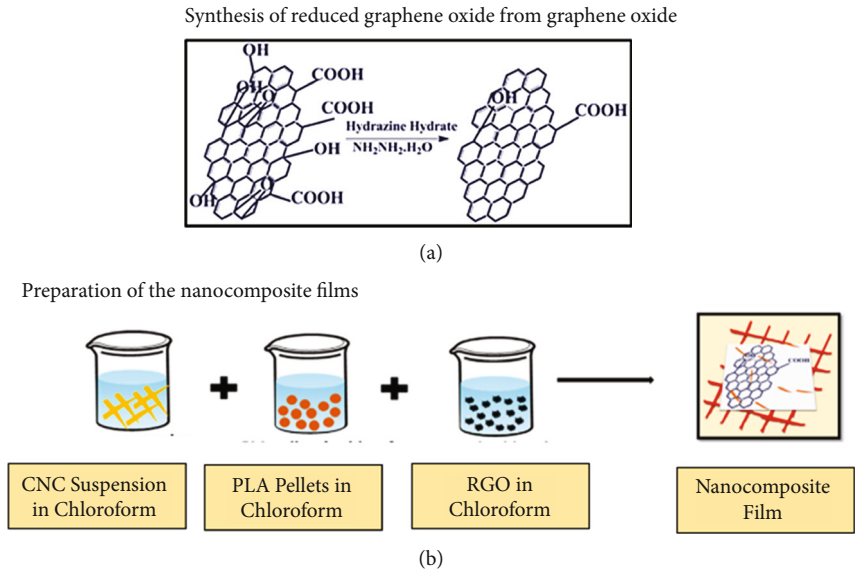

Figure 2: (a) Synthesizing of minimal quantum of graphene oxide and (b) nanocomposite film formation.

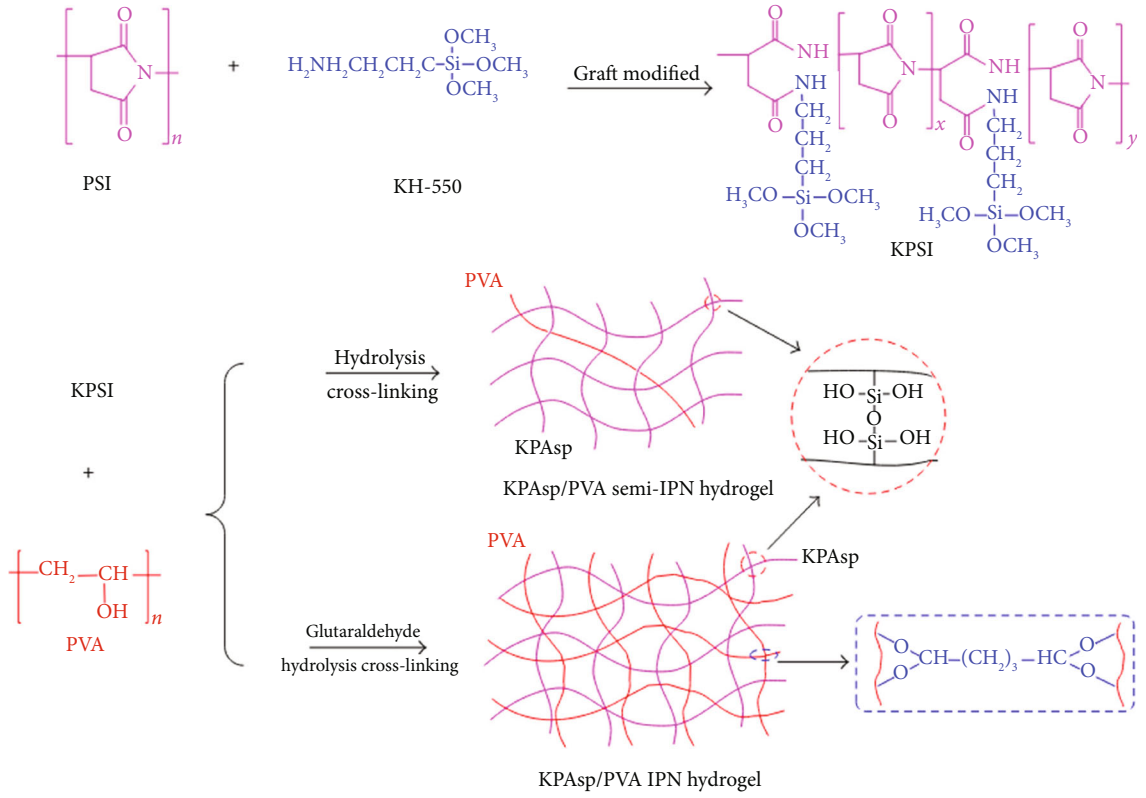

Figure 3: Illustrating the scheme of polyacrylamide characterized with cross-linked structure [20].

3.12. Mechanical Performance of NC Starch Component. Due to poor mechanical property and high hydrophilic nature, the starch-based film is not much used in several applications. The coefficient of the starch film and the tensile strength gets increased from 7.689 to 1.575 MPa, whereas the tensile strength gets increased from 7.629 to 1.515 MPa, respectively. The NCF and starch contain hydroxyl group that are capable for the formation of the hydrogen bond within the NCF chain and the starch chain.

3.13. Mechanical Performance of NC/Polycaprolactone Composites. In the room temperature, this component is mostly ductile and exhibits less elastic coefficient. In addition, NC of up to 12% leads to rise in tensile strength and

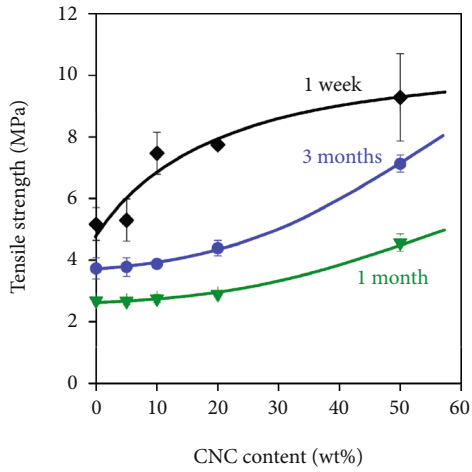

Figure 4: Characteristics over the physical and mechanical properties of CNC content across tensile strength.

reduction in strain at break [22]. This rise leads to hardness of the NC. The NCF and starch contain hydroxyl group that are suitable for the formation of the hydrogen bond.

3.14. Reinforcement of NC in Rubbery Composites. The stress–strain curve of NC composites exhibits similar fashion. Having less NC content, the rubbery material exhibits the non-linear behavior. The NBR chains are formed due to rigidity and highly crystalline nature. The composite material constitutes both the rubbery material and the NC. The characteristics over the physical and mechanical properties of CNC content across tensile strength have been depicted in Figure 4.

3.15. Performance Realization of Bulky Chain Natural Rubber Composites. The tensile strength of the natural rubber composites is increased by 250%, having the addition of the NC from the 3–15 phr. The rise in mechanical property is due to interaction property, reinforcement effect, and dispersion between the nitrile and the NC [23]. Likewise, with the tensile strength and the coefficient value, the tensile strength of the nitrile gets raised due to rise in the concentration of the NC of up to 15.88% kN/m. One of the essential factors that hinder the commercial degradation of nanoparticles is the non-presence of robust and quick characterization strategies for performing an effective process and quality assessment along the manufacturing loop. Particularly, this challenge is more significant for the existing industry of producing nanoparticles. In spite of its impressive NC properties, it could be modified in its technical form of production in reaching its maximum potential in its functioning. In addition, the enhancements of its tool of measurement in characterizing its capability are also one of the biggest challenges to be addressed.

3.16. Mechanical Performance of NC Butadiene Rubber. The mechanical performance of the NC butadiene rubber is similar to that of the nitrile rubber, and the tensile strength and tear strength of the butadiene are about 16.9–24.1 MPa and, thus, 43.5–65.3 MPa, respectively. The excellent interfacial bonding and the distribution are mainly due to rise in the modulus and the strength of the material. The cross-linking between the matrix and the NC is mainly due to NC and the nitrile butadiene rubber, as shown in Figure 5.

3.17. Illustration of Sensors Like Skin for Robotics. Being expandable, one of the most essential qualities of skin surface is transducing the deformations characterized under mechanical properties for movement, perception over tactile strength, and essentially manipulating the objects [24]. In addition to that, the skin could also make the sensing of humidity, temperature, and vibrations, as depicted in Figure 6. In both men and women, the detections over the sensations associated with the tactile properties are made by mechanoreceptors [25, 26]. The spatial density and the sensitivity associated with mechanoreceptors change across the whole body with the maximal performance and count being placed at the forearm and the leg, as depicted in Figure 6. In order to manufacture the materials, which are maximally sensitive under the deformations of mechanical structures, the demonstrations over the nano- and the microstructuring of various elastic composites and substances have been established. This adheres to piezo sensitivity. The most regularized form of piezo-sensitive substances is declared to be as carbon conductive inks or elastomers with which the variation in the resistivity of the material is being explored with the induced strain or pressure.

4. Results and Discussion

4.1. Potential Application. These NC composites are used in various applications, such as food, packaging, automobile, water treatment, and in the paper industry. There are various functions involved in the food packing process; one such process is to increase the food packing property. Polymer-based food packing has best result in the food packing industry, in which the foods are prevented from dust, oxygen, moisture, and microorganisms, thus leading to rise in maintaining the quality of the food. In the food packing industry, the NC is best suited for the filler application, as shown in Table 2. NC has been used as filler to increase the mechanical property during packing.

NC is a non-toxic material, and it is used in several biomedical applications. In tissue engineering and in the drug carrier, the potential of the NC plays a wide role, whereas several studies have proven to show the increase in the porosity of about 93%, bulk density of 0.02 g/cm, and absorption ratio of 3000%. NC crystal also possesses grafting property. They are also used in the electronic application. The mechanical property of the PEO is increased by the electrospinning property of the polyethylene oxide and poly lactic acid. Polyvinylidene fluoride-co-hexafluro propylene is used in segregation of the lithium ions in the batteries. In rubber industry, they are used in the reinforcement property of the NC crystals as well as the NC fiber.

4.2. Reinforcement of NC in Industrial Electronic Automation. A magnificent enhancement in the utilization of naturally

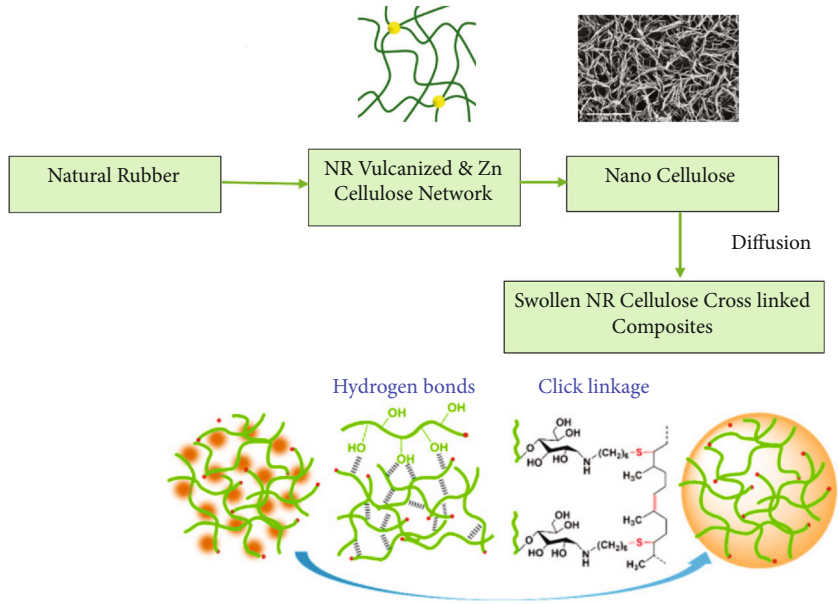

Figure 5: Illustration over the formation of dual network between rubber and ZnO.

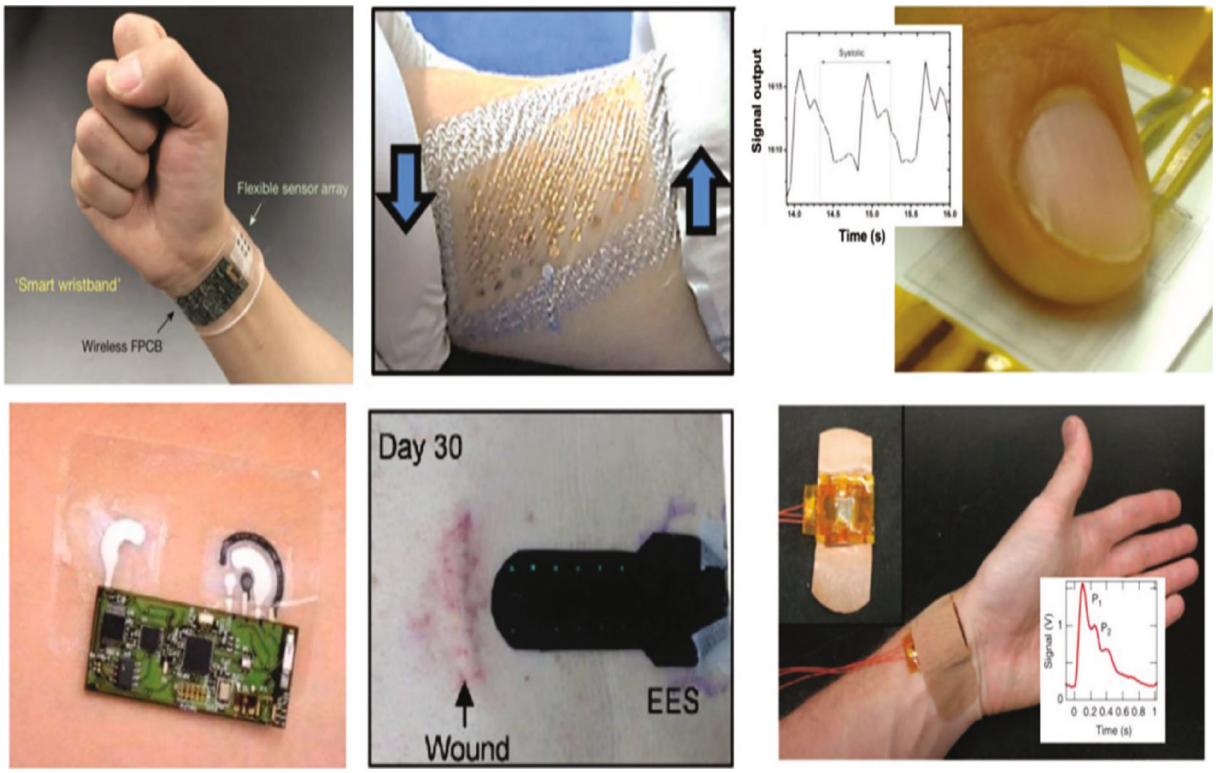

Figure 6: Illustration over the arrays of wearable integrated electronic sensors used in biohealth monitoring.

Table 2: Properties of biodegradation associated with nanocellulose system of composites.

Composites of nanocellulose	Degradable performance	Test over degradation
NCF (PLA)	The rapid initialization of degradation has been made around 5–9 weeks	ASTM D54426 at 60°C
Bacterial cellulose/starch	Cent percent degradable at 30°C	Soil
Nanocellulose/NR	After the competition of fourth week, the degradation exists over 76%	Soil

Table 3: Applications on nanocellulose polymer substrates, illustrating the electronic and mechanical domains.

S no	Usage of composite substance	Inferences
1	Digital and electronic display	Nanocellulose polymer composites have been utilized in manufacturing smart and intelligent cards, solar cells, radio spectral frequency tags, solar cells, and medical wearable sensing equipment [29].
2	Automotive mechanical parts	A substitute composite material for carbon or glass fiber nanocellulose substrates that are essentially utilized for door and window panels and glass substances
3	Packaging	The improvisation of nanocellulose polymer substrate has been realized greatly over the electronic and mechanical performance when compared to the pure polymer; it is being inferred that the permeability of O_2 content and the transmission rate of water vapor are also highly enhanced

existing polymer composites of fiber in the previous decades has been noticed, for its implication in various applications in different domains, such as construction machineries, sports machineries, automotive electronic machineries, and smart artificial intelligence machineries. Most of the countries in Europe have inculcated many efforts for enhancing the utilization of naturally developed polymer composites both in hybrid and pure nature in the components of automotive sections [27]. The major pioneers in the industrial automation also been developed in utilizing these nanopolymer composites for the non-structural and the structural elements in automobile applications. A major potential is being enforced on utilizing certain natural fibers such as flax, hemp, jute etc allowed to mix with glass or carbon resulting in hybrid form for the automotive electronic parts. The non-natural mixed fiber substances are being integrated with the electronic components with which its reliability of functioning is totally dependent on its internal bonding characteristics [28–29]. The common existing fiber composites, such as glass and banana, neither hybrid form of both being built with these NC structures, are implied for structuring the bumpers and other polyvinyl components in modernized vehicles. The reinforcement of polymer composites incorporating the banana fiber has been utilized for manufacturing the casings of mirror. The resins built by thermoset and hemp have been designed with complete body automotive functioning under certain electronics mode, and this is incorporated by Henry Ford. In addition to that, the electronic parts associated with the inserts and the door panels have been built with hybrid form of hemp–kenaf–wood composite mixtures. The reinforcement of sisal fibers within the poxy vector is being utilized for manufacturing cylinders for different electronic automotive applications. Table 3 depicts the applications on NC polymer substrates, illustrating the electronic and mechanical domains.

5. Conclusion

NC is characterized by the following properties, such as the crystalline and amorphous property. Depending on its size, the NC has better surface area, better dispersion and wettability, and increased interfacial bonding ability. The hydrophilicity may occur due to surplus quantity of the hydrogen group, thus ensuring the biodegradability and green nature of the NC composites. Various works have been enacted on the synthetic and natural polymers reinforced by the NC. In this proposed study, the applications are mainly highlighted with the enhancement and utilization of NC polymer substrates in both the domains of mechanical and electronics along with the illustrations of its unique properties. This shows the advancements in its properties when its utilization has been used in hybrid form in the state of mixed composition. It demonstrates its potentiality of being different and advantageous than the conventional mixture of composite substance that has been used traditionally. Future work includes the NC usage in the environmental application, such as water spitting as photocatalyst and in biomedical application including the antioxidant and drug carrier.

Data Availability

Data supporting this research article are available from the corresponding author or first author on reasonable request.

Conflicts of Interest

The authors declare that they have no conflicts of interest.

References

[1] B. Duchemin, D. le Corre, N. Leray, A. Dufresne, and M. P. Staiger, "All-cellulose composites based on microfibrillated cellulose and filter paper via a NaOH–urea solvent system," *Cellulose*, vol. 23, no. 1, pp. 593–609, 2016.

[2] D. R. Ruka, P. Sangwan, C. J. Garvey, G. P. Simon, and K. M. Dean, "Biodegradability of poly-3-hydroxybutyrate/bacterial cellulose composites under aerobic conditions, measured via evolution of carbon dioxide and spectroscopic and diffraction methods," *Environmental Science & Technology*, vol. 49, no. 16, pp. 9979–9986, 2015, ent system, *Cellulose*, 23, 1, (2016): 593–609.

[3] P. Liou, F. X. Nayigiziki, F. Kong, A. Mustapha, and M. Lin, "Cellulose nanofibers coated with silver nanoparticles as a SERS platform for detection of pesticides in apples," *Carbohydrate Polymers*, vol. 157, pp. 643–650, 2017.

[4] L. Ansaloni, J. Salas-Gay, S. Ligi, and M. G. Baschetti, "Nanocellulose-based membranes for CO_2 capture," *Journal of Membrane Science*, vol. 522, pp. 216–225, 2017.

[5] C. Vilela, T. D. O. Gadim, A. J. D. Silvestre, C. S. R. Freire, and F. M. L. Figueiredo, "Nanocellulose/poly (methacryloyloxyethyl phosphate) composites as proton separator materials," *Cellulose*, vol. 23, no. 6, pp. 3677–3689, 2016.

[6] I. I. Muhamad, E. Salleh, S. Shaharuddin, N. Pa'e, S. Selvakumaran, and M. H. Salehudin, *Incorporation of Filler/Additives in Polymer*

Gel for Advanced Application Polymer Gels, Springer, Singapore, 2018.

[7] P. M. Favi, S. P. Ospina, M. Kachole, M. Gao, L. Atehortua, and T. J. Webster, "Preparation and characterization of biodegradable nano hydroxyapatite–bacterial cellulose composites with well-defined honeycomb pore arrays for bone tissue engineering applications," *Cellulose*, vol. 23, no. 2, pp. 1263–1282, 2016.

[8] E. Cudjoe, M. Hunsen, Z. Xue et al., "*Miscanthus giganteus*: a commercially viable sustainable source of cellulose nanocrystals," *Carbohydrate Polymers*, vol. 155, pp. 230–241, 2017.

[9] N. M. Julkapli, S. Bagheri, and S. M. Sapuan, "Bio-nanocomposites from natural fibre derivatives: manufacturing and properties," in *Manufacturing of Natural Fibre Reinforced Polymer Composites*, pp. 233–265, Springer, Cham, 2015.

[10] A. Jabbar, J. Militký, J. Wiener, B. M. Kale, U. Ali, and S. Rwawiire, "Nanocellulose coated woven jute/green epoxy composites: characterization of mechanical and dynamic mechanical behavior," *Composite Structures*, vol. 161, pp. 340–349, 2017.

[11] M. Chaichi, M. Hashemi, F. Badii, and A. Mohammadi, "Preparation and characterization of a novel bionanocomposite edible film based on pectin and crystalline nanocellulose," *Carbohydrate Polymers*, vol. 157, pp. 167–175, 2017.

[12] A. K. Mohanty, M. Misra, and L. T. Drzal, "Sustainable biocomposites from renewable resources: opportunities and challenges in the green materials world," *Journal of Polymers and the Environment*, vol. 10, no. 1, pp. 19–26, 2002.

[13] G. Kadry, "Comparison between gelatin/carboxymethyl cellulose and gelatin/carboxymethyl nanocellulose in tramadol drug loaded capsule," *Heliyon*, vol. 5, no. 9, article e02404, 2019.

[14] R. Hashaikeh, P. Krishnamachari, and Y. A. Samad, "Nanomanifestations of cellulose: applications for biodegradable composites," in *Handbook of Polymer Nanocomposites. Processing, Performance and Application*, pp. 229–248, Springer, Berlin, Heidelberg, 2015.

[15] A. K. Bledzki, P. Franciszczak, and A. Meljon, "High performance hybrid PP and PLA biocomposites reinforced with short man-made cellulose fibres and softwood flour," *Composites Part A: Applied Science and Manufacturing*, vol. 74, pp. 132–139, 2015.

[16] P. Zhang, L. Chen, Q. Zhang, and F. F. Hong, "Using in situ dynamic cultures to rapidly biofabricate fabric-reinforced composites of chitosan/bacterial nanocellulose for antibacterial wound dressings," *Frontiers in Microbiology*, vol. 7, p. 260, 2016.

[17] A. Hebeish, S. Farag, S. Sharaf, and T. I. Shaheen, "Advancement in conductive cotton fabrics through in situ polymerization of polypyrrole-nanocellulose composites," *Carbohydrate Polymers*, vol. 151, pp. 96–102, 2016.

[18] J. Trifol, D. Plackett, C. Sillard, P. Szabo, J. Bras, and A. E. Daugaard, "Hybrid poly(lactic acid)/nanocellulose/nanoclay composites with synergistically enhanced barrier properties and improved thermomechanical resistance," *Polymer International*, vol. 65, no. 8, pp. 988–995, 2016.

[19] M. M. Hamedi, A. Hajian, A. B. Fall et al., "Highly conducting, strong nanocomposites based on nanocellulose-assisted aqueous dispersions of single-wall carbon nanotubes," *ACS Nano*, vol. 8, no. 3, pp. 2467–2476, 2014.

[20] N. T. Cervin, C. Aulin, P. T. Larsson, and L. Wågberg, "Ultra porous nanocellulose aerogels as separation medium for mixtures of oil/water liquids," *Cellulose*, vol. 19, no. 2, pp. 401–410, 2012.

[21] M. G. Thomas, E. Abraham, P. Jyotishkumar, H. J. Maria, L. A. Pothen, and S. Thomas, "Nanocelluloses from jute fibers and their nanocomposites with natural rubber: preparation and characterization," *International Journal of Biological Macromolecules*, vol. 81, pp. 768–777, 2015.

[22] K. Jeong and A. B. Kahng, "A power-constrained MPU roadmap for the international technology roadmap for semiconductors (ITRS)," in *International SoC Design Conference (ISOCC)*, pp. 49–52, IEEE, 2009.

[23] S. P. Jani, A. S. Jose, C. Rajaganapathy, and M. A. Khan, "A polymer resin matrix modified by coconut filler and its effect on structural behavior of glass fiber-reinforced polymer composites," *Iranian Polymer Journal*, vol. 31, no. 7, pp. 1–11, 2022.

[24] M. Y. Teo, N. Kim, S. Kee et al., "Highly stretchable and highly conductive PEDOT: PSS/ionic liquid composite transparent electrodes for solution-processed stretchable electronics," *ACS Applied Materials & Interfaces*, vol. 9, no. 1, pp. 819–826, 2017.

[25] J. S. Kim, S. H. Cho, K. L. Kim et al., "Flexible artificial synesthesia electronics with sound-synchronized electroluminescence," *Nano Energy*, vol. 59, pp. 773–783, 2019.

[26] M. Ramesh, K. Palanikumar, and K. H. Reddy, "Plant fibre based bio-composites: sustainable and renewable green materials," *Renewable and Sustainable Energy Reviews*, vol. 79, pp. 558–584, 2017.

[27] O. Zabihi, M. Ahmadi, S. Nikafshar, K. C. Preyeswary, and M. Naebe, "A technical review on epoxy-clay nanocomposites: structure, properties, and their applications in fiber reinforced composites," *Composites Part B: Engineering*, vol. 135, pp. 1–24, 2018.

[28] V. K. Thakur, M. K. Thakur, and R. K. Gupta, "Raw natural fiber–based polymer composites," *International Journal of Polymer Analysis and Characterization*, vol. 19, no. 3, pp. 256–271, 2014.

[29] D. Trache, A. F. Tarchoun, M. Derradji et al., "Nanocellulose: from fundamentals to advanced applications," *Frontiers in Chemistry*, vol. 8, p. 392, 2020.

Hindawi
International Journal of Polymer Science
Volume 2023, Article ID 2541384, 13 pages
https://doi.org/10.1155/2023/2541384

Research Article

Design and Development of Polymer-Based Optical Fiber Sensor for GAIT Analysis

Mamidipaka Hema,[1] **Jami Venkata Suman**,[2] **Boddepalli Kiran Kumar**,[3] **and Adisu Haile**[4]

[1]*Department of ECE, JNTU-GV College of Engineering, Vizianagaram, India*
[2]*Department of ECE, GMR Institute of Technology (A), Rajam, India*
[3]*Department of CSE, Aditya College of Engineering, Surampalem, India*
[4]*Department of Mechanical Engineering, WOLLO University, Kombolcha Institute of Technology, P.O. Box no: 208, Kombolcha, Ethiopia*

Correspondence should be addressed to Adisu Haile; adisu.haile@wu.edu.et

Received 21 July 2022; Revised 29 October 2022; Accepted 27 January 2023; Published 20 February 2023

Academic Editor: Adam Khan M

In the present scenario like COVID-19 pandemic, to maintain physical distance, the gait-based biometric is a must. Human gait identification is a very difficult process, but it is a suitable distance biometric that also gives good results at low resolution conditions even with face features that are not clear. This study describes the construction of a smart carpet that measures ground response force (GRF) and spatio-temporal gait parameters (STGP) using a polymer optical fiber sensor (POFS). The suggested carpet contains two light detection units for acquiring signals. Each unit obtains response from 10 nearby sensors. There are 20 intensity deviation sensors on a fiber. Light-emitting diodes (LED) are triggered successively, using the multiplexing approach that is being employed. Multiplexing is dependent on coupling among the LED and POFS sections. Results of walking experiments performed on the smart carpet suggested that certain parameters, including step length, stride length, cadence, and stance time, might be used to estimate the GRF and STGP. The results enable the detection of gait, including the swing phase, stance, stance length, and double supporting periods. The suggested carpet is dependable, reasonably priced equipment for gait acquisition in a variety of applications. Using the sensor data, gait recognition is performed using genetic algorithm (GA) and particle swarm optimization (PSO) technique. GA- and PSO-based gait template analyses are performed to extract the features with respect to the gait signals obtained from polymer optical gait sensors (POGS). The techniques used for classification of the obtained signals are random forest (RF) and support vector machine (SVM). The accuracy, sensitivity, and specificity results are obtained using SVM classifier and RF classifier. The results obtained using both classifiers are compared.

1. Introduction

Utilizing biometric information, identity recognition is being done in many scenarios. Even gender recognition and age estimation are being done by such information. Human age estimation has emerged as an important area of research [1], such that minors can be prevented from purchase of banned items and also access of inappropriate web pages. Further, elderly monitoring and human–computer interaction are feasible. Initially, age estimation was done on facial features. At distance, the facial features have low resolution on constrained details [2]. Every gait cycle consists of two steps and spans the time between the first time an event occurs with a particular foot and the next time it occurs with the same foot. Due to their superior elasticity, reduced Young's modulus, better strain limitations, impact strength, and shock resistance, polymer optical fibers (POFs) outperform silica optical fibers [3]. The use of POF for gait

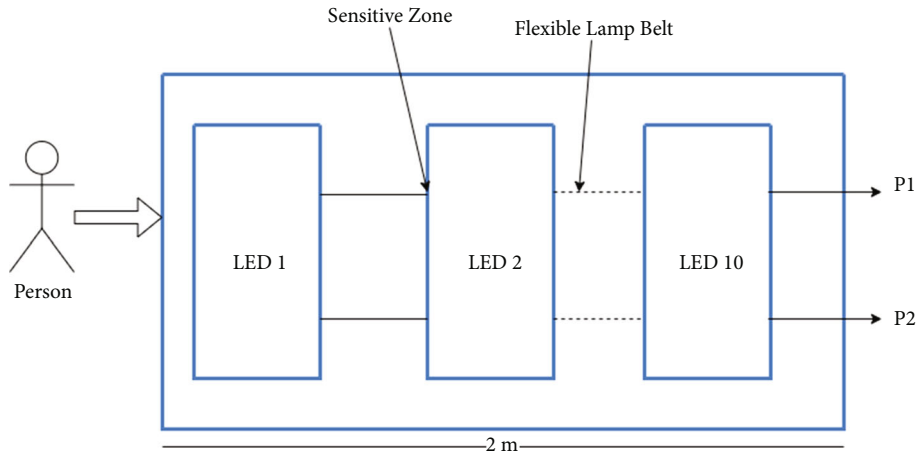

Figure 1: Structure of FOPS smart carpet for gait analysis.

examination has several applications in the clinical setting, including sensors for tracking joints angular movement, heel pressure, gait frequency, and foot positioning during the stride. Over the years, many POF sensor designs have been put forth, fiber Bragg gratings (FBGs), and interferometers. In terms of cost, manufacturing complexity, and signal processing simplicity, intensity variation-based sensors outperform the others. Since each sensor would need a photo-detector and a light generator, the absence of multiplexing abilities poses a significant obstacle to the implementation of intensity deviation sensors in the measurement of multiple parameters.

In Leal-Junior et al. [4], an insole POF-based gait signal detector and an intensity deviation POF curve sensor were created. For the practical testing of the sensors, a robotic leg and an electrical stimulating system for gait intervention were utilized. A method to monitor ground reaction force (GRF) throughout the gait phase was described in Leal-Junior et al. [5]. Because of the viscous elasticity, this polymer is not able to respond in accordance with stress consistently. Therefore, a method compensating for this impact is also suggested. Avellar et al. [6] created an intelligent carpet for measuring gait patterns and GRF built on POF. One fiber of the recommended carpet includes amplitude variability sensors and two photodiodes for acquiring signal. Multiplexing technology is centred on coupling among the luminaires and POF longitudinal portions. Specifically, built wearable foot sensors implanted in the shoe liner were used by Bucinskas et al. [7] to develop a system for fall prediction. By analysing, parameters such as weight, step size, and timing of phase enable gait evaluation.

A multiplexing strategy relying on light source coupling was presented in as a solution to this problem. In this technology, photo-detectors are placed above POF edges; measure the power of sensors' optical fluctuation during the activation of light sources. This approach yields better spatial resolution. Additionally, compared to other systems, the intensity deviation multiplexing approach produces a device at a cheaper cost [8]. Involving a mainframe can improve surveillance systems' intelligence, analyse customs, and allow robots [9]. Artificial intelligence-based gender categorization may utilize facial [10], vocal [11], or gait [12] inputs. Among these, gait has become the most sophisticated feature, being detected from a distance [13]. Many pioneering works on this have been reported. Furthermore, gait can be utilized for gender classification as done by Kozlowski and Cutting [14].

This research introduces the development of a smart platform that measures GRF and spatio-temporal gait parameters (STGP) using a polymer optical fiber sensor (POFS). The POF is made up of polymethyl methacrylate (PMMA), fluorinated polymer cladding, and polyethylene coating. The features obtained from the proposed POFS in the form of signals are given to the classifier to analyse the gait. The accuracy, sensitivity, and specificity results are computed by utilizing various classifiers such as support vector machine (SVM) and random forest (RF).

2. Materials and Methods

2.1. Polymer Optical Fiber Sensor. The construction of the POFS smart carpet is performed on a single POF arranged perpendicular to the walking direction between two 60 cm × 2 m polyethylene layers, as shown in Figure 1. The POF was composed of PMMA having 980 μm core diameter, fluorinated polymer cladding (20 μm), and polyethylene covering, which provides 2.2 mm overall diameter. A flexible light-emitting diode (LED) lamp strip that is laterally placed serves as the light source and the sensors' reactions. The FRMD-KL25Z microcontroller handles signal capture and LED control. When contrasted to industrial devices often utilized for gait assessment, this leads to a cheaper cost solution. It must also be mentioned that the planned POFS smart carpet does have a modular design, which means that the system may be built with varying numbers of LED elastic light belts across the span total span.

To ensure the appropriate length and thickness of the POF sensor, it is mounted on a permanent support. 20 sections are created laterally on the fiber with 20 cm separation. Each lateral part is outfitted with LED flexible light belts. When pressure is imparted to each lateral part, an optical power change occurs, which P1 and P2 detect. The optical power fluctuation of all 20 sensors was measured using two photo-detectors. Thus, P1 acquires the responses of 10 sensors (R_{P1}), whereas P2 acquires

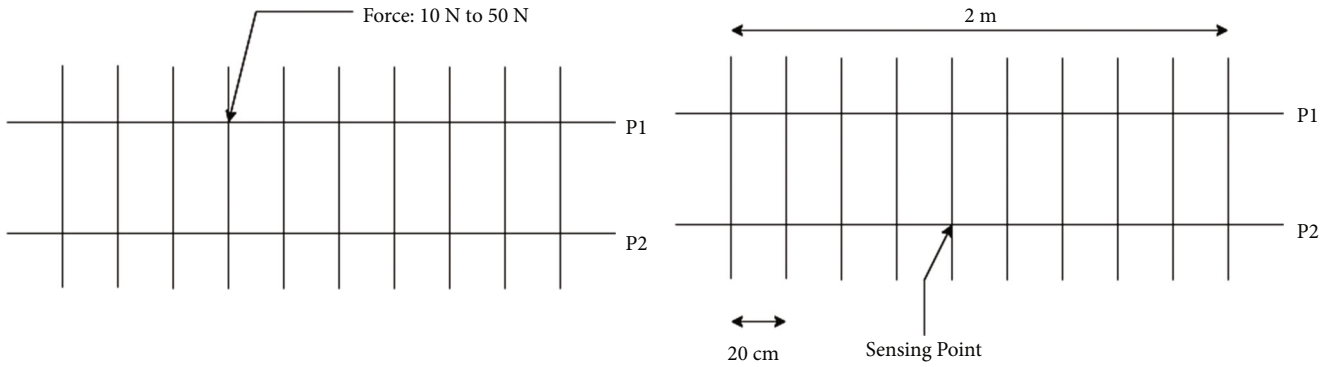

Figure 2: Characterization setup: (a) characterization of force; (b) characterization of space.

the responses of the other 10 sensors (R_{P2}). A microprocessor regulates the activation rate and sequence of one LED belt at a time. This is accomplished by activating two sensors (left and right) at the same time. The acquisition pattern is obtained from LEDs 1–10 with 30 Hz activation rate. Furthermore, the microcontroller is in charge of acquiring the optical signal detected by individual photo-detectors. Figure 2(a) depicts the setup for the characterization of force. The next approach is the characterization of space that depends on the placement of foot in specified distance markers. The purpose of this procedure is to link optical intensity with carpet distance. This assessment is connected to the force description since the sensor reaction with predetermined weights must be obtained precisely on the top of sensors. The setup for the characterization of space is depicted in Figure 2(b).

Equation (1) is used to compute the association between the attenuation of optical energy and the person's distance towards the POFS. F_0 indicates the force deployed over the POFS. F_n is the applied force alongside the fiber. n denotes the separation between F_1 and F_0. l denotes the spacing between LEDs.

$$n = \frac{F_n \cdot l}{F_0}. \tag{1}$$

Figure 3 depicts the reaction of detectors towards the loads given POFSs in the force evaluation, including the coefficient of determination (R2) and relative errors. Markers stand for the observed response, and consistent lines indicate the fitness of POFS. Figures 3(c) and 3(d) show the behaviour of load administration and a saturating propensity for larger loads. Figures 3(a) and 3(b) depict the responses of POFS. Since linearity and sensitivity are connected to the manufacture of each sensor, sensitivity varies for each light detector. Interestingly, the sensors 1 obtained by each optical detector exhibit polynomial behaviour.

2.2. Feature Extraction. There are two categories of human gait representation [15, 16]. The frequency model-based feature is not reliable. Therefore, another set of features such as force and space-based features have been used [17]. All data for experimental purpose are obtained from the POFS-based carpet. Human gait signals may be extracted using filtering and thresholding. In Wang et al. [18], extracting human gait features from signal sequences has been done. As the features of the gaits are not unique, normalization has to be done to bring to the same value.

2.2.1. Gait Energy Signals. Gait energy signal (GES) gives the spatiotemporal data of silhouette out of the whole cycle of gait. By obtaining mean of the signals yields a signal representing energy. $D(x, y)$ representing GES can be calculated by using Equation (2). Here, N gives a count of gait cycle signals. x and y indicate the gait signal coordinates.

$$D(x, y) = \frac{1}{N}\sum_{t=1}^{N} Bt(x, y). \tag{2}$$

Taking gait as the relevant characteristics [19], the gait model (GM) presents the sensitive ageing-related parameters, such as applied force and length of stride varies with age. Length of stride and force [20–22] are useful parameters for getting a useful gait-based age descriptor.

2.2.2. Dynamic Gait Energy Signal. Due to the slight movements of legs and the pressure applied on the sensor, static data from these get into GES. For reducing the impact of this static information, the dynamic information is attained with force, leg joint change and stride length represented by Equation (3).

$$I_{\mathrm{GES}}(x, y) = \begin{cases} 0 & \text{if } I_{\mathrm{GES}}(x, y) > 220 \\ 1 & \text{if } I_{\mathrm{GES}}(x, y) \neq 0 \end{cases}. \tag{3}$$

Second step computes dynamic part of GES with "AND" operator in individual signals of gait cycle sequences after acquisition of the dynamic section of the signal as indicated in Equation (4).

$$F'(x, y) = F(x, y) \times I_{\mathrm{GES}}(x, y). \tag{4}$$

2.2.3. Gait Energy Projection Model. Gait energy projection model (GPM) gives the important gender-associated

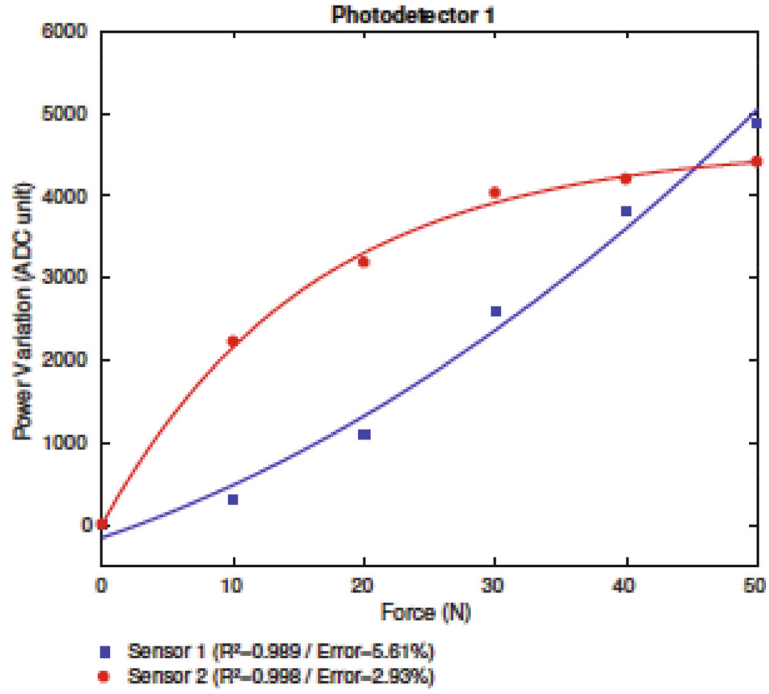

(a)

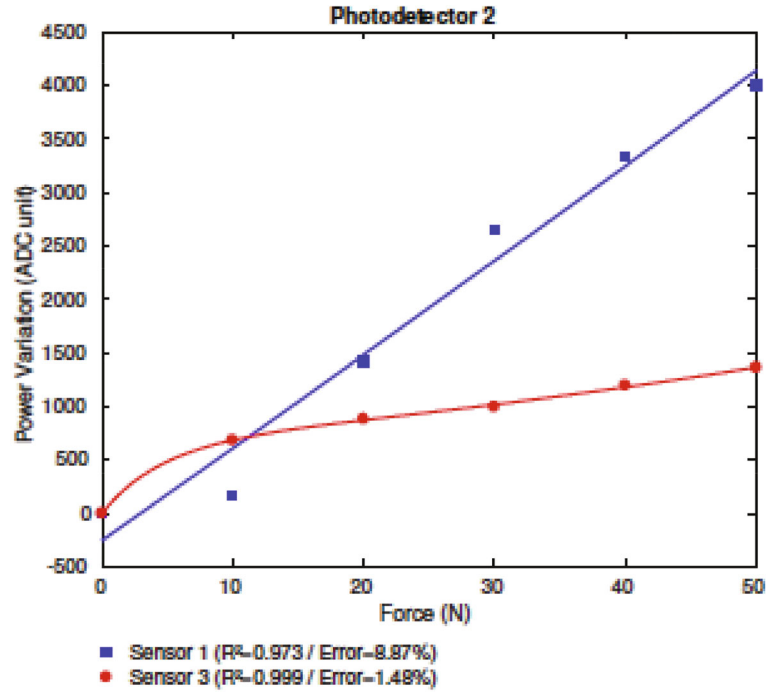

(b)

Figure 3: Continued.

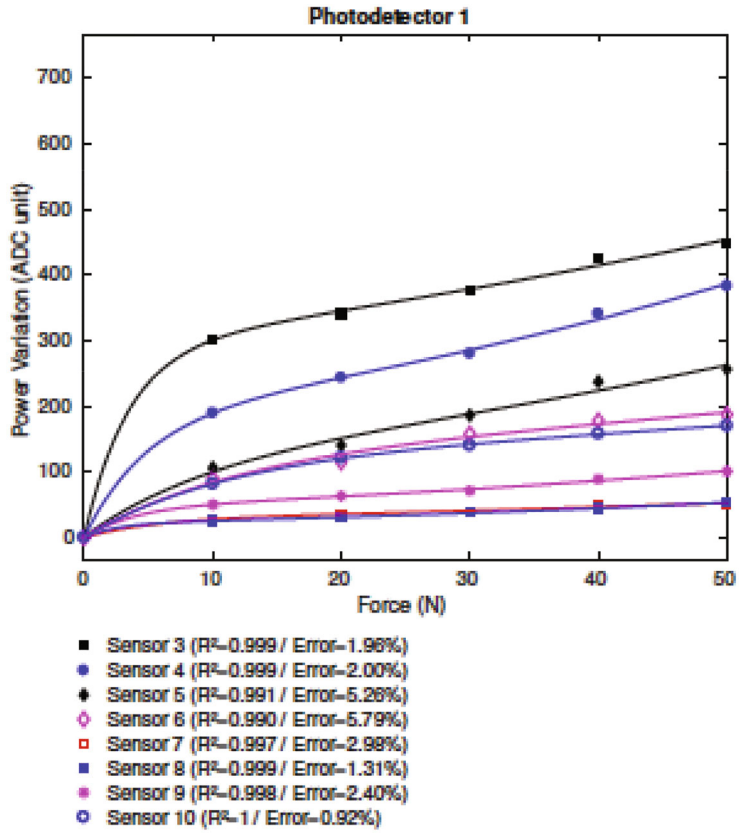

(c)

Figure 3: Continued.

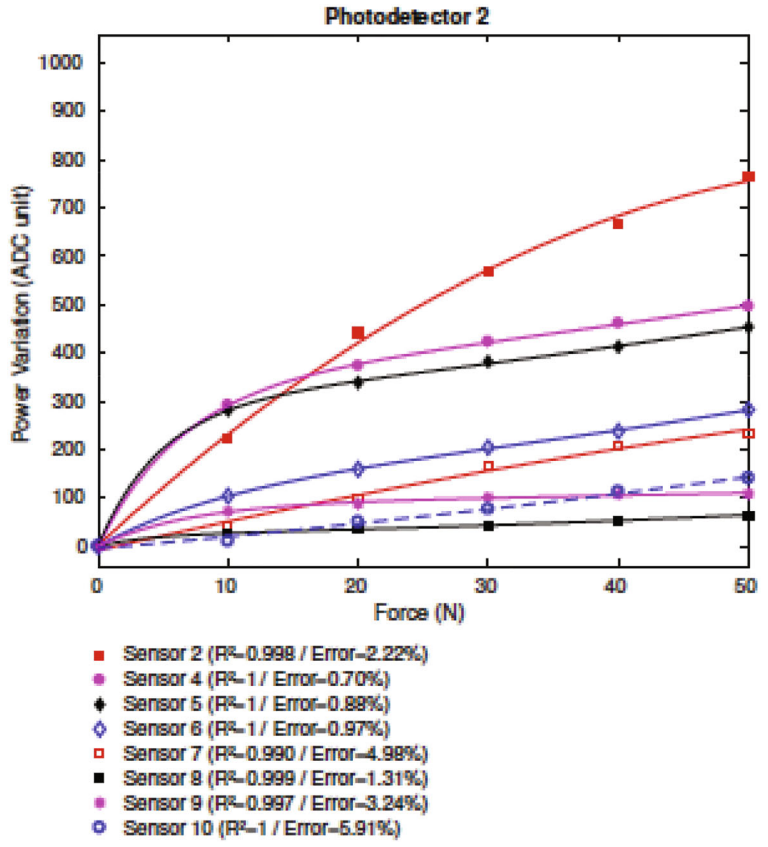

(d)

Figure 3: Force characterization response: (a) right POFS 1 and 2 with P1; (b) left POFS 1 and 3 with P2; (c) right POFS 3–10 with P1; (d) left POFS 2 and 4–10 with P2.

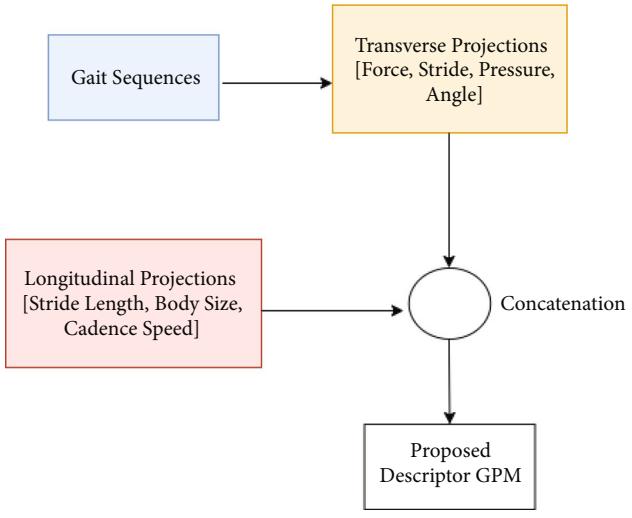

Figure 4: GPM descriptor identification.

parameter like size of body and variation in the length of stride as depicted in Figure 4.

$$\mathrm{GPM} = \left\{\mathrm{GLP}_{\mathrm{cycle}} U\, \mathrm{GTP}_{\mathrm{cycle}}\right\}. \tag{5}$$

In GPM, the two projections are gait energy longitudinal projection (GLP) and gait energy transverse projection (GTP).

$$\mathrm{GLP}_{\mathrm{cycle}} = \frac{1}{M}\sum_{i=1}^{M} GLP_i, \tag{6}$$

$$\mathrm{GTP}_{\mathrm{cycle}} = \frac{1}{M}\sum_{i=1}^{M} \mathrm{GTP}_i, \tag{7}$$

No of sets of signals = M; and i stands for the i^{th} signal vector.

2.2.4. Gradient Gait Energy Signal. Based on the averaging concept, gradient gait energy signal (GGES) has more mobile attributes than the straight forward gait signals. Kernels are required to acquire the energy of signals. Kernels create the gradient GGES pattern from energy signal of gait.

3. Feature Selection Using Genetic Algorithm

Genetic algorithm (GA) offers optimization inspired by natural solution [23, 24]. The operations are iterative and provide chromosome as a symbols string. Initial population is

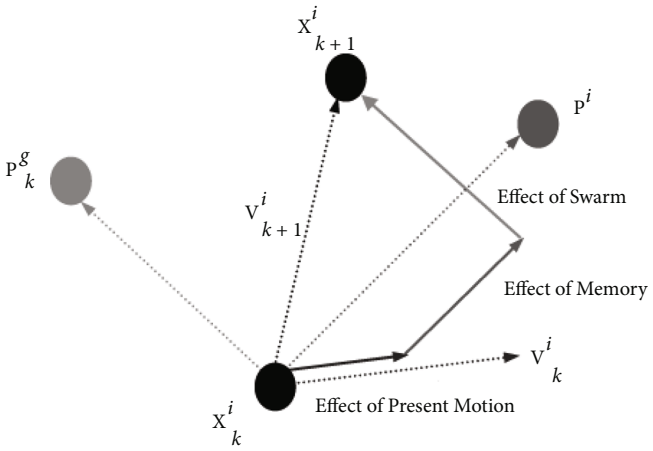

Figure 5: Velocities and positions in PSO.

an arbitrarily created set of strips. Three basic operations of genetic origin guide the search: selection, crossover, and mutation. The aim of selecting feature subset is to utilize lesser number of features, and the performance of SVM and RF may be evaluated by a validation data set for guiding the GA. Each feature subset possesses few features. By random generation, initial population is selected.

3.1. Particle Swarm Signal Template Optimization. GA and particle swarm optimization (PSO) are used to attain the borders of GES and GGES contours. The optimization process will be performed during the training and testing process. The parameters in gait signals are split into categories of weight (W_H, W_L, W_R, W_F) and stride (S_H, S_M, S_F). It is observed that the S_H and S_F are the only parameters depend on covariate conditions and S_M is independent. Swarm technique is applied in dividing the features of the signal by closely looking towards the parameters. The use of particle swarm signal template optimization (PSSTO) has more impact on the performance of the technique. So, the parameters that are retrieved can be tuned by using another overlaying optimizer. PSO includes necessary parameters such as position (X_k^i) and velocity (V_k^i) as described in Equations (8) and (9). For the i^{th} particle at k^{th} time, the minimum and maximum ranges are coined by X_{min} and X_{max}, respectively. The update in velocity at time $k + 1$ is computed using Equation (10).

$$X_k^i = X_{min} + \text{rand}\,(X_{max} - X_{min}), \tag{8}$$

$$V_k^i = \frac{X_{min} + \text{rand}\,(X_{max} - X_{min})}{\Delta t}, \tag{9}$$

$$V_{k+1}^i = wV_k^i + C_1\,\text{rand}\,\frac{(P^i - X_k^i)}{\Delta t} + C_2\,\text{rand}\,\frac{(P_k^g - X_k^i)}{\Delta t}, \tag{10}$$

where P_k^g indicates the overall best position and P^i denotes the best position. C_1 and C_2 are the coefficients. The velocity used to revise the location of particle is computed using Equation (11).

$$X_{k+1}^i = X_k^i + V_{k+1}^i \Delta t. \tag{11}$$

Updating velocity and position, and fitness computation are major operations that are repeated until convergence and are depicted in Figure 5.

4. Classification and Recognition

4.1. Training and Testing Phase. The total signals are classified into training and testing sets. In training phase, database signals are selected and applied with GES/GGES. The PSO template and GES/GGES features are contrasted with test signals. Linear discriminant analysis (LDA) is selected as classifier to recognize exact signal. Obtained signal is provided to Principal Component Analysis (PCA) for additional reduction in dimension.

4.2. Feature Reduction. For feature reduction, PCA and LDA are the optimum transform schemes. PCA discards labels of class and its target is to locate the orientation known as principal component, which maximizes the conflict. LDA computes the orientation and linear discriminants for maximization of separation. Combination of PCA and LDA is known to give good results.

4.3. SVM Classification. SVM classifier with linear kernel has been one of classifiers, which can categorize the feature vector with the help of a hyper plane [25]. The separation between the data is coined as decision hyperplane, and the separation from the hyper-plane is termed margin. Optimum target of SVM training is to obtain the hyper-plane having highest margin and to provide accurate classification [26]. Usage of linear kernel reduces the risk of over-fitting the data and increases the efficiency of classification by reducing the overall complexity.

4.4. RF Classifier. Random trees, then again, randomize the choice criteria. A random choice basis is characterized by a random characteristic and an irregular limit. Random trees, in this way, separate the preparation information on totally random characteristics [27]. This randomization primarily addresses high dimensional information and speculation. A random tree chooses an irregular element and a random edge and partitions the preparation pictures at a hub as depicted in Figure 6.

Recursively, an entire tree and thusly an accumulation of trees are assembled, which comprise a random timberland. The classification results from each tree are gathered for an info picture and regularly, a basic larger part casting a vote plot grants the subsequent class mark. In the accompanying areas, we present the utilization of RF on various related picture tasks. The features extracted consist of feature vectors from the trained data, and the trained data are given by Equation (12). Here, T_n is the elements that are present in the

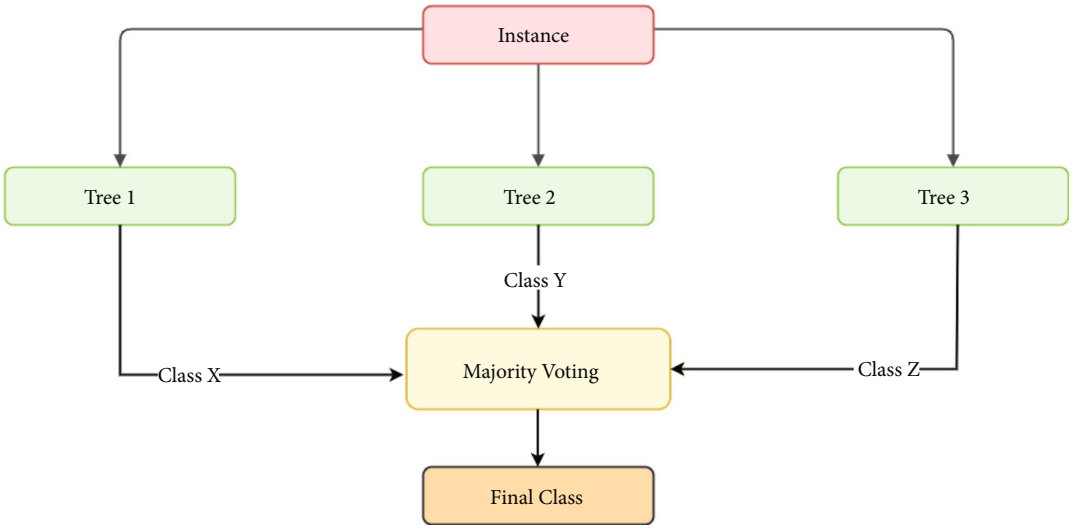

Figure 6: Random forest classifier model.

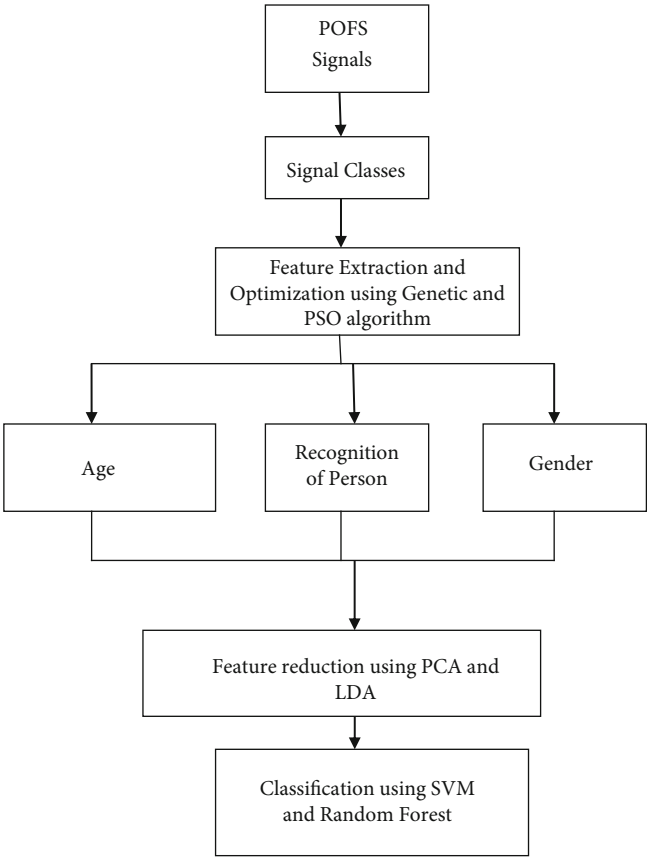

Figure 7: Design flow of proposed classification model.

data; each of the data has its own feature which is termed c_p.

$$D = T_n c_p ; n = 1, \cdots N \text{ and } p = 1, \cdots P. \quad (12)$$

The accuracy of classification increases due to the presence of decision trees, which acts the nodes to obtain the relevant data. The process flow of the proposed POFS signal-based gait classification model is provided in Figure 7.

5. Results and Discussion

The performance of SVM and RF using GA and PSO are contrasted to find out the optimum technique that

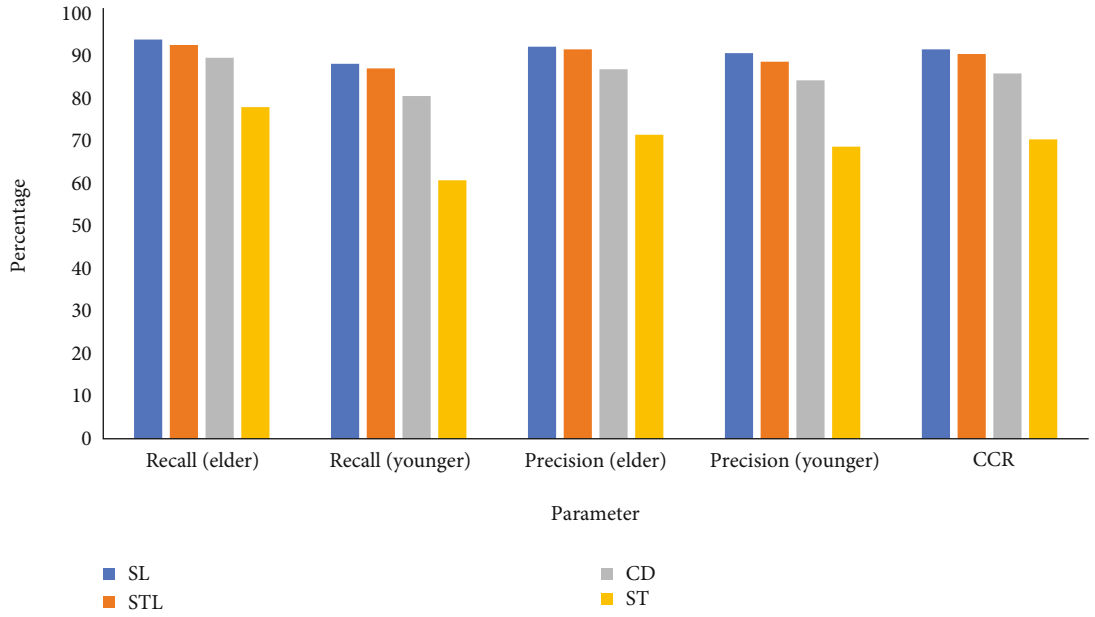

Figure 8: Age recognition with GA and SVM.

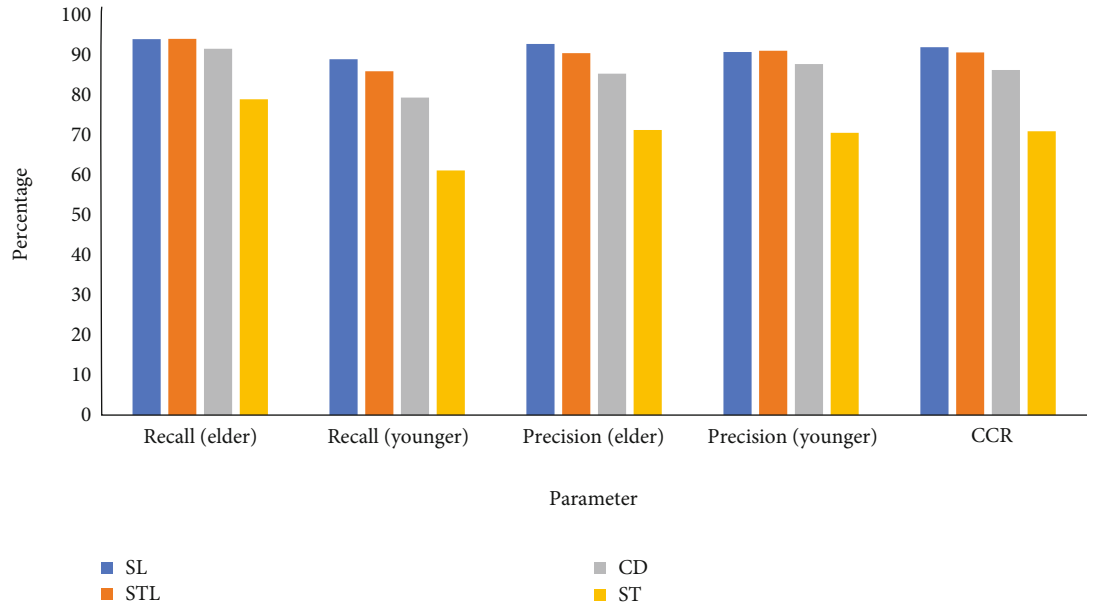

Figure 9: Age recognition with PSO and RF.

provides better results. The classifiers are provided with optimum features provided by GA and PSO algorithms. Optimal features selected are given as the input to the classifiers, and the results does not have the effect of unwanted features.

5.1. Age Recognition. Let us consider age recognition using GA and PSO optimization with various conditions. The parameters like recall, precision, and correct classification rate (CCR) are evaluated. Various descriptors such as step length (SL), stride length (STL), cadence (CD), and stance time (ST) are used for the recognition of age. For all the parameters evaluated, SL produces maximum value. So, SL can be selected as the optimum descriptor for the recognition of age. The results obtained for age recognition with GA and SVM are depicted in Figure 8.

While considering recall (elder), STL produces maximum value of 93.9%. For all the remaining parameters, descriptor SL produced maximum values. So, SL can be selected as the optimum descriptor for the recognition of age. The descriptor ST provides the lowest values for the performance parameters. The results obtained for age recognition with PSO and RF are depicted in Figure 9.

5.2. Gender Recognition. Let us consider gender recognition using GA and PSO optimization with various conditions.

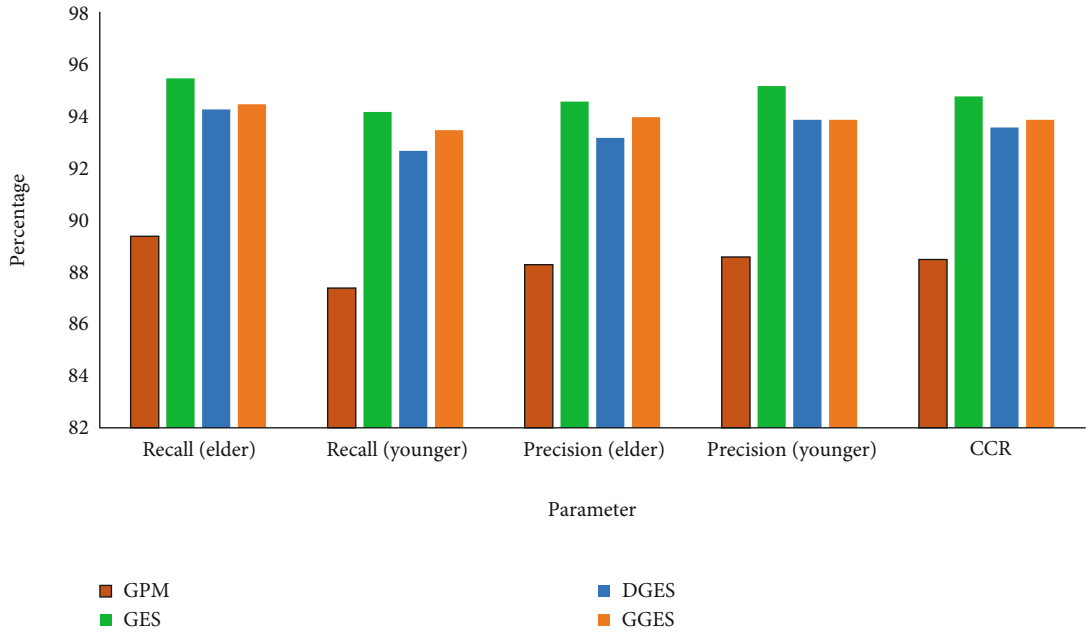

Figure 10: Gender recognition with GA and SVM.

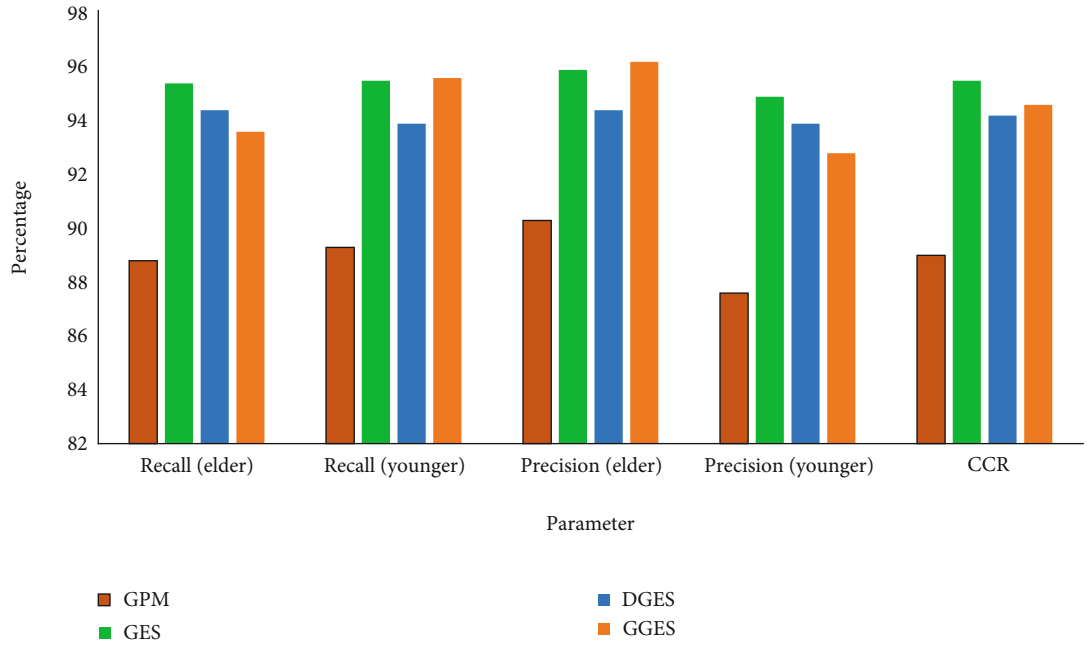

Figure 11: Gender recognition with PSO and RF.

Various descriptors such as GPM, GES, dynamic gait energy signal (DGES), and GGES are used for the recognition of gender. The parameters like recall, precision, and CCR are evaluated. During the recognition of gender using GES descriptor, maximum values are obtained for all the parameters. Lowest parameter values were obtained for the descriptor GPM. This implicates that GES is the optimum descriptor for gender recognition using GA and SVM. The results obtained are shown in Figure 10.

While performing gender recognition with PSO and RF, the usage of GGES descriptor provides maximum value 95.9% for the parameter precision (elder). Maximum values for all the remaining parameters are obtained for the descriptor GES. Lowest parameter values were obtained for the descriptor GPM. This implicates that GES is the optimum descriptor for gender recognition using PSO and RF. The results obtained are shown in Figure 11.

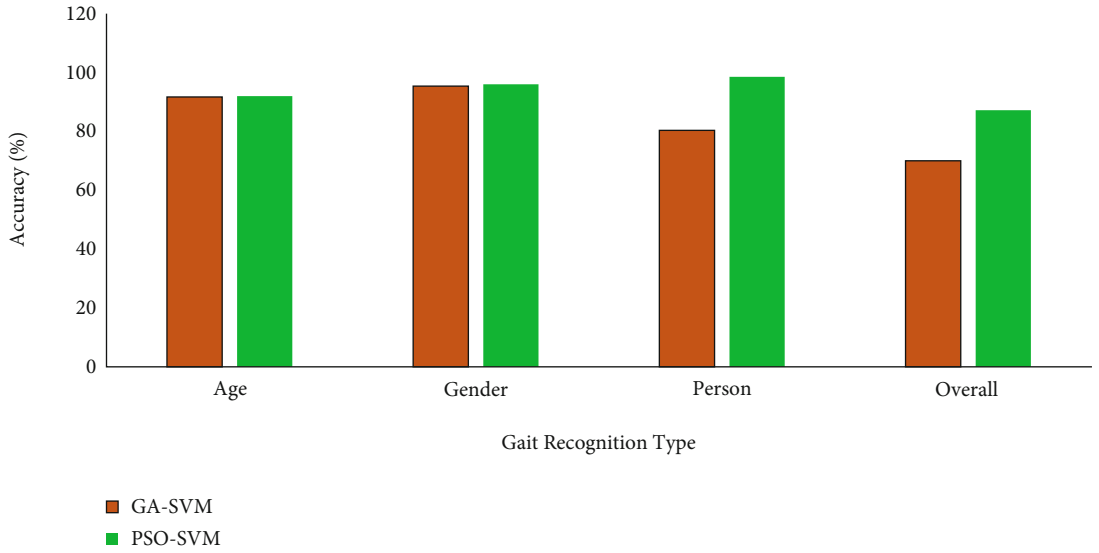

Figure 12: Accuracy using SVM classifier.

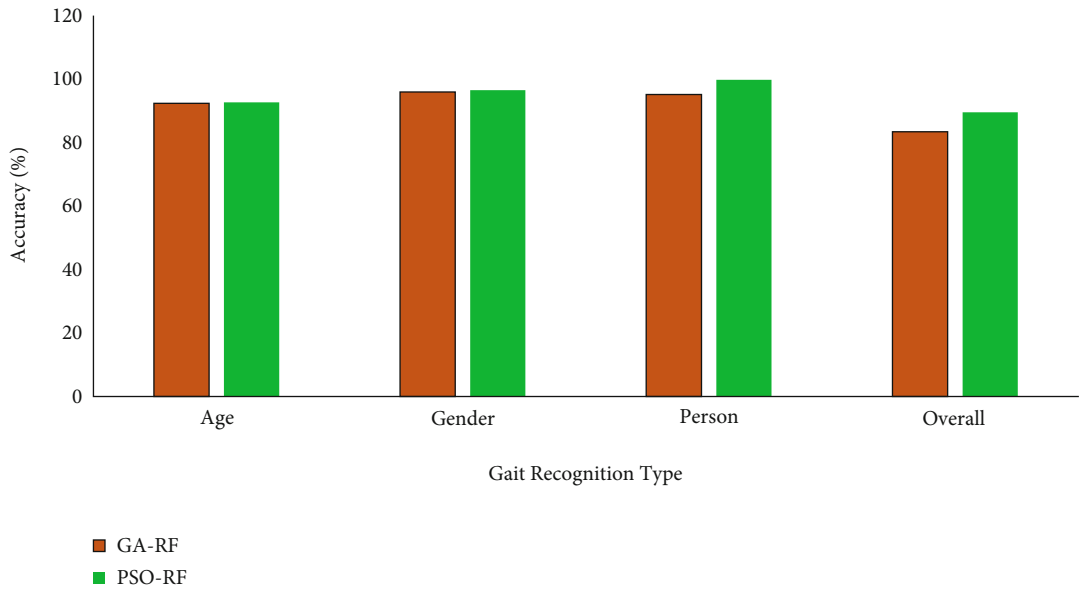

Figure 13: Accuracy using RF classifier.

5.3. Classifier Performance. SVM and RF are the two classifiers used for recognizing various gait-related human biometrics. The performance of these two classifiers is compared to find out the optimum classifier for gait classification from the signals obtained from POFS. Initially, SVM is considered with two optimization techniques such as GA and PSO. The accuracy comparison is depicted in Figure 12.

PSO-SVM provides the maximum accuracy for different gait-related analysis. So PSO is identified as the best optimizer for the selection of descriptors. The maximum overall recognition accuracy is found to be 87.16% for PSO-SVM. In the next stage of experiment, RF is considered with two optimization techniques such as GA and PSO. The accuracy comparison for RF classifier is depicted in Figure 13. In this analysis, PSO-RF provides the maximum accuracy for different gait-related analysis. So PSO is identified as the best optimizer for the selection of descriptors while using RF classifier.

From Figures 12 and 13, it is clear that the maximum value for overall accuracy of 89.58% is provided by PSO-RF classifier. This value is 2.42% more than that of PSO-SVM classifier. So, the PSO-RF classifier can categorize signals obtained from POFS in an efficient way.

6. Conclusion

This study described the construction of a smart carpet that measures GRF and STGP using a POFS. The suggested carpet contains two light detection units for acquiring signals. Each unit is capable of obtaining response from 10 nearby sensors. There are 20 intensity deviation sensors on a fiber.

One LED is triggered successively using the multiplexing approach that is being employed. Multiplexing is dependent on coupling among the LED and POFS sections. Results of walking experiments performed on the smart carpet suggested that certain parameters, including SL, STL, CD, and ST, might be used to estimate the GRF and STGP. The results enable the detection of gait instances, including the stance and swing phases, stance length, and the double supporting periods. The suggested carpet is dependable, reasonably priced equipment for gait acquisition in a variety of applications. An optimized GA-based approach for automatic feature selection has been proposed. Using PCA and LDA, irrelevant information has been reduced. SVM and RF classifier have been used to categorize signals in terms of person age and gender. This method could provide insight into gait classification problems with an overall accuracy of 89.58%. The inclusion of polymer-based sensors (POFS) provided high quality signals, and the analysis provided better results. Major merits of using POFS are the improved signal quality and fast response.

Data Availability

Data supporting this research article are available from the corresponding author or first author on reasonable request.

Conflicts of Interest

The authors declare that they have no conflicts of interest.

References

[1] N. K. Sarah, "Using artificial neural network for human age estimation based on facial images," *Proceedings of International Conference Innovations in Information Technology*, pp. 215–219, United Arab Emirates, Abu Dhabi, UAE, 2012.

[2] J. Lu and Y. -P. Tan, "Gait-based human age estimation," *IEEE International Conference on Acoustics, Speech and Signal Processing*, pp. 1718–1721, Dallas, TX, USA, 2010.

[3] K. Peters, "Polymer optical fiber sensors-a review," *Smart Materials and Structures*, vol. 10, p. 013002, 2011.

[4] A. G. Leal-Junior, A. Frizera, L. Vargas-Valencia et al., "Polymer optical fiber sensors in wearable devices: toward novel instrumentation approaches for gait assistance devices," *IEEE Sensors Journal*, vol. 18, no. 17, pp. 7085–7092, 2018.

[5] A. G. Leal-Junior, A. Frizera, L. M. Avellar, C. Marques, and M. J. Pontes, "Polymer optical fiber for in-shoe monitoring of ground reaction forces during the gait," *IEEE Sensors Journal*, vol. 18, no. 6, pp. 2362–2368, 2018.

[6] L. M. Avellar, A. G. Leal-Junior, C. A. Diaz, C. Marques, and A. Frizera, "POF smart carpet: a multiplexed polymer optical fiber-embedded smart carpet for gait analysis," *Sensors*, vol. 19, no. 15, p. 3356, 2019.

[7] V. Bucinskas, A. Dzedzickis, J. Rozene et al., "Wearable feet pressure sensor for human gait and falling diagnosis," *Sensors*, vol. 21, no. 15, p. 5240, 2021.

[8] G. A. T. Sevilla, J. P. Rojas, H. M. Fahad et al., "Flexible and transparent silicon-on-polymer based sub-20 nm non-planar 3D FinFET for brain-architecture inspired computation," *Advanced Materials*, vol. 26, no. 18, pp. 2794–2799, 2014.

[9] L. Lee and W. Grimson, "Gait analysis for recognition and classification," *Proceedings of Fifth IEEE International Conference on Automatic Face Gesture Recognition*, pp. 155–161, Washington, USA, DC, 2002.

[10] B. A. Golomb, D. T. Lawrence, and T. J. Sejnowski, "SEXNet: a neural network identifies sex from human faces," *Proceedings of the Conference Advances in Neural Information Processing Systems*, vol. 3, pp. 572–577, 1990.

[11] H. Harb and L. Chen, "Gender identification using a general audio classifier," *Proceedings of the International Conference on Multimedia and Expo*, pp. 733–736, Washington, DC, USA, 2003.

[12] X. Li, S. J. Maybank, S. Yan, D. Tao, and D. Xu, "Gait components and their application to gender recognition," *IEEE Transactions on Systems, Man and Cybernetics Part C Applications and Reviews*, vol. 38, no. 2, pp. 145–155, 2008.

[13] J. E. Boyd and J. J. Little, "Biometric gait recognition," in *Advanced Studies in Biometrics: Summer School on Biometrics*, pp. 19–42, LCNS, 2005.

[14] L. T. Kozlowski and J. E. Cutting, "Recognizing the sex of a walker from a dynamic point-light display," *Perception & Psychophysics*, vol. 21, no. 6, pp. 575–580, 1977.

[15] G. Shakhnarovich, L. Lee, and T. Darrell, "Integrated face and gait recognition from multiple views," *Proceedings of the IEEE Conference Computer Vision and Pattern Recognition*, pp. I439–I446, CVPR, Kauai, HI, USA, 2001.

[16] L. Wang, H. Ning, T. Tan, and W. Hu, "Fusion of static and dynamic body biometrics for gait recognition," *IEEE Transactions on Circuits and Systems for Video Technology*, vol. 14, no. 2, pp. 149–158, 2004.

[17] J. Han and B. Bhanu, "Individual recognition using gait energy image," *IEEE Transactions on Pattern Analysis and Machine Intelligence*, vol. 28, no. 2, pp. 316–322, 2006.

[18] L. Wang, T. Tan, H. Ning, and W. Hu, "Silhouette analysis-based gait recognition for human identification," *IEEE Transactions on Pattern Analysis and Machine Intelligence*, vol. 25, no. 12, pp. 1505–1518, 2003.

[19] C. Wang, J. Zhang, L. Wang, J. Pu, and X. Yuan, "Human identification using temporal information preserving gait template," *IEEE Transactions on Pattern Analysis and Machine Intelligence*, vol. 34, no. 11, pp. 2164–2176, 2011.

[20] N. Mansouri, M. Aouled Issa, and Y. Ben Jemaa, "Gait-based human age classifiation using a silhouette model," *IET Biometrics*, vol. 7, no. 2, pp. 116–124, 2017.

[21] Y. Liu, T. C. Robert, and Y. Tsin, "Gait sequence analysis using frieze patterns," *Proceedings of European Conference Computer Vision*, pp. 657–671, Copenhagen, Denmark, 2002.

[22] N. Cuntoor, A. Kale, and R. Chellappa, "Combining multiple evidences for gait recognition," *Proceedings International Conference Acoustics, Speech, and Signal Processing*, pp. 33–36, IEEE, Hong Kong, 2003.

[23] A. Norouzi and A. H. Zaim, "Genetic algorithm application in optimization of wireless sensor networks," *The Scientific World Journal*, vol. 2014, p. 15, 2014.

[24] A. Masuri, O. Medina, S. Hacohen, and N. Shvalb, "Gait and trajectory optimization by self-learning for quadrupedal robots with an active back joint," *Journal of Robotics*, vol. 2020, p. 7, 2020.

[25] J. Luo, J. Tang, and X. Xiao, "Abnormal gait behavior detection for elderly based on enhanced Wigner-Ville analysis and cloud

incremental SVM learning," *Journal of Sensors*, vol. 2016, p. 18, 2016.

[26] S. M. Vasanthi and T. Jayasree, "Performance evaluation of pattern recognition networks using electromyography signal and time-domain features for the classification of hand gestures," *Proceedings of the Institution of Mechanical Engineers. Part H*, vol. 234, no. 6, pp. 639–648, 2020.

[27] A. H. Lenin, S. M. Vasanthi, and T. Jayasree, "Automated recognition of hand grasps using electromyography signal based on LWT and DTCWT of wavelet energy," *International Journal of Computational Intelligence Systems*, vol. 13, no. 1, pp. 1027–1035, 2020.

Hindawi
International Journal of Polymer Science
Volume 2022, Article ID 9047554, 19 pages
https://doi.org/10.1155/2022/9047554

Review Article

A Review on Polyaniline: Synthesis, Properties, Nanocomposites, and Electrochemical Applications

Abdulwahhab H. Majeed,[1] **Leqaa A. Mohammed**,[1] **Omar G. Hammoodi**,[1] **Shankar Sehgal**,[2] **Mustafa A. Alheety**,[3] **Kuldeep K. Saxena**,[4] **Safaa A. Dadoosh**,[1] **Israa K. Mohammed**,[1] **Mustafa M. Jasim**,[1] **and N. Ummal Salmaan**[5]

[1]*Department of Chemistry, College of Science, Diyala University, Diyala, Iraq*
[2]*Mechanical Engineering, UIET, Panjab University, Chandigarh, PB 160014, India*
[3]*Department of Nursing, Al-Hadi University College, Baghdad, Iraq*
[4]*Department of Mechanical Engineering, GLA University, Mathura, UP 281406, India*
[5]*Department of Automotive Engineering, Aksum University, Axum, Ethiopia*

Correspondence should be addressed to N. Ummal Salmaan; ummalsalmaan90@gmail.com

Received 20 June 2022; Revised 11 July 2022; Accepted 19 September 2022; Published 14 October 2022

Academic Editor: Temel Varol

The development in the use of polyaniline (PANI) in advanced studies makes us draw attention to the presented research and combine it into one study like this one. The unique composition of PANI qualifies it for use in electrochemical applications in addition to many other applications whose use depends on its mechanical properties. Based on this, it is necessary to limit the reactions that produce PANI and the cheapest cost, and then limit the current uses in the formation of nanocomposites with metals, their oxides, and/or carbon nanocomposites in order to determine what is missing from them and work on it again to expand its chemistry. The development in the use of PANI in advanced studies makes us draw attention to the research presented on PANI and combine it into one study. One of the very important things that made PANI possess a very huge research revolution are preparation in a variety of ways, easy and inexpensive, from which a daily product can be obtained with very high purity, as well as its distinctive properties that made it the focus of researchers in various scientific departments. The unique structure of PANI, which is easy to prepare in its pure form or with various chemical compounds including metals, metal oxides, and carbon nanomaterials (such as carbon nanotubes, graphene, graphene oxide, and reduced graphene oxide), qualifies it for use in electrochemical applications. The various studies reviewed showed that PANI gave good results in the applications of super capacitors. In some of the studies mentioned later, it gave a specific capacitance of 503 F/g, cycle stability 85% at 10,000 cycles, energy density 8.88 kW/kg, and power density 96 W h/kg. It was also noted that these values improved significantly when using PANI with its nanocomposites. Because of its good electrical conductivity and the possibility of preparing it with a high surface area with nanostructures in the form of nanowires, nanofibers, and nanotubes, PANI was used as a gas sensor. We have noticed, through the studies conducted in this field, that the properties of PANI as a basic material in gas sensors are greatly improved when it is prepared in the form of PANI nanocomposites, as explained in detail later. From this review, we tried with great effort to shed light on this attractive polymer in terms of its different preparation methods, its distinctive properties, its nanocomposites, and the type of polymerization used for each nanocomposites, as well as its applications in its pure form or with its nanocomposites in the supercapacitor and gas sensor applications.

1. Introduction

During the past few decades, nanomaterials, polymeric materials, and hybrid materials [1–6] have aroused a distinguished interest in the world of scientific research due to their distinctive chemical and physical properties and their various applications in photonics, electronics, sensors, conductive materials, biotechnology, medicine, and pollution control

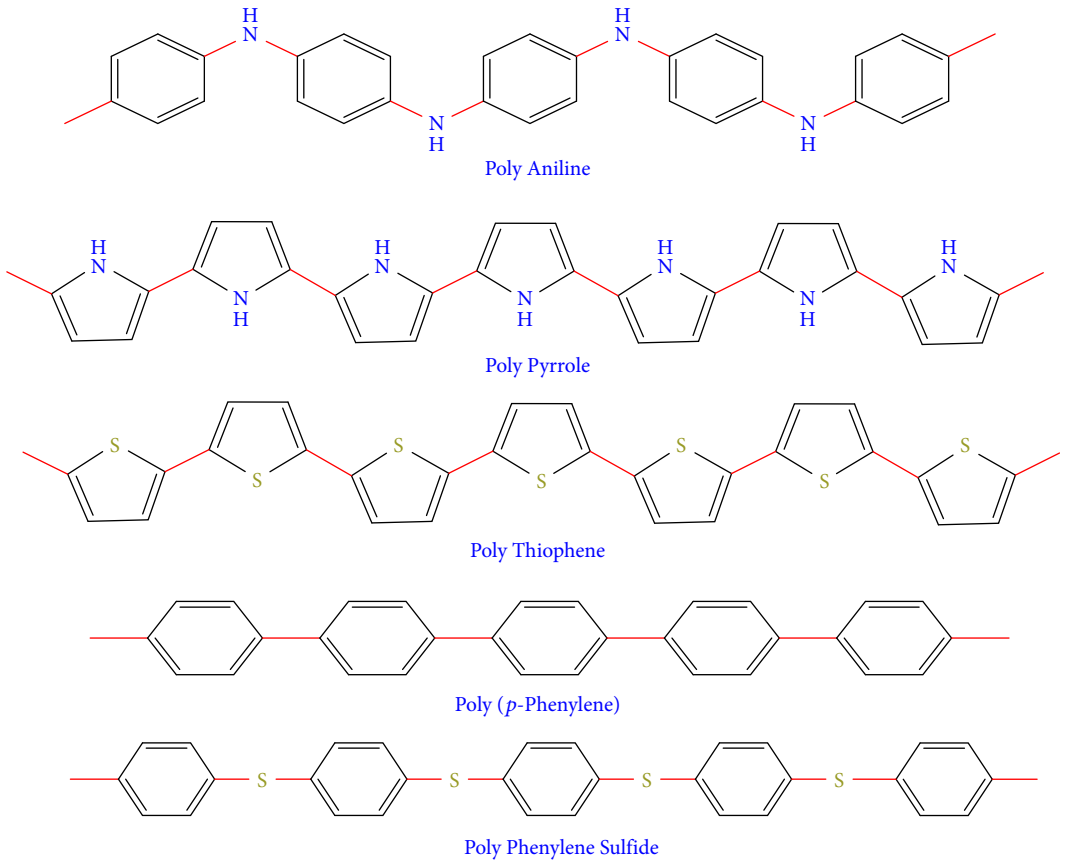

Figure 1: Structure of some conductive polymers.

[7–15]. Conductive polymers are among the important classes of polymers that have become popular in recent decades because of their high efficiency, which made them distinguished in the field of electrical conductivity and energy storage [16–18]. Polyaniline (PANI) and its derivatives, polypyrrole, polythiophene, poly(para-phenylene), and polyphenylene sulfide (Figure 1), are among the most widely used classes of conductive polymers in recent times because of their good electrical properties that can be controlled, their good environmental stability, their cheapness, and their easy preparedness [19–21].

2. Polyaniline

PANI is the most important of these polymers mentioned, which has been used in research as an advanced polymeric material during the last decade, because it is a polymer rich in electrons and has good electrical conductivity, as well as it has a good ability to modify and processing [22]. PANI has been used in many applications including solar cells [23], lithium batteries [24], supercapacitors [25], fuel cells [26], flexible electrodes [27], corrosion-resistant coatings [28], water pollutant removal [29], screen printing [30], and sensors [31]. MacDiarmid (1997) suggested different kinds of basic PANI. He proposed three idealized oxidation state structures including completely reduced leucoemeraldine base (LEB), semi-oxidized emeraldine base (EB), and fully oxidized pernigraniline base (PAB; Figure 2). The EB is the greatest broadly studied PANI type [32, 33].

Different forms of PANI display various colors like leucoemeraldine structure of PANI is colorless or white in color, emeraldine type is blue in base structure and green in salt form, and pernigraniline structure is blue to violet color. Using protonic acids and oxidative doping procedures, EB can be converted into a conducting state (Figure 3), but this process cannot be performed for LEB and PAB [34–36].

The color change associated with PANI in different oxidation states can be used in sensors and electrochromic devices [37]. The best method for making a PANI sensor is arguably to take advantage of the dramatic conductivity changes between the different oxidation states or doping levels [38].

3. Synthesis of PANI

PANI is considered one of the attractive electrical conductive polymers, because it can be easily converted between base and salt forms easily by adding base (OH^-) or acid (H^+). The properties of reduction and oxidation, good electrical conductivity, easy method of preparation, and modification in addition to its environmental stability made PANI one of the most conductive polymeric materials that the researchers dealt with in their work. In the past, the

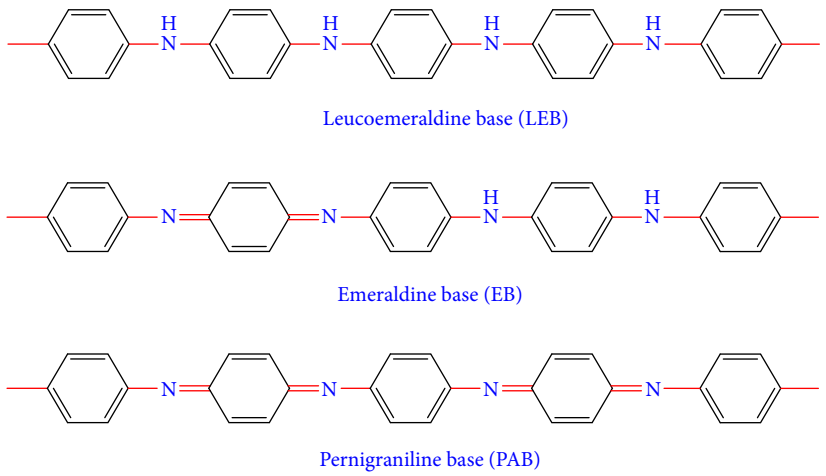

Figure 2: The chemical structures of different forms of polyaniline.

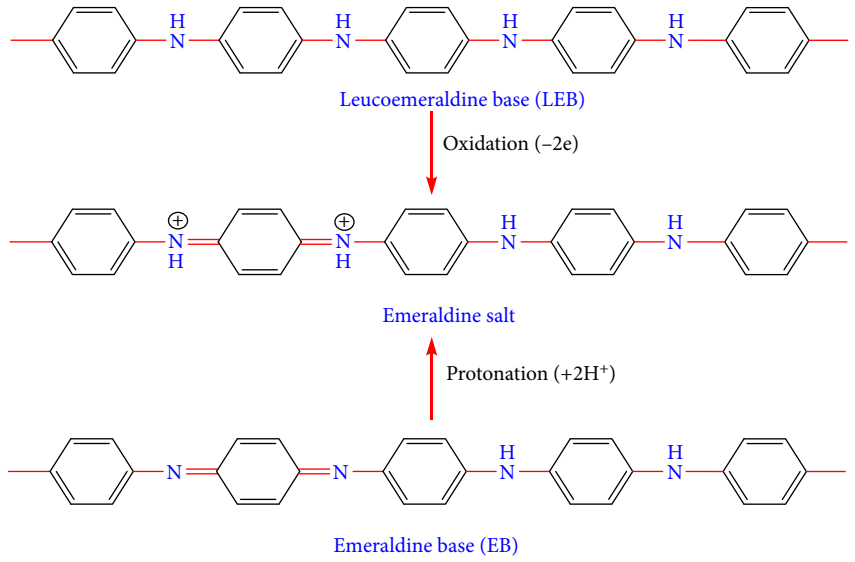

Figure 3: Formation of emeraldine salt from leucoemeraldine structure by oxidation and from emeraldine base by protonation.

oxidative polymerization of aniline monomers in an acidic medium was used to prepare PANI, but with the development of work and research on PANI, different methods and techniques were used to prepare it, including [39]:

1. Electrochemical polymerization.
2. Chemical polymerization.
3. Vapor-phase polymerization (VPP).
3. Photochemically initiated polymerization.
4. Enzyme-catalyzed polymerization.
5. Polymerization employing electron acceptors [39].

3.1. Electrochemical Polymerization. The electrochemical method for preparing conductive polymers plays an important role in the preparation, because in many applications, it is required to prepare polymers in the form of a thin film with a wide surface area. When conductive polymers are prepared using the chemical method, it is difficult to follow the electrochemical process of the prepared polymers, because the study of electrical and optical properties depends mainly on these thin layers of polymer deposited on the electrode. This method of preparing conductive polymers is similar to the electrodeposition method used in metals. Electrodynamic and galvanic techniques were used to prepare PANI as electrochemical methods. The electrochemical method used in the preparation includes many advantages over the chemical method, which is cheap and easy to operate, giving a very pure and homogeneous polymer deposited on the electrode; in addition, the process takes place in a simple chamber cell containing a power source, an electrode, and an electrolyte solution [40, 41].

The electro-polymerization method to prepare PANI follows the next steps: (1) formation of a positive free radical (cationic free radical) of aniline monomers by oxidation at the anode, (2) the combination of the structures formed in the first step to form dimers through the process of removing protons and rearranging electrons in the aromatic rings, (3) the growth of these formed dimers and the formation of new, larger structures, (4) the last step is the spontaneous activation of the polymeric chain formed by the acid present in the solution to obtain the resulting denatured PANI, and this

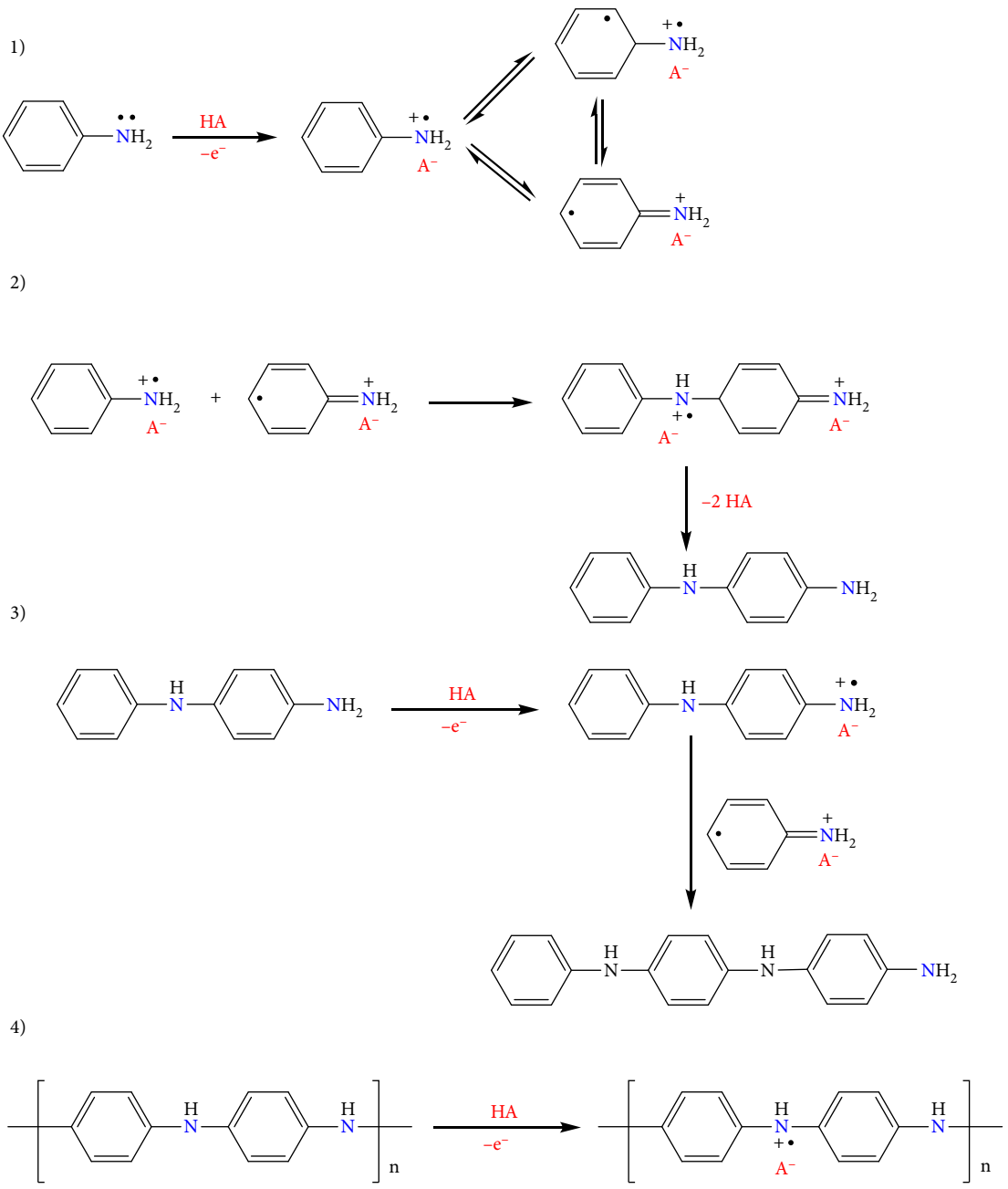

Figure 4: Proposal mechanism to form PANI using electrochemical polymerization.

is the proposed mechanism for the electro-polymerization of PANI (Figure 4) [41, 42].

3.2. Chemical Polymerization. The chemical method (oxidative polymerization) for the preparation of polymers is characterized as a simple and cheap method capable of preparing large quantities of polymers within a short time. Until now, it is the common method used by many companies to prepare PANI [43].

In this method, the oxidizing force that initiates the polymerization process is provided by adding a chemical oxidizing agent to the solution. Ammonium persulfate ($(NH_4)_2S_2O_8$), sodium vanadate ($NaVO_3$), cerium sulfate ($Ce(SO_4)_2$), hydrogen peroxide (H_2O_2), potassium iodate (KIO_3), potassium dichromate ($K_2Cr_2O_7$), and others were used as oxidizing agents during the polymerization process [44]. In addition, ammonium persulfate ($(NH_4)_2S_2O_8$) is one of the most widely used oxidizing materials in this method. Usually, ammonium persulfate is used in the polymerization of aniline in an acidic medium (pH ≤ 3), in order to be suitable for dissolving the aniline, to stimulate the initiation of the polymerization process, and to avoid the formation of unwanted by-products. The usually used molar ratio between persulfate and aniline (APS/Aniline) is less than 1.2 [45].

The mechanism of polymerization of aniline by ammonium persulfate occurs in its initial stages through a

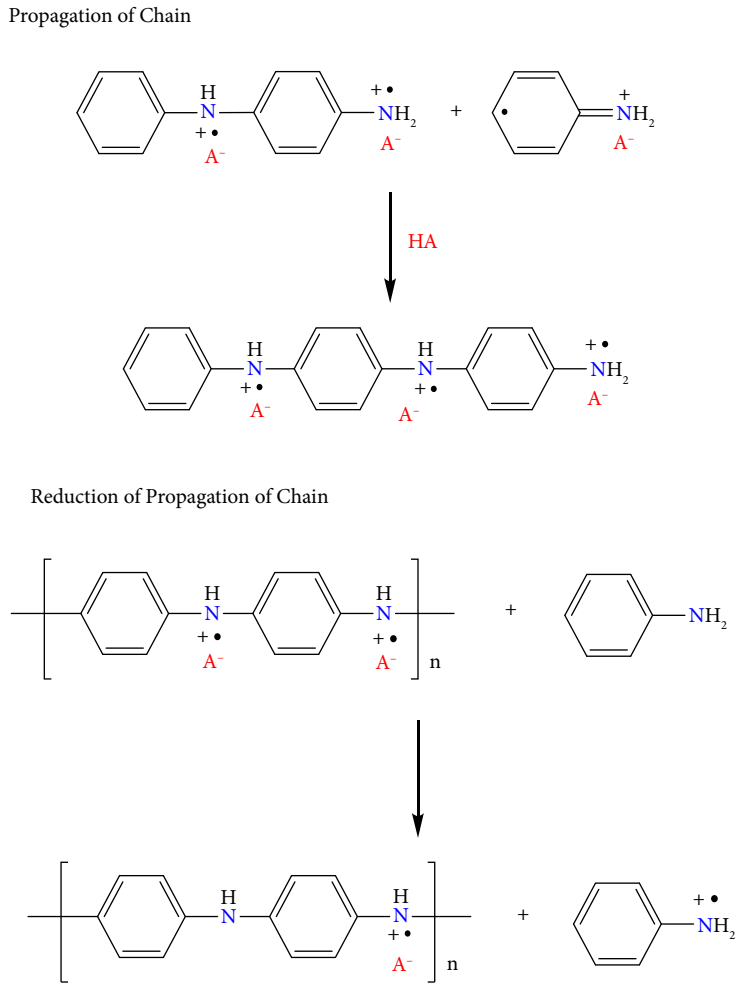

Figure 5: Chemical (oxidative) polymerization of aniline [39, 50].

mechanism similar to the mechanism of polymerization of aniline by electrochemical method as described previously [46–48]. The first stage includes the formation of the radical cation of aniline by capturing nitrogen electrons with ammonium persulfate [49].

In the second step, the reaction occurs between the nitrogen radical cation with the radical cation in the para-site of another aniline molecule, and the reaction continues (Figure 5). Mostly, the interaction between the radical cation of nitrogen in the first aniline molecule with the radical cation occurs in the *para* site of the second aniline molecule, but sometimes, the reaction occurs with the radical cation in the *ortho* position with the second aniline molecule, and this leads to a distortion of the resulting PANI chains [39].

3.3. Vapor-Phase Polymerization. One of the important processes of PANI synthesis is VPP. This method was used for the first time to deposit conductive PANI on cotton threads in 1998, by saturating cotton threads with ammonium persulfate $(NH_4)_2S_2O_8$, then passing aniline steam over cotton threads to be coated with conductive PANI [51].

VPP technology is used to manufacture ultra-thin polymer films, such as PANI, polypyrrole, polythiophene, and others. This process is one of the techniques of self-assembly polymerization that takes place under the vapor phase, which can easily prepare thin films of polymers with very high purity and with superconductivity, because they are free of impurities, as well as the possibility of preparing them at the nanoscale [44, 52, 96, 97].

3.4. Photochemically Initiated Polymerization. Photocatalytic polymerization is a promising and attractive method for producing PANI with unique properties and compositions. In addition, it is a very important method for the production of hybrid materials [53]. In 1998 [54] and 2001 [55], Kobayashi and co-workers demonstrated that it is possible to prepare PANI by photopolymerization using single- or bi-layer films containing $[Ru(bipy)_3]^{2+}$ as a primer and methylviologen (MV^{2+}) as an oxidizer, then irradiated with visible light to give PANI. $[Ru(bipy)_3]^{2+}$ is irradiated at the 452 nm region, and this leads to the generation of the triple excited state $^*[Ru(bipy)_3]^{2+}$. The process of electron transfer between $^*[Ru(bipy)_3]^{2+}$ and MV^{2+} leads to the generation of the strong oxidizer $[Ru\ (bipy)_3]^{3+}$, which is responsible for the process of oxidation of aniline and then polymerization of the latter to PANI. In these studies, the formed PANI

was deposited on monolayer or bilayer films to be used later in molecular electronics.

Later, different techniques were used for the irradiation process to form PANI using an external source, including gamma rays [56], microwaves [57], ultraviolet rays [58], and X-rays [59].

3.5. Enzyme-Catalyzed Polymerization. The researchers in the past years have resorted to using enzymes, such as horseradish peroxidase (HRP), as catalysts for the synthesis of some important polymers, such as PANI and poly pyrrole in the presence of oxidants, such as peroxide [60, 61]. This method is considered environmentally friendly, because the peroxide is converted to water, but several studies have produced branched polymers with low molecular weight. To overcome these problems, Samuelson et al. [62, 63] used various electrolytes, such as poly(styrene sulfonate) (PSS) as templates in the HRP-catalyzed PANI preparation mixture to produce regular polymeric chains. PSS plays three roles in this process:

(i) PSS acts as a template that aligns the aniline monomers before starting the polymerization process in order to arrange the monomers in the desired head-to-tail coupling position.

(ii) It provides important doping in the process of activating PANI into the form of electrically conductive emeraldine salt.

(iii) It imparts the water solubility of the (PAni/PSS) product [64].

In this method, the polymerization process takes place in an acidic medium at (pH = 4), in which water-soluble PANI is obtained [65]. The good electrolytes used are poly(vinylphosphonic acid) and DNA, as well as PSS [66, 67].

4. Properties of PANI

4.1. Physical Properties. PANI has various physical properties, depending on its three forms, where these forms show different colors according to their chemical nature. PANI appears white/clear or colorless if the polymer form is leucoemeraldine, and if the polymer type is pernigraniline, it gives blue to violet color, and if the polymer form is emeraldine, it gives blue color if it is basic and gives green color if it is salt form. PANI also has good electrical conductivity only in the emeraldine form, and the other types do not show significant conductivity [37]. As for solubility, all forms of PANI are insoluble in water, acetone, ethanol, and other solvents, but are soluble in dimethylformamide, dimethyl sulfoxide, and *N*-methyl-2-pyrrolidone [37, 68, 69].

4.2. Optical Properties. The optical properties of PANI are used to study the oxidation level and protonation process of the polymer. Huang and MacDiarmid observed that when leucoemeraldine was converted from its base form to its salt form, a blue shift occurred from 3.94 to 4.17 eV. This shift occurred due to the excitation of electrons between the locally occupied upper molecular orbital (HOMO) to the lower unoccupied molecular orbital (LOMO), where the absorption peak was observed at 2.1 eV [70]. Barbero and Kötz studied the optical properties of PANI films deposited on gold, and two absorption states appeared in the UV–visible region of the oxidized state of the polymer, the first at 3.8 eV (which is due to the π–π^* transition*) and the second at 2.75 eV (which is related to the n-to-π^* transition), as it has one absorption band at 1.5 eV near infrared and is due to the transition entering the band [71].

For emeraldine conductive PANI in its salt form, there are predictions of molecular orbital calculations, and later (ab initio calculations), where these studies show the presence of a single broad polaron band within the band gap. This band is half full, resulting in a signal in the ESR scan. Calculations of this band structure are consistent with the observed UV–visible and infrared spectra [72, 73]. The emeraldine salt in their compact coil structure shows three bands: the first band at 330 nm, which is assigned to (π–π^* band transitions), and two visible-region bands at 430 nm, which is attributed to ($\pi \rightarrow$ polaron band), and 800 nm, which related to (polaron $\rightarrow \pi^*$) [74].

4.3. Mechanical Properties. PANI shows a noticeable difference in mechanical properties according to the polymerization method from which it was prepared. Emeraldine salts prepared by electropolymerization method are highly porous and have poor mechanical properties. In addition, PANI films prepared by electropolymerization method have poor mechanical properties, so they are not used frequently. As for PANI prepared from solutions, it is more rigid and is widely used as films and fibers, because it has less porosity and better mechanical properties [39]. The first to study the mechanical properties of PANI are Wei et al., where they noticed that a layer of PANI with a thickness of 0.07 + 0.03 mm at a temperature of 25°C and under nitrogen atmosphere showed a storage modulus of ~200 MPa [75].

4.4. Electrical Properties. PANI is an attractive conductive polymer that is widely used in the electrical field, because it has good electrical conductivity in its emeraldine salt form. When the acid is added with the basic emeraldine of PANI, it works on protonating the imine group's nitrogen, thus converting it into a salt, thus turning from the non-conductive form to the electrically conductive polymer [37]. Generally, the range of PANI conductivity is from $\sigma \leq 10^{-10}$ S/cm (undoped base emeraldine) to $\sigma \geq 10$ S/cm (doped salt emeraldine) [76, 77]. The process of improving the electrical conductivity or increasing the number of different properties of PANI simultaneously is coupled with the doping process of the polymer. In recent decades, many researchers in the world have tended to dope PANI with various classes of chemical compounds for use in different applications. The purpose of this is to improve the electrical conductivity of the new compounds prepared (polymer compounds) to be used in that application [37, 78]. Table 1 shows the electrical conductivity of the items prepared with PANI.

4.5. Anti-Corrosion Properties. Corrosion is a chemical change to the metal due to the environmental influences

Table 1: Electrical conductivity of polyaniline and/or its composites.

No.	PANI system	Dopant	Conductivity S/cm	References
1.	PANI-SAP	Sulfonic aminophenol	0.13×10^{-3}	[79]
2.	PANI-H_2SO_4	Sulfuric acid	1.09	[80]
	PANI-NA	Nicotinic acid	0.63	
	PANI-MNA	2-Methyl nicotinic acid	0.089	
3.	PANI	Molybdenum disulfide	1.09×10^{-1}	[81]
	MoS_2/PANI-8		2.5×10^{-1}	
	MoS_2/PANI-38		2.38	
4.	FTO/PANI	Florine doped tin oxide (FTO) and graphene (GR)	0.09	[82]
	FTO/PANI-GR 1 mg		0454	
	FTO/PANI-GR 3 mg		4.76	
5.	GO-PANI	Graphene oxide	0.1	[83]
6.	PANI	Carbon black (CB)	0.01	[84]
	PANI/CB	Graphite (GR)	0.03	
	PANI/GR	Multi-wall carbon nanotubes (MWCNTs)	0.07	
	PANI/MWCNTs		2.28	
7.	PANI		0.50	[85]
	PANI/MWCNTs	MWCNTs	1.95	
8.	PANI-Au	Gold (Au)	2.13×10^{-4}	[86]
	PANI-Au-CSA	Camphor sulfonic acid (CSA)	5.42×10^{-3}	
9.	PANI	Tin dioxide (SnO_2)	0.21	[87]
	PANI-SnO_2 (0.02 g)		2.6×10^{2}	
	PANI-SnO_2 (0.05 g)		3.1×10^{2}	
10.	PANI	Silver NPs (Ag)	3.3×10^{-3}	[88]
	PANI/Ag		5.2×10^{-2}	
11.	PANI 9%–DBSA/DVB	Dodecylbenzenesulfonic acid (DBSA) Divinylbenzene (DVB)	0.01	[89]
12.	PANI 13%–DBSA/PC	Polycarbonate (PC)	0.01	[90]
13.	PS/(PANI–DBSA) 30%	Polystyrene (PS)	0.001	[91]
14.	PANI 0%/PVA-g-PAA	Poly(vinyl alcohol) (PVA)–g–poly(acrylic acid) (PAA)	0.01	[92]
	PANI 5%/PVA-g-PAA		0.04	
15.	RGO/PANI/EVA	Reduced graphene oxide (RGO) and ethylene vinyl acetate (EVA)	1.7×10^{-1}	[93]
16.	PANI–TiO_2	Titanium dioxide (TiO_2)	1×10^{-5}	[94]
17.	PANI		2.6×10^{-2}	[95]
	PANI–TiO_2 (15%)	Titanium dioxide (TiO_2)	3.8×10^{-2}	
	PANI–TiO_2		4.8×10^{-2}	
18.	PANI-NC	Nanoclay (NC)	2.143	[96]
19.	PVA/PANI/Ni	Poly(vinylalcohol) (PVA) and nickel nanoparticles (Ni)	4.9	[97]

surrounding it, and it is one of the major problems facing the various processes that use the metal as a base element in their applications. Many materials have been used to end or reduce the corrosion process, and one of these materials is PANI, which was first reported in the 1980s [41]. PANI was used to effectively protect steel from oxidation (corrosion) when it was used with fuel cells at the same time. Research and studies have proven that preparing layers of sulfate with PANI is much better and more suitable for reducing the corrosion of steel than layers of PANI with phosphate [98]. The materials prepared from PANI molybdate and PANI tungstate as coating materials to reduce steel corrosion were studied by Kamaraj et al. [99]. Likewise, with nickel-plated steel, the PANI coating showed great protection for this steel from corrosion [100]. In addition, Mirmohseni and Oladegaragoze used PANI-coated iron in different corrosive environments to study the corrosion potential and corrosion current [101].

4.6. Semiconducting Properties. PANI is considered one of the most promising materials in the field of electronics due

Table 2: Summary of some polyaniline nanocomposites synthesis with metal nanoparticles.

No.	PANI nanocomposite type	Dopant	Preparation method	References
1.	PANI/Au	Au	In situ interfacial polymerization	[123]
2.	PANI/Ag	Ag	Oxidative polymerization	[124]
3.	PANI/Ag	Ag	In situ photo-redox mechanism	[125]
4.	PANI/Ag	Ag	In situ polymerization	[126]
5.	PANI/Fe	Fe	Sonochemical method	[127]
6.	PANI/Ni	Ni	Oxidative polymerization	[128]
7.	PANI/Cu	Cu	Electrochemical polymerization	[129]
8.	PANI/Pd	Pd	Templating method	[130]
9.	PANI/Pt	Pt	In situ interfacial polymerization	[131]
10.	PANI/Pr	Pr	Oxidative polymerization	[132]
11.	PANI/Se	Se	Oxidative polymerization	[133]
12.	La/Cd/PANI	La/Cd	Graft copolymerization method	[134]
13.	PANI/CdS	CdS	Facile chemical methods	[135]
14.	PANI/PbS	PbS	Chemical oxidation technique	[136]
15.	PANI/Au Pd	Au Pd	Oxidative polymerization	[137]

to its good conductivity of electrons. The results of electrical and thermal conductivity of the ionic liquid of PANI showed that this polymer is a p-type semiconductor, and the diode of PANI was prepared by Yakuphanoglu and Şenkal [102]. On the other hand, PANI films doped with boric acid were prepared, then the electrical properties of these films were examined. It was found that PANI films doped with boric acid show semi-conductive properties, and its electrical conductivity was found 1.02×10^{-4} S/cm at room temperature. The optical band gap of the PANI films doped with boric acid was 3.71 eV. Because of these semiconducting properties, PANI is widely used in organic field transistors and in solar batteries [103].

4.7. Capacitive Properties. PANI has been widely used in recent years in various electrical and electronic devices, especially electrical storage devices, such as the super capacitor. PANI has contributed to improving the properties of these energy-saving devices due to the rapid oxidation and reduction reactions that occur in a large part of the polymer material. PANI gives a good capacitive response and produces superior specific energies compared to double-layer capacitors. Moreover, PANI has a stronger effect than inorganic batteries and also has remarkable electrical conductivity. However, capacitors made of pure PANI experience contractions in the charge–discharge cycle [41, 104]. To overcome these problems and enhance the properties of the capacitors, researchers resorted to using other compounds with PANI, such as PANI–graphene [105–107], PANI–carbon nanotubes [108–110], PANI–manganese oxide [111], PANI/MoS_2–MnO_2 [112], PANI–silver–manganese dioxide [113], and others. These modifications of the electrodes containing PANI proved to be of great improvement in the increase of energy density, stability, and strength [41].

4.8. Magnetic Properties. Due to its high spin density, PANI shows good interest in magnetic behavior and has been used in many studies [114]. The paramagnetic nature is closely and directly related to the magnetic and electrical properties of electrically conducting PANI, which is caused by the presence of hydrochloric acid as dopant with PANI as a result of the oxidation process [115].

The polymeric composite nanotubes (PANI–Fe_3O_4) have been prepared in [116], and this composite exhibited good magnetic behavior and significant magnetic properties. Similarly, the self-assembly method was used to prepare the polymeric composite (PANI–Fe_3O_4) nanorods. In addition, because hydrogen bonding in methanol and PANI structures actually affects the polarization, it has been observed that there are good magnetic properties of iron in PANI [41].

The rotation sensitivity of PANI refers to the magnetic centers that are found in charge carriers that are implanted in metal fields as well as those along polymer chains. In this spin, the electron comes into contact with the samples, and this leads to clearly showing anti-ferromagnetic properties, such as paramagnetic sensitivity [41, 117].

5. Nanocomposites of PANI

A composite is a new substance resulting from the mixing of two or more materials that are significantly different from each other in properties. The resulting new materials (composites) have different properties or improved properties from those of the parent materials. The idea is to form a new material (composite) to bring out new, diverse, and remarkably progressive properties [118]–[120]. Although PANI exhibits attractive qualities and outstanding properties, there are some limitations in some applications [121]. Making some improvements on PANI, such as combining it with other materials to form polymeric composites, is very important to give higher efficiency in different applications. The process of mixing materials with polymers is the result of polymeric composites, so if the added material is in the

Table 3: Summary of some polyaniline nanocomposites synthesis with metal oxide nanostructures.

No.	PANI nanocomposite type	Dopant	Preparation method	References
1.	PANI/TiO_2	TiO_2	In situ deposition oxidative polymerization	[138]
2.	PANI/MnO_2	MnO_2	Simultaneous-oxidation route	[7]
3.	PANI/MgO	MgO	In situ polymerization method	[139]
4.	PANI/ZnO	ZnO	In situ chemical oxidation method	[140]
5.	PANI/NiO	NiO	Electrodeposition method	[141]
6.	PANI/Fe_2O_3	Fe_2O_3	In situ polymerization	[142]
7.	PANI/γ-Fe_2O_3	γ-Fe_2O_3	In situ polymerization	[143]
8.	PANI/α-Fe_2O_3	α-Fe_2O_3	In situ polymerization	[144]
9.	PANI/CuO	CuO	In situ polymerization	[145]
10.	PANI/Co_3O_4	Co_3O_4	In situ polymerized method	[146]
11.	PANI/V_2O_5	V_2O_5	Chemical oxidation method	[147]
12.	PANI/RuO_2	RuO_2	Chemical bath deposition (CBD) method	[148]
13.	PANI/SnO_2	SnO_2	Chemical oxidative polymerization	[149]
14.	PANI/Sm_2O_3	Sm_2O_3	In situ oxidative polymerization	[150]
15.	CeO_2/PANI	CeO_2	Chemical oxidative polymerization	[151]
16.	PANI/Al_2O_3	Al_2O_3	Surface initialized polymerization (SIP) method	[152]

Table 4: Summary of some polyaniline nanocomposites synthesis with carbon nanocompounds.

No.	PANI nanocomposite type	Dopant	Preparation method	References
1.	PANI/SWCNT	SWCNT	Oxidative polymerization method	[153]
2.	PANI/f-SWCNT	f-SWCNT	Electrochemical polymerization	[154]
3.	PANI/MWCNT	MWCNT	Oxidative polymerization method	[155]
4.	PANI/MWCNT	MWCNT	In situ enzymatic aniline polymerization	[156]
5.	MnO_2/PANT/MWCNT	MnO_2/MWCNT	In situ chemical oxidation polymerization	[157]
6.	MWCNTs/PANI/TiO_2	MWCNT/TiO_2	One-pot polymerization process	[158]
7.	CuO@NiO/PANI/MWCNT	CuO@NiO/MWCNT	Oxidative polymerization method	[159]
8.	PANI/GO	GO	In situ polymerization technique	[160]
9.	CuNPs-PANI-GO	CuNPs-GO	In situ oxidative polymerization	[161]
10.	Ag_3PO_4-PANI-GO	Ag_3PO_4-GO	Interfacial polymerization	[162]
11.	PANI-RGO-ZnO	RGO-ZnO	In situ oxidative polymerization	[163]
12.	PANI/graphene	G	In situ polymerization	[164]
13.	Pt–PANI–graphene	Pt–G	In situ oxidative polymerization	[165]
14.	Polyaniline/fullerene C_{60}	C_{60}	Copolymerization of aniline	[166]
15.	Polyaniline/graphite oxide	Graphite oxide	Interfacial polymerization	[167]

nanoscale dimensions, the new material is called the polymeric nanocomposite. It has been observed that many materials were mixed with PANI to form PANI composites. The additives added to PANI to form PANI composites may be in the form of metals, metal oxides, carbon nanostructures, polymers, or various organic compounds [122]. Table 2 shows the preparation of PANI nanocomposites with metal nanoparticles.

PANI composites were also synthesized with metallic nano-oxides due to their great importance in many applications, such as electrical storage devices, water purification, electronic devices, supercapacitors, sensors, solar cells, and others. Table 3 shows the preparation of PANI nanocomposites with metal oxides and the method of their preparation.

On the other hand, PANI was extensively synthesized with carbon nanocompounds, due to the high properties demonstrated by these prepared nanocomposites compounds. The prepared PANI nanocomposites were used in many different applications and showed high efficiency in the applications used in them. Table 4 shows some PANI nanocomposites with different carbon nanocompounds.

In addition, there is a huge amount of polymeric nanocomposites of PANI in different shapes and structures and with different applications and polymerization techniques, and this is clear evidence of the importance of PANI and its wide uses in the experimental and the industrial field.

Table 5: Some of the different studies used in the applications of supercapacitor based on polyaniline or its nanocomposites.

PANI nanocomposites	Electrolyte	Specific capacitance	Cycle stability	Energy and power density	References
PANI	1 M H_2SO_4	503 F/g	85% (10,000)	96 W h/kg and 8.88 kW/kg	[172]
PANI nanowires	1 M H_2SO_4	742 F/g	92% (1500)	68 W h/kg and 16 kW/kg	[173]
PANI nanofibers	1 M H_2SO_4	548 F/g	75% (1000)	36 W h/kg and 0.12 kW/kg	[174]
Sulfonated PANI	1 M H_2SO_4	1107 F/g	—	31.4 W h/kg and 14.8 kW/kg	[175]
PANI/G/CNT	1 M H_2SO_4	510 F/g	91% (5000)	20.5 W h/kg and 25 kW/kg	[176]
GO/PANI	PVA/H_3PO_4	1095 F/g	—	24.3 W h/kg and 28.1 kW/kg	[177]
PANI/G	EMITFSI/PVDF–HFP	87.8 mF/cm^{-2} at 0.22 mA/cm^{-2}	100% (10000)	12.2 mW h/cm^{-2} and 226.4 mW/cm^{-2}	[178]
Carbonized iron/PANI/G	1 M $NaNO_3$	69.9 F/g	91% (10000)	68 W h/kg and 718.2 W/kg	[179]
G/PANI/MnOx	1 M Na_2SO_4	955 F/g	89% (1000)	61 W h/kg and 4.5 kW/kg	[180]
Polyaniline/G/Fe_2O_3 hydrogel	1 M H_2SO_4	1124 F/g	82% (10000)	14.4 W h/kg and 58 W/kg	[181]
PANI/TiO_2/GO	1 M H_2SO_4	430 F/g	—	—	[182]
PANI/SWCNT	1 M H_2SO_4	485 F/g	—	228 W h/kg and 2250 W/kg	[153]
PANI/MWCNT	1 M $NaNO_3$	328 F/g	94% (1000)	—	[183]
PANI/MnO_2	0.1 M Na_2SO_4	715 F/g	96.5% (5000)	200 W h/kg	[184]
MnO_2/PANI/Hollow mesoporous c	PVA–KOH	248.5 F/g	97.7% (5000)	88.4 W h/kg and 800 W/kg	[185]
PANI/SnO_2	1 M H_2SO_4	305 F/g	95.5% (500)	42 W h/kg	[186]
PANI/V_2O_5	5 M LiCl	443 F/g	92% (5000)	69 W h/kg and 0.72 W/kg	[187]
PANI/MoS_2	1 M H_2SO_4	575 F/g	98% (500)	265 W h/kg and 18 W/kg	[188]
MnO_2/PANI/MWCNTs	1 M KOH	395 F/g	72% (1000)	—	[157]
PANI coated RuO_2/TiO_2	0.1 M H_2SO_4	67.4 F/g	81.6% (10,000)	3.37 W h/kg and 60 W/kg	[189]
PANI-RGO-ZnO	1 M H_2SO_4	40 F/g	86% (5000)	5.61 W h/kg and 403 W/kg	[163]
CuO@NiO/PANI/MWCNT	3 M NaOH	1372 F/g	83% (1500)	—	[159]
PANI/rGO-Co_3S_4	1 M H_2SO_4	767 F/g	81.7% (5000)	61.2 W h/kg and 8.8 kW/kg	[190]
PANI/MoO_3/G	1 M H_2SO_4	593 F/g	92.4% (1000)	55.5 W h/kg and 1678.99 W/kg	[191]

6. Application of PANI

Conductive polymers, since their discovery until now, have shown very unique properties due to their distinctive electronic arrangement, chemical nature, and due to their diverse physical specifications, and this makes them essential materials in many different applications. For example, PANI is a good electrical conductive polymer, and due to its low cost, ease of preparation, unique properties, and non-polluting of the environment, it attracts the interest of many researchers for its use in many applications. The most important applications in which PANI is used as a main material or as a secondary material are as follows.

6.1. In Supercapacitor. The world economy has played a very important role in the use of multiple sources of energy, such as natural gas, fossil fuels, and gas. The use of this fuel provides good energy, but it causes many environmental problems. Therefore, it has become very necessary to replace the traditional energy system with alternative energy sources. For this, scientists have always sought to develop and produce environmentally friendly, high-energy, and renewable energy sources, such as water energy, supercapacitors, wind energy, and fuel cells. Super capacitors are considered one of the most promising energies and of great commercial importance in the future markets, because they are used in many different applications, such as electrical and electronic devices and wearable devices. The main difference between super capacitors and conventional is that super capacitors have a capacity for storing energy 1000 times more than dielectric capacitors, as well as their long life, and show high-energy density and have fast charging and discharging [168].

Table 6: Some different studies on sensors based on polyaniline or one of its nanocomposites.

Sensory system	Analytes	Sensitivity % at ppm	Range (ppm)	Response time	Recovery time	Detection limit	References
PANI	NH_3	140% for 100 ppm	1–2000 ppm	60 s	240 s	—	[201, 203]
PANI-MWCNTs	NH_3	320% for 100 ppm	0.9	20 min	40 min	50 ppm	[204]
PANI-MWCNT	CO	6.8–26.7%	—	76 s	210 s	—	[205]
PANI-SWCNT	NH_3	5.8%	0.1–100	—	—	0.05 ppm	[206]
PANI-SWCNT	NO_2	1.9%	0.5–80	—	—	0.5 ppm	[206]
PANI-SWCNT	H_2S	3.6%	2–100	—	—	0.5 ppm	[206]
PANI/Co_3O_4	CO	8.6%	—	140 s	90 s	—	[207]
PANI/TiO_2 nanorods	NH_3	75% for 100 ppm	1	40 s	400 s	20 ppm	[208]
PANI-SnO_2 NPs	NH_3	8% for 100 ppm	0.08	10 s	150 s	100 ppm	[209]
SnO_2/rGO/PANI	H_2S	9.1% for 0.1 ppm	0.1	—	—	0.05 ppm	[210]
PANI/TiO_2 nanofibers	NH_3	180% for 0.2 ppm	0.33	20 s	50 s	25 ppb	[211]
PANI/TiO_2	Acetone	0.5%	15–50	—	—	10 ppm	[212]
PANI/TiO_2	Ethyl acetate	0.06%	10–80	—	—	10 ppm	[212]
PANI/TiO_2	Toluene	1.4%	2–35	—	—	2 ppm	[212]
PANI/TiO_2	Ethanol	2.1%	1–35	—	—	0.5 ppm	[212]
PANI/AuNPs	H_2S	—	0.1–8000	—	—	0.1 ppm	[194]
PANI/rGO	NH_3	50%	0.01	1000 s	50 s	5 ppm	[213]
PANI/Ag NPs	NH_3	200%	1.2	20 min	30 min	100 ppm	[214]
PANI/Au/Al_2O_3	Acetone	0.06	30–300	—	—	30 ppm	[215]
PANI-PMMA fibers	Ammonia	550% for 30 ppm	27	200 s	300 s	1 ppm	[216]
PANI/In_2O_3	NH_3	90% for 93 ppm	0.7	10 s	60 s	23 ppm	[217]
PANI/acrylic acid	Ammonia	2%	1–600	—	—	1 ppm	[218]

Supercapacitors can be divided into three main types, which are as follows: (i) double-layer electrostatic capacitors, whose electrodes are mostly carbon materials, such as carbon, carbon nanotubes, and graphene, (ii) pseudo-electrochemical capacitors, whose electrodes are mostly made of conductive polymers and metal oxides, and (iii) hybrid pseudocapacitors, which are a mixture between the above two types [121, 169].

The electrode materials used in supercapacitors have a very important role on the efficiency of the storage device and the energy conversion process. The electrodes used in supercapacitor devices depend on the use of carbon materials, metals, and conductive polymers [170]. Although supercapacitors using various carbon materials exhibit significant energy density, good conductivity, and adequate durability, their energy density is low. As for metals, they show very appropriate electrochemical properties when used in super-capacities, but their abundance in nature, difficulty in obtaining them, and high cost limit their use for this purpose. Because of its different oxidation states, high conductivity, and specific capacitance, PANI can be used with great success in supercapacitors. In addition, the flexible electrochemical properties of PANI make it very suitable to be strongly used in the manufacture of supercapacitor electrodes. The electrochemical properties of supercapacitors in which PANI is used as a base material in the electrodes depend on the properties of the PANI itself, such as synthesis method, chemical/physical properties, dopant, and nanostructure of PANI [171]. Various carbon compounds were used with PANI to prepare the supercapacitors, such as graphene, fullerene, carbon nanotubes, and graphene oxide. Metal nanomaterials with PANI were also used for the same purpose. Table 5 shows the use of various types of materials with PANI to prepare the super capacitors.

There are also a very large number of polymeric nanocomposites of PANI used in supercapacitors, and they gave good efficiency while using as supercapacitors.

6.2. In Sensors. The device that can show the occurrence of various changes in its environment and detect the presence of other things is called a sensor. The common sensors at present are composed of organic or inorganic semiconducting materials or films [192]. One of the materials that have gained great demand in recent times for the manufacture of sensors is conductive polymers. PANI is one of these polymers, which has received great interest as sensors due to its different structures and morphologies in which it can be prepared, such as microstructures, nanowires, nanotubes, nanoparticles, and nanosheets [193]. Using PANI or one of its nanocomposites, various sensors have been manufactured, such as chemical and biological sensors. Researchers have tried to prepare PANI with different nanostructures, such as nanofibers, nanowires, and nanotubes; then, these nanostructures were used in gas sensors because of their very high surface area and the possibility of gas emission. Pure PANI cannot detect H_2S gas alone, because H_2S gas molecules cannot change the conductivity of PANI, so gold nanoparticles are grafted with PANI to form gold nanocomposites with PANI, and this new system can easily detect H_2S gas, and the

response rate reaches very low concentrations (0.1 ppb) [194]. PANI nanostructures were also used to sense the presence of ammonia, hydrochloric acid, hydrazine, chloroform, carbon oxides, and methanol Table 6, and this led to a noticeable structural change in the PANI nanostructure chains [38]. The sensing property of PANI can be improved by adding different nanomaterials to form PANI nanocomposites, as this reduces the sensing time and leads to the detection of materials or gases even in very low concentrations [193, 195–202].

7. Conclusions

Providing polymeric composites with metals or their oxides in addition to various other composites in order to improve some properties is the subject of all investigations now. Because PANI originally has unique electrical properties, it always attracts the attention of researchers in their studies as well as in various applications, the most important of which is electrical applications. We concluded during this study that it is possible to improve the electrical properties of PANI to be used in sensor applications as well as in other applications.

The recent discoveries in the chemistry of PANI made researchers to devote their efforts to research in this field. It appeared to PANI with important specifications that made it preferred over the rest of the other polymers. One of the most important properties of PANI is its electrical conductivity and its various applications, which opened new horizons for researchers to research in this field. It was found that PANI possesses real electrical properties that made it a cornerstone in many applications that could be of great help to humanity in their lives, including super capacitors, solar cells, all kinds of sensors, batteries of all kinds, and fuel cells. It was also found that the electrical properties of PANI are significantly improved when it is grafted with some nanomaterials to form PANI nanocomposites. We concluded, during this study, that it is possible to improve the properties of PANI by grafting it with other materials, especially nanomaterials, to form polymeric nanocomposites of PANI, and that the latter can improve the applied properties of supercapacitors, gas sensors, and others, as documented in this study.

Data Availability

The data used to support the findings of this study are included within the article.

Conflicts of Interest

The authors declare that they have no conflicts of interest.

Acknowledgments

The authors express their thanks to the industrial and organic chemistry laboratories staff at the Department of Chemistry, College of Science, University of Diyala, Baqubah, Iraq, for their effective contribution to collecting information about PANI and its composites and arranging it for the success of this study in the service of researchers around the world.

References

[1] M. M. Shameem, S. M. Sasikanth, R. Annamalai, and R. G. Raman, "A brief review on polymer nanocomposites and its applications," *Materials Today: Proceedings*, vol. 45, pp. 2536–2539, 2021.

[2] N. F. Alheety, A. H. Majeed, and M. A. Alheety, "Silver nanoparticles anchored 5-methoxy benzimidazol thiomethanol (MBITM): modulate, characterization and comparative studies on MBITM and Ag-MBITM antibacterial activities," *Journal of Physics: Conference Series*, vol. 1294, no. 5, p. 52026, 2019.

[3] A. Kamal, M. Ashmawy, A. M. Algazzar, and A. H. Elsheikh, "Fabrication techniques of polymeric nanocomposites: a comprehensive review," *Proceedings of the Institution of Mechanical Engineers, Part C: Journal of Mechanical Engineering Science*, vol. 236, no. 9, pp. 4843–4861, 2022.

[4] L. A. Adnan, N. F. Alheety, A. H. Majeed, M. A. Alheety, and H. Akbaş, "Novel organic-inorganic nanohybrids (MnO_2 and Ag nanoparticles functionalized 5-methoxy-2-mercaptobenzimidazole): one step synthesis and characterization," *Materials Today: Procedings*, vol. 42, pp. 2700–2705, 2021.

[5] L. A. Mohammed, O. A. Nief, F. W. Askar, and A. H. Majeed, "Synthesis, characterization and antimicrobial activities of silver nanoparticles coated [1, 3] thiazin-4-one derivatives," *Journal of Physics: Conference Series*, vol. 1294, no. 5, p. 52028, 2019.

[6] L. A. Mohammed, "Effect of the addition of silver nanoparticles on the biological activity of thiocarbohydrazide derivatives," *Tikrit Journal of Pure Science*, vol. 21, no. 6, pp. 90–97, 2018.

[7] J. Zhang, D. Shu, T. Zhang et al., "Capacitive properties of PANI/MnO_2 synthesized via simultaneous-oxidation route," *Journal of Alloys and Compounds*, vol. 532, pp. 1–9, 2012.

[8] R. Zhang and H. Pang, "Application of graphene-metal/conductive polymer based composites in supercapacitors," *Journal of Energy Storage*, vol. 33, article 102037, 2021.

[9] C. I. Idumah, E. O. Ezeani, and I. C. Nwuzor, "A review: advancements in conductive polymers nanocomposites," *Polymer-Plastics Technology and Materials*, vol. 60, no. 7, pp. 756–783, 2021.

[10] M. M. Mahat, A. S. M. Sabere, J. Azizi, and N. A. N. Amdan, "Potential applications of conducting polymers to reduce secondary bacterial infections among COVID-19 patients: a review," *Emergent Materials*, vol. 4, no. 1, pp. 279–292, 2021.

[11] Z. Zhang, M. Rouabhia, and S. E. Moulton, *Conductive Polymers: Electrical Interactions in Cell Biology and Medicine*, CRC Press, 2018.

[12] D. Feldman, "Polymers and polymer nanocomposites for cancer therapy," *Applied Sciences*, vol. 9, no. 18, p. 3899, 2019.

[13] S. P. Singh, S. K. Srivastav, K. Kumar, and A. K. Agarwal, "Metal nanocomposites for energy and environmental applications," in *Metal Nanocomposites for Energy and Environmental Applications*, pp. 3–6, Springer, 2022.

[14] M. A. Farhan, A. H. Majeed, N. A. Imran, W. S. Al-Zuhairi, and L. A. Mohammed, "A review of overcome the side effect of digestion process on the drugs," *Earthline Journal of Chemical Sciiences*, vol. 5, no. 2, pp. 363–375, 2021.

[15] M. A. Alheety, A. H. Majeed, A. H. Ali, L. A. Mohammed, A. Destagul, and P. K. Singh, "Synthesis and characterization of eggshell membrane polymer-TiO_2 nanocomposite for newly synthesized ionic liquid release," *Journal of the Iranian Chemical Society*, vol. 19, no. 9, pp. 4005–4015, 2022.

[16] A. N. Abd, A. H. Al-Agha, and M. A. Alheety, "Addition of some primary and secondary amines to graphene oxide, and studying their effect on increasing its electrical properties," *Baghdad Science Journal*, vol. 13, no. 1, pp. 97–112, 2016.

[17] M. G. Sumdani, M. R. Islam, A. N. A. Yahaya, and S. I. Safie, "Recent advancements in synthesis, properties, and applications of conductive polymers for electrochemical energy storage devices: a review," *Polymer Engineering and Science*, vol. 62, no. 2, pp. 269–303, 2022.

[18] X. Li, X. Chen, Z. Jin, P. Li, and D. Xiao, "Recent progress in conductive polymers for advanced fiber-shaped electrochemical energy storage devices," *Materials Chemistry Frontiers*, vol. 5, no. 3, pp. 1140–1163, 2021.

[19] A. H. Majeed, D. H. Hussain, E. T. B. Al-Tikrity, and M. A. Alheety, "Poly(*o*-phenylenediamine-GO-TiO_2) nanocomposite: modulation, characterization and thermodynamic calculations on its H_2 storage capacity," *Chemical Data Collections*, vol. 28, article 100450, 2020.

[20] A. H. Majeed, E. T. B. Al-Tikrity, and D. H. Hussain, "Dielectric properties of synthesized ternary hybrid nanocomposite embedded in poly (vinyl alcohol) matrix films," *Polymers and Polymer Composites*, p. 967391120951406, 2020.

[21] M. Ates, T. Karazehir, and A. Sezai Sarac, "Conducting polymers and their applications," *Current Physical Chemistry*, vol. 2, no. 3, pp. 224–240, 2012.

[22] J. Luo, S. Jiang, R. Liu, Y. Zhang, and X. Liu, "Synthesis of water dispersible polyaniline/poly(styrenesulfonic acid) modified graphene composite and its electrochemical properties," *Electrochimica Acta*, vol. 96, pp. 103–109, 2013.

[23] Y. Mei, Z. Shen, S. Kundu et al., "Perovskite solar cells with polyaniline hole transport layers surpassing a 20% power conversion efficiency," *Chemistry of Materials*, vol. 33, no. 12, pp. 4679–4687, 2021.

[24] M. A. Deyab, G. Mele, E. Bloise, and Q. Mohsen, "Novel nanocomposites of Ni-Pc/polyaniline for the corrosion safety of the aluminum current collector in the Li-ion battery electrolyte," *Scientific Reports*, vol. 11, no. 1, pp. 1–8, 2021.

[25] A. K. Ghasemi, M. Ghorbani, M. S. Lashkenari, and N. Nasiri, "Controllable synthesis of zinc ferrite nanostructure with tunable morphology on polyaniline nanocomposite for supercapacitor application," *Journal of Energy Storage*, vol. 51, article 104579, 2022.

[26] A. A. Yaqoob, A. Serrà, S. A. Bhawani et al., "Utilizing biomass-based graphene oxide–polyaniline–ag electrodes in microbial fuel cells to boost energy generation and heavy metal removal," *Polymers*, vol. 14, no. 4, p. 845, 2022.

[27] J. Upadhyay, T. M. Das, and R. Borah, "Electrochemical performance study of polyaniline and polypyrrole based flexible electrodes," *International Journal of Polymer Analysis and Characterization*, vol. 26, no. 4, pp. 354–363, 2021.

[28] C. H. Abdul Kadar, M. Faisal, N. Maruthi, N. Raghavendra, B. P. Prasanna, and S. R. Manohara, "Corrosion-resistant polyaniline-coated zinc tungstate nanocomposites with enhanced electric properties for electromagnetic shielding applications," *Macromolecular Research*, pp. 1–12, 2022.

[29] A. Samadi, M. Xie, J. Li, H. Shon, C. Zheng, and S. Zhao, "Polyaniline-based adsorbents for aqueous pollutants removal: a review," *Chemical Engineering Journal*, vol. 418, article 129425, 2021.

[30] X. Zhang, Y. Wang, D. Fu, G. Wang, H. Wei, and N. Ma, "Photo-thermal converting polyaniline/ionic liquid inks for screen printing highly-sensitive flexible uncontacted thermal sensors," *European Polymer Journal*, vol. 147, article 110305, 2021.

[31] G. P. Oliveira, B. H. Barboza, and A. Batagin-Neto, "Polyaniline-based gas sensors: DFT study on the effect of side groups," *Computational & Theoretical Chemistry*, vol. 1207, article 113526, 2022.

[32] A. G. MacDiarmid, "Polyaniline and polypyrrole: where are we headed?," *Synthetic Metals*, vol. 84, no. 1–3, pp. 27–34, 1997.

[33] S. Kalluri, A. M. Asha, S. Parvathy et al., "Electrospun nanofibers of polyaniline-carbon black composite for conductive electrode applications," *Trends in Polyaniline Research*, pp. 181–202, 2013.

[34] G. Venugopal, X. Quan, G. E. Johnson, F. M. Houlihan, E. Chin, and O. Nalamasu, "Photoinduced doping and photolithography of methyl-substituted polyaniline," *Chemistry of Materials*, vol. 7, no. 2, pp. 271–276, 1995.

[35] A. Malinauskas, "Self-doped polyanilines," *Journal of Power Sources*, vol. 126, no. 1–2, pp. 214–220, 2004.

[36] S. Bhadra, N. K. Singha, and D. Khastgir, "Dual functionality of PTSA as electrolyte and dopant in the electrochemical synthesis of polyaniline, and its effect on electrical properties," *Polymer International*, vol. 56, no. 7, pp. 919–927, 2007.

[37] V. Babel and B. L. Hiran, "A review on polyaniline composites: synthesis, characterization, and applications," *Polymer Composites*, vol. 42, no. 7, pp. 3142–3157, 2021.

[38] S. Virji, J. Huang, R. B. Kaner, and B. H. Weiller, "Polyaniline nanofiber gas sensors: examination of response mechanisms," *Nano Letters*, vol. 4, no. 3, pp. 491–496, 2004.

[39] G. G. Wallace, P. R. Teasdale, G. M. Spinks, and L. A. P. Kane-Maguire, *Conductive Electroactive Polymers: Intelligent Polymer Systems*, CRC press, 2008.

[40] M. Aldissi, *Intrinsically Conducting Polymers: An Emerging Technology*, vol. 246, Springer Science + Business Media, 2013.

[41] M. Beygisangchin, S. Abdul Rashid, S. Shafie, A. R. Sadrolhosseini, and H. N. Lim, "Preparations, properties, and applications of polyaniline and polyaniline thin films—a review," *Polymers*, vol. 13, no. 12, p. 2003, 2021.

[42] A. Korent, K. Ž. Soderžnik, S. Šturm, and K. Ž. Rožman, "A correlative study of polyaniline electropolymerization and its electrochromic behavior," *Journal of the Electrochemical Society*, vol. 167, no. 10, article 106504, 2020.

[43] N. Gospodinova and L. Terlemezyan, "Conducting polymers prepared by oxidative polymerization: polyaniline," *Progress in Polymer Science*, vol. 23, no. 8, pp. 1443–1484, 1998.

[44] N. K. Jangid, S. Jadoun, and N. Kaur, "A review on high-throughput synthesis, deposition of thin films and properties of polyaniline," *European Polymer Journal*, vol. 125, article 109485, 2020.

[45] Y. Cao, A. Andreatta, A. J. Heeger, and P. Smith, "Influence of chemical polymerization conditions on the properties of polyaniline," *Polymer*, vol. 30, no. 12, pp. 2305–2311, 1989.

[46] E. M. Genies, A. Boyle, M. Lapkowski, and C. Tsintavis, "Polyaniline: a historical survey," *Synthetic Metals*, vol. 36, no. 2, pp. 139–182, 1990.

[47] K. Tzou and R. V. Gregory, "Kinetic study of the chemical polymerization of aniline in aqueous solutions," *Synthetic Metals*, vol. 47, no. 3, pp. 267–277, 1992.

[48] D. E. Stilwell and S. Park, "Electrochemistry of conductive polymers: II. Electrochemical studies on growth properties of polyaniline," *Journal of the Electrochemical Society*, vol. 135, no. 9, pp. 2254–2262, 1988.

[49] S. Tan, J. Zhai, B. Xue et al., "Property influence of polyanilines on photovoltaic behaviors of dye-sensitized solar cells," *Langmuir*, vol. 20, no. 7, pp. 2934–2937, 2004.

[50] B. Guo, Y. Zhao, W. Wu et al., "Research on the preparation technology of polyaniline nanofiber based on high gravity chemical oxidative polymerization," *Chemical Engineering and Processing Process Intensification*, vol. 70, pp. 1–8, 2013.

[51] B. Das, S. Kar, S. Chakraborty, D. Chakraborty, and S. Gangopadhyay, "Synthesis and characterization of polyacrylamide–polyaniline conductive blends," *Journal of Applied Polymer Science*, vol. 69, no. 5, pp. 841–844, 1998.

[52] J.-Y. Kim, J.-H. Lee, and S.-J. Kwon, "The manufacture and properties of polyaniline nano-films prepared through vapor-phase polymerization," *Synthetic Metals*, vol. 157, no. 8–9, pp. 336–342, 2007.

[53] P. Zarrintaj and M. R. Saeb, "Synthetic route of polyaniline (IV): irradiation path," in *Fundamentals and Emerging Applications of Polyaniline*, pp. 91–103, Elsevier, 2019.

[54] K. Teshima, S. Uemura, N. Kobayashi, and R. Hirohashi, "Effect of pH on photopolymerization reaction of aniline derivatives with the tris(2,2'-bipyridyl)ruthenium complex and the methylviologen system," *Macromolecules*, vol. 31, no. 20, pp. 6783–6788, 1998.

[55] Y. Kim, S. Fukai, and N. Kobayashi, "Photopolymerization of aniline derivatives in solid state and its application," *Synthetic Metals*, vol. 119, no. 1–3, pp. 337–338, 2001.

[56] P. Hamdi-Mohammadabad, T. Tohidi, R. Talebzadeh, R. Mohammad-Rezaei, and S. Rahmatallahpur, "Preparation and characterization of gamma irradiated ZnO/PANI hybrid films," *Journal of Radioanalytical and Nuclear Chemistry*, vol. 330, no. 3, pp. 785–796, 2021.

[57] M. R. Gizdavic-Nikolaidis, D. R. Stanisavljev, A. J. Easteal, and Z. D. Zujovic, "A rapid and facile synthesis of nanofibrillar polyaniline using microwave radiation," *Macromolecular Rapid Communications*, vol. 31, no. 7, pp. 657–661, 2010.

[58] S. V. J. Sury, A. Ulianas, and S. Aini, "Synthesis of conducting polyaniline with photopolymerization method and characterization," *Journal of Physics: Conference Series*, vol. 1788, no. 1, p. 12004, 2021.

[59] J. F. Felix, R. A. Barros, W. M. De Azevedo, and E. F. da Silva Jr, "X-ray irradiation: a non-conventional route for the synthesis of conducting polymers," *Synthetic Metals*, vol. 161, no. 1–2, pp. 173–176, 2011.

[60] R. Sfez, E. Natan, Y. Bardavid et al., "Enzyme mediated encapsulation of gold nanoparticles by polyaniline nanoshell," *Journal of Self-Assembly and Molecular Electronics*, vol. 3, no. 1, pp. 1–16, 2015.

[61] A. Jabłońska, M. Gniadek, and B. Pałys, "Enhancement of direct electrocatalytic activity of horseradish peroxidase on polyaniline nanotubes," *Journal of Physical Chemistry C*, vol. 119, no. 22, pp. 12514–12522, 2015.

[62] L. A. Samuelson, A. Anagnostopoulos, K. S. Alva, J. Kumar, and S. K. Tripathy, "Biologically derived conducting and water soluble polyaniline," *Macromolecules*, vol. 31, no. 13, pp. 4376–4378, 1998.

[63] W. Liu, J. Kumar, S. Tripathy, K. J. Senecal, and L. Samuelson, "Enzymatically synthesized conducting polyaniline," *Journal of the American Chemical Society*, vol. 121, no. 1, pp. 71–78, 1999.

[64] X. Wang, H. Schreuder-Gibson, M. Downey, S. Tripathy, and L. Samuelson, "Conductive fibers from enzymatically synthesized polyaniline," *Synthetic Metals*, vol. 107, no. 2, pp. 117–121, 1999.

[65] W. Liu, J. Kumar, S. Tripathy, and L. A. Samuelson, "Enzymatic synthesis of conducting polyaniline in micelle solutions," *Langmuir*, vol. 18, no. 25, pp. 9696–9704, 2002.

[66] R. Nagarajan, S. Tripathy, J. Kumar, F. F. Bruno, and L. Samuelson, "An enzymatically synthesized conducting molecular complex of polyaniline and poly (vinylphosphonic acid)," *Macromolecules*, vol. 33, no. 26, pp. 9542–9547, 2000.

[67] R. Nagarajan, W. Liu, J. Kumar, S. K. Tripathy, F. F. Bruno, and L. A. Samuelson, "Manipulating DNA conformation using intertwined conducting polymer chains," *Macromolecules*, vol. 34, no. 12, pp. 3921–3927, 2001.

[68] L. W. Shacklette and C. C. Han, "Solubility and dispersion characteristics of polyaniline," *MRS Online Proceedings Library*, vol. 328, 1993.

[69] H. Hussin, S. N. Gan, S. Mohamad, and S. W. Phang, "Synthesis of water-soluble polyaniline by using different types of cellulose derivatives," *Polymers and Polymer Composites*, vol. 25, no. 7, pp. 515–520, 2017.

[70] W. S. Huang and A. G. MacDiarmid, "Optical properties of polyaniline," *Polymer*, vol. 34, no. 9, pp. 1833–1845, 1993.

[71] C. Barbero and R. Kötz, "Nanoscale dimensional changes and optical properties of polyaniline measured by in situ spectroscopic ellipsometry," *Journal of the Electrochemical Society*, vol. 141, no. 4, pp. 859–865, 1994.

[72] S. Stafström, J. L. Brédas, A. J. Epstein et al., "Polaron lattice in highly conducting polyaniline: theoretical and optical studies," *Physical Review Letters*, vol. 59, no. 13, pp. 1464–1467, 1987.

[73] L. Zhuang, Q. Zhou, and J. Lu, "Simultaneous electrochemical-ESR-conductivity measurements of polyaniline," *Journal of Electroanalytical Chemistry*, vol. 493, no. 1–2, pp. 135–140, 2000.

[74] Y. Xia, J. M. Wiesinger, A. G. MacDiarmid, and A. J. Epstein, "Camphorsulfonic acid fully doped polyaniline emeraldine salt: conformations in different solvents studied by an ultraviolet/visible/near-infrared spectroscopic method," *Chemistry of Materials*, vol. 7, no. 3, pp. 443–445, 1995.

[75] Y. Wei, G.-W. Jang, K. F. Hsueh, E. M. Scherr, A. G. MacDiarmid, and A. J. Epstein, "Thermal transitions and mechanical properties of films of chemically prepared polyaniline," *Polymer*, vol. 33, no. 2, pp. 314–322, 1992.

[76] W.-S. Huang, B. D. Humphrey, and A. G. MacDiarmid, "Polyaniline, a novel conducting polymer. Morphology and chemistry of its oxidation and reduction in aqueous electrolytes," *Jounal of the Chemical Society, Faraday Transactions 1: Physical Chemistry Condensed Phases*, vol. 82, no. 8, pp. 2385–2400, 1986.

[77] M. Q. Mezan, S. O. Mezan, K. Mohammed, and A. H. Jabbar, "A review on synthesis of conducting with polyaniline rice

husk ash silica nanocomposites and application," *International Journal of Psychosocial Rehabilitation*, vol. 24, no. 3, 2020.

[78] N. Khalid, J. A. Razak, H. Hasib et al., "A short review on polyaniline (PANI) based nanocomposites for various applications: enhancing the electrical conductivity," *IOP Conference Series: Materials Science and Engineering*, vol. 957, no. 1, p. 12028, 2020.

[79] K. A. Ibrahim, "Synthesis and characterization of polyaniline and poly(aniline-co-o-nitroaniline) using vibrational spectroscopy," *Arabian Journal of Chemistry*, vol. 10, pp. S2668–S2674, 2017.

[80] H. F. Alesary, H. K. Ismail, A. F. Khudhair, and M. Q. Mohammed, "Effects of dopant ions on the properties of polyaniline conducting polymer," *Oriental Journal of Chemistry*, vol. 34, no. 5, pp. 2525–2533, 2018.

[81] J. Wang, Z. Wu, K. Hu, X. Chen, and H. Yin, "High conductivity graphene-like MoS_2/polyaniline nanocomposites and its application in supercapacitor," *Journal of Alloys and Compounds*, vol. 619, pp. 38–43, 2015.

[82] A. Sayah, F. Habelhames, A. Bahloul et al., "Electrochemical synthesis of polyaniline-exfoliated graphene composite films and their capacitance properties," *Journal of Electroanalytical Chemistry*, vol. 818, pp. 26–34, 2018.

[83] A. H. Al-Agha and I. A. Latif, "Silver nanoparticles anchored 5-methoxy benzimidazol thiomethanol (MBITM): modulate, characterization and comparative studies on MBITM and ag-MBITM antibacterial activities," *Diyala Journal of Pure Science*, vol. 12, 3-part 1, 2016.

[84] D. Majumdar, "Polyaniline nanocomposites: innovative materials for supercapacitor applications–PANI nanocomposites for supercapacitor applications," in *Polymer Nanocomposites for Advanced Engineering and Military Applications*, pp. 220–253, IGI Global, 2019.

[85] S. B. Kondawar, M. D. Deshpande, and S. P. Agrawal, "Transport properties of conductive polyaniline nanocomposites based on carbon nanotubes," *International Journal of Composite Materials*, vol. 2, no. 3, pp. 32–36, 2012.

[86] C. Basavaraja, G. H. Jung, and D. S. Huh, "Solubility and electrochemical properties of chemically modified polyaniline-gold/camphor sulfonic acid composites," *Polymer Composites*, vol. 36, no. 2, pp. 245–252, 2015.

[87] M. Diantoro and A. A. Mustikasari, "The influence of SnO_2 nanoparticles on electrical conductivity, and transmittance of PANI-SnO_2 films," *IOP Conference Series: Materials Science and Engineering*, vol. 367, no. 1, p. 12034, 2018.

[88] M. R. Safenaz and M. Sheikha, "Synthesis and electrical properties of polyaniline composite with silver nanoparticles," *Advances in Materials Physics and Chemistry*, p. 2012, 2012.

[89] V. Kumar, T. Yokozeki, T. Goto, and T. Takahashi, "Mechanical and electrical properties of PANI-based conductive thermosetting composites," *Journal of Reinforced Plastics and Composites*, vol. 34, no. 16, pp. 1298–1305, 2015.

[90] A. J. Heeger, "Polyaniline with surfactant counterions: conducting polymer materials which are processible in the conducting form," *Synthetic Metals*, vol. 57, no. 1, pp. 3471–3482, 1993.

[91] Y. Cao, P. Smith, and A. J. Heeger, "Counter-ion induced processibility of conducting polyaniline," *Synthetic Metals*, vol. 57, no. 1, pp. 3514–3519, 1993.

[92] A. K. Bajpai, J. Bajpai, and S. N. Soni, "Designing polyaniline (PANI) and polyvinyl alcohol (PVA) based electrically conductive nanocomposites: preparation, characterization and blood compatible study," *Journal of Macromolecular Science, Part A Pure and Applied Chemistry*, vol. 46, no. 8, pp. 774–782, 2009.

[93] N. Y. Yuan, F. F. Ma, Y. Fan, Y. B. Liu, and J. N. Ding, "High conductive ethylene vinyl acetate composites filled with reduced graphene oxide and polyaniline," *Composites. Part A, Applied Science and Manufacturing*, vol. 43, no. 12, pp. 2183–2188, 2012.

[94] T.-C. Mo, H.-W. Wang, S.-Y. Chen, and Y.-C. Yeh, "Synthesis and dielectric properties of polyaniline/titanium dioxide nanocomposites," *Ceramics International*, vol. 34, no. 7, pp. 1767–1771, 2008.

[95] S. K. Shweta, C. Gumma, and A. G. Bidve, "In-situ chemical synthesis and electrical properties of PANI/TiO_2 composites, international research journal of engineering and technology," *International Research Journal of Engineering and Technology*, vol. 8, no. 4, pp. 1598–1603, 2021.

[96] M. Vellakkat, A. Kamath, S. Raghu, S. Chapi, and D. Hundekal, "Dielectric constant and transport mechanism of percolated polyaniline nanoclay composites," *Industrial and Engineering Chemistry Research*, vol. 53, no. 43, pp. 16873–16882, 2014.

[97] A. M. Meftah, E. Gharibshahi, N. Soltani, W. Yunus, and E. Saion, "Structural, optical and electrical properties of PVA/PANI/nickel nanocomposites synthesized by gamma radiolytic method," *Polymers*, vol. 6, no. 9, pp. 2435–2450, 2014.

[98] A. A. Ganash, F. M. Al-Nowaiser, S. A. Al-Thabaiti, and A. A. Hermas, "Comparison study for passivation of stainless steel by coating with polyaniline from two different acids," *Progress in Organic Coatings*, vol. 72, no. 3, pp. 480–485, 2011.

[99] K. Kamaraj, V. Karpakam, S. Sathiyanarayanan, S. S. Azim, and G. Venkatachari, "Synthesis of tungstate doped polyaniline and its usefulness in corrosion protective coatings," *Electrochimica Acta*, vol. 56, no. 25, pp. 9262–9268, 2011.

[100] S. Chaudhari and P. P. Patil, "Inhibition of nickel coated mild steel corrosion by electrosynthesized polyaniline coatings," *Electrochimica Acta*, vol. 56, no. 8, pp. 3049–3059, 2011.

[101] A. Mirmohseni and A. Oladegaragoze, "Anti-corrosive properties of polyaniline coating on iron," *Synthetic Metals*, vol. 114, no. 2, pp. 105–108, 2000.

[102] F. Yakuphanoglu and B. F. Şenkal, "Electronic and thermoelectric properties of polyaniline organic semiconductor and electrical characterization of Al/PANI MIS diode," *Journal of Physical Chemistry C*, vol. 111, no. 4, pp. 1840–1846, 2007.

[103] F. Yakuphanoglu and B. F. Şenkal, "Electrical transport properties of an organic semiconductor on polyaniline doped by boric acid," *Polymers for Advanced Technologies*, vol. 19, no. 12, pp. 1876–1881, 2008.

[104] G. A. Snook, P. Kao, and A. S. Best, "Conducting-polymer-based supercapacitor devices and electrodes," *Journal of Power Sources*, vol. 196, no. 1, pp. 1–12, 2011.

[105] R. Pal, S. L. Goyal, I. Rawal, A. K. Gupta, and Ruchi, "Efficient energy storage performance of electrochemical supercapacitors based on polyaniline/graphene nanocomposite electrodes," *Journal of Physics and Chemistry of Solids*, vol. 154, article 110057, 2021.

[106] C.-Y. Kung, T.-L. Wang, H.-Y. Lin, and C.-H. Yang, "A high-performance covalently bonded self-doped polyaniline-graphene assembly film with superior stability for supercapacitors," *Journal of Power Sources*, vol. 490, article 229538, 2021.

[107] A. Xu, W. Li, Y. Yu, Y. Zhang, Z. Liu, and Y. Qin, "Rational design of active layer configuration with parallel graphene/polyaniline composite films for high-performance supercapacitor electrode," *Electrochimica Acta*, vol. 398, article 139330, 2021.

[108] A. S. Wasfi, N. I. Ibrahim, and H. O. Ismael, "Polyaniline/carbon nanotube composite supercapacitor electrodes synthesized by a microwave-plasma polymerization," *AIP Conference Proceedings*, vol. 2372, no. 1, article 130017, 2021.

[109] J. Dai, Y. Lv, J. Zhang et al., "Effect of morphology and phase engineering of MoS_2 on electrochemical properties of carbon nanotube/$_2$ composites," *Journal of Colloid and Interface Science*, vol. 590, pp. 591–600, 2021.

[110] M. Jasna, M. Manoj, A. Abhilash, P. S. Midhun, S. Jayalekshmi, and M. K. Jayaraj, "Polyaniline wrapped carbon nanotube/exfoliated MoS_2 nanosheet composite as a promising electrode for high power supercapacitors," *Carbon Trends*, vol. 7, article 100154, 2022.

[111] H. S. Roy, M. M. Islam, M. Y. A. Mollah, and M. A. B. H. Susan, "Polyaniline-MnO_2 composites prepared in-situ during oxidative polymerization of aniline for supercapacitor applications," *Materials Today: Procedings*, vol. 29, pp. 1013–1019, 2020.

[112] H. Heydari, M. Abdouss, S. Mazinani, A. M. Bazargan, and F. Fatemi, "Electrochemical study of ternary polyaniline/MoS_2–MnO_2 for supercapacitor applications," *Journal of Energy Storage*, vol. 40, article 102738, 2021.

[113] M. B. Poudel, M. Shin, and H. J. Kim, "Polyaniline-silver-manganese dioxide nanorod ternary composite for asymmetric supercapacitor with remarkable electrochemical performance," *International Journal of Hydrogen Energy*, vol. 46, no. 1, pp. 474–485, 2021.

[114] M. Wan, W. Zhou, Y. Li, and J. Liu, "Protonic doping in free-standing film of polyaniline," *Solid State Communications*, vol. 81, no. 4, pp. 313–316, 1992.

[115] Y. Long, Z. Chen, J. Shen et al., "Magnetic properties of conducting polymer nanostructures," *The Journal of Physical Chemistry. B*, vol. 110, no. 46, pp. 23228–23233, 2006.

[116] X. Lu, H. Mao, D. Chao, W. Zhang, and Y. Wei, "Ultrasonic synthesis of polyaniline nanotubes containing Fe_3O_4 nanoparticles," *Journal of Solid State Chemistry*, vol. 179, no. 8, pp. 2609–2615, 2006.

[117] B. Dittrich, K.-A. Wartig, R. Mülhaupt, and B. Schartel, "Flame-retardancy properties of intumescent ammonium poly(phosphate) and mineral filler magnesium hydroxide in combination with graphene," *Polymers*, vol. 6, no. 11, pp. 2875–2895, 2014.

[118] R. Gangopadhyay and A. De, "Conducting polymer nanocomposites: a brief overview," *Chemistry of Materials*, vol. 12, no. 3, pp. 608–622, 2000.

[119] H. Bai, C. Li, and G. Shi, "Functional composite materials based on chemically converted graphene," *Advanced Materials*, vol. 23, no. 9, pp. 1089–1115, 2011.

[120] A. A. B. Omran, A. A. B. A. Mohammed, S. M. Sapuan et al., "Micro- and nanocellulose in polymer composite materials: a review," *Polymers*, vol. 13, no. 2, p. 231, 2021.

[121] K. Namsheer and C. S. Rout, "Conducting polymers: a comprehensive review on recent advances in synthesis, properties and applications," *RSC Advances*, vol. 11, no. 10, pp. 5659–5697, 2021.

[122] T. Sen, S. Mishra, and N. G. Shimpi, "Synthesis and sensing applications of polyaniline nanocomposites: a review," *RSC Advances*, vol. 6, no. 48, pp. 42196–42222, 2016.

[123] B. Zhang, B. Zhao, S. Huang, R. Zhang, P. Xu, and H.-L. Wang, "One-pot interfacial synthesis of Au nanoparticles and Au–polyaniline nanocomposites for catalytic applications," *CrystEngComm*, vol. 14, no. 5, pp. 1542–1544, 2012.

[124] N. V. Blinova, J. Stejskal, M. Trchova, I. Sapurina, and G. Ćirić-Marjanović, "The oxidation of aniline with silver nitrate to polyaniline-silver composites," *Polymer*, vol. 50, no. 1, pp. 50–56, 2009.

[125] P. K. Khanna, N. Singh, S. Charan, and A. K. Viswanath, "Synthesis of Ag/polyaniline nanocomposite via an in situ photo-redox mechanism," *Materials Chemistry and Physics*, vol. 92, no. 1, pp. 214–219, 2005.

[126] S. S. Barkade, J. B. Naik, and S. H. Sonawane, "Ultrasound assisted miniemulsion synthesis of polyaniline/Ag nanocomposite and its application for ethanol vapor sensing," *Colloids and Surfaces A: Physicochemical Engineering Aspects*, vol. 378, no. 1–3, pp. 94–98, 2011.

[127] B. Gu, S. He, W. Zhou et al., "Polyaniline-supported iron catalyst for selective synthesis of lower olefins from syngas," *Journal of Energy Chemistry*, vol. 26, no. 4, pp. 608–615, 2017.

[128] A. Houdayer, R. Schneider, D. Billaud, J. Ghanbaja, and J. Lambert, "New polyaniline/Ni(0) nanocomposites: synthesis, characterization and evaluation of their catalytic activity in Heck couplings," *Synthetic Metals*, vol. 151, no. 2, pp. 165–174, 2005.

[129] Y. Zhang, J. Yin, K. Wang, P. Chen, and L. Ji, "Electrocatalysis and detection of nitrite on a polyaniline–Cu nanocomposite-modified glassy carbon electrode," *Journal of Applied Polymer Science*, vol. 128, no. 5, pp. 2971–2976, 2013.

[130] L. Kong, X. Lu, E. Jin, S. Jiang, C. Wang, and W. Zhang, "Templated synthesis of polyaniline nanotubes with Pd nanoparticles attached onto their inner walls and its catalytic activity on the reduction of p-nitroanilinum," *Composites Science and Technology*, vol. 69, no. 5, pp. 561–566, 2009.

[131] W. Cho, S.-J. Park, and S. Kim, "Effect of monomer concentration on interfacial synthesis of platinum loaded polyaniline nanocomplex using poly(styrene sulfonic acid)," *Synthetic Metals*, vol. 161, no. 21–22, pp. 2446–2450, 2011.

[132] A. S. Najibzad, R. Amini, M. Rostami, P. Kardar, and M. Fedel, "Active corrosion performance of magnesium by silane coatings reinforced with polyaniline/praseodymium," *Progress in Organic Coatings*, vol. 140, article 105504, 2020.

[133] M. Alam, A. M. Siddiqui, and M. Husain, "Synthesis, characterization and properties of Se nanowires intercalated polyaniline/Se nanocomposites," *Express Polymer Letters*, vol. 7, no. 9, 2013.

[134] G. Sharma, M. Naushad, A. Kumar, S. Devi, and M. R. Khan, "Lanthanum/cadmium/polyaniline bimetallic nanocomposite for the photodegradation of organic pollutant," *Iranian Polymer Journal*, vol. 24, no. 12, pp. 1003–1013, 2015.

[135] S. Sharma, S. Singh, and N. Khare, "Synthesis of polyaniline/CdS (nanoflowers and nanorods) nanocomposites: a comparative study towards enhanced photocatalytic activity for

degradation of organic dye," *Colloid & Polymer Science*, vol. 294, no. 5, pp. 917–926, 2016.

[136] J. B. Bhaiswar, M. Y. Salunkhe, S. P. Dongre, and B. T. Kumbhare, "Comparative study on thermal stability and optical properties of PANI/CdS and PANI/PbS nanocomposite," *IOSR Journal of Applied Physics*, vol. 80, pp. 79–82, 2014.

[137] P. Boomi and H. G. Prabu, "Synthesis, characterization and antibacterial analysis of polyaniline/Au–Pd nanocomposite," *Colloids and Surfaces A: Physicochemical Engineering Aspects*, vol. 429, pp. 51–59, 2013.

[138] C. Yang, W. Dong, G. Cui et al., "Enhanced photocatalytic activity of PANI/TiO_2 due to their photosensitization-synergetic effect," *Electrochimica Acta*, vol. 247, pp. 486–495, 2017.

[139] J. Husain, N. Reddy, A. Begum et al., "Conductivity and LPG sensing behavior of PANI/MgO nano composites thin films," *Materials Today: Procedings*, vol. 46, pp. 410–412, 2021.

[140] V. Gilja, I. Vrban, V. Mandić, M. Žic, and Z. Hrnjak-Murgić, "Preparation of a PANI/ZnO composite for efficient photocatalytic degradation of acid blue," *Polymers*, vol. 10, no. 9, p. 940, 2018.

[141] A. Auliya, R. Deswara, M. Paristiowati, and S. Budi, "Electrodeposition of PANI-NiO as electrode for deionization K^+ and Cl," *Chemistry of Materials*, vol. 1, no. 1, pp. 1–6, 2022.

[142] V. S. Sumi, S. R. Arunima, M. J. Deepa et al., "PANI-Fe_2O_3 composite for enhancement of active life of alkyd resin coating for corrosion protection of steel," *Materials Chemistry and Physics*, vol. 247, article 122881, 2020.

[143] T. Sen, N. G. Shimpi, S. Mishra, and R. Sharma, "Polyaniline/γ-Fe_2O_3 nanocomposite for room temperature LPG sensing," *Sensors and Actuators B: Chemical*, vol. 190, pp. 120–126, 2014.

[144] Z. Yang, L. Tang, J. Ye, D. Shi, S. Liu, and M. Chen, "Hierarchical nanostructured α-Fe_2O_3/polyaniline anodes for high performance supercapacitors," *Electrochimica Acta*, vol. 269, pp. 21–29, 2018.

[145] S. M. Ambalagi, M. Devendrappa, S. Nagaraja, and B. Sannakki, "Dielectric properties of PANI/CuO nanocomposites," *IOP Conference Series: Materials Science and Engineering*, vol. 310, no. 1, p. 12081, 2018.

[146] Y. Fan, H. Chen, Y. Li, D. Cui, Z. Fan, and C. Xue, "PANI-Co_3O_4 with excellent specific capacitance as an electrode for supercapacitors," *Ceramics International*, vol. 47, no. 6, pp. 8433–8440, 2021.

[147] C. Sridhar, N. Gunvanthrao Yernale, and M. V. N. Prasad, "Synthesis, spectral characterization, and antibacterial and antifungal studies of PANI/V_2O_5 nanocomposites," *International Journal of Chemical Engineering*, vol. 2016, p. 6, 2016.

[148] P. R. Deshmukh, R. N. Bulakhe, S. N. Pusawale, S. D. Sartale, and C. D. Lokhande, "Polyaniline–RuO composite for high performance supercapacitors: chemical synthesis and properties," *RSC Advances*, vol. 5, no. 36, pp. 28687–28695, 2015.

[149] Q. Feng, H. Zhang, Y. Shi, X. Yu, and G. Lan, "Preparation and gas sensing properties of PANI/SnO_2 hybrid material," *Polymers*, vol. 13, no. 9, p. 1360, 2021.

[150] S. R. Jamnani, H. M. Moghaddam, S. G. Leonardi, and G. Neri, "PANI/Sm_2O_3 nanocomposite sensor for fast hydrogen detection at room temperature," *Synthetic Metals*, vol. 268, article 116493, 2020.

[151] M. Nallappan and M. Gopalan, "Fabrication of CeO_2/PANI composites for high energy density supercapacitors," *Materials Research Bulletin*, vol. 106, pp. 357–364, 2018.

[152] J. Zhu, S. Wei, L. Zhang et al., "Electrical and dielectric properties of polyaniline–Al_2O_3 nanocomposites derived from various Al_2O_3 nanostructures," *Journal of Materials Chemistry*, vol. 21, no. 11, pp. 3952–3959, 2011.

[153] R. Wu, H. Yuan, C. Liu, J.-L. Lan, X. Yang, and Y.-H. Lin, "Flexible PANI/SWCNT thermoelectric films with ultrahigh electrical conductivity," *RSC Advances*, vol. 8, no. 46, pp. 26011–26019, 2018.

[154] M. H. Suhail, O. G. Abdullah, and G. A. Kadhim, "Hydrogen sulfide sensors based on PANI/f-SWCNT polymer nanocomposite thin films prepared by electrochemical polymerization," *Journal of Science: Advanced Materials and Devices*, vol. 4, no. 1, pp. 143–149, 2019.

[155] D. Maity, M. Manoharan, and R. T. Rajendra Kumar, "Development of the PANI/MWCNT nanocomposite-based fluorescent sensor for selective detection of aqueous ammonia," *ACS Omega*, vol. 5, no. 15, pp. 8414–8422, 2020.

[156] G. Otrokhov, D. Pankratov, G. Shumakovich et al., "Enzymatic synthesis of polyaniline/multi-walled carbon nanotube composite with core shell structure and its electrochemical characterization for supercapacitor application," *Electrochimica Acta*, vol. 123, pp. 151–157, 2014.

[157] Y. Huang, J. Lu, S. Kang, D. Weng, L. Han, and Y. Wang, "Synthesis and application of MnO_2/PANI/MWCNT ternary nanocomposite as an electrode material for supercapacitors," *International Journal of Electrochemical Science*, vol. 14, pp. 9298–9310, 2019.

[158] L. Ouyang, Y. Wang, P. Zhang, X. Wang, and S. Yuan, "Heterostructured MWCNTs@PANI@TiO_2 nanocomposites for enhanced adsorption of As(III) from aqueous solution: adsorption and photocatalytic oxidation behaviors," *Industrial and Engineering Chemistry Research*, vol. 59, no. 25, pp. 11743–11756, 2020.

[159] I. Chakraborty, N. Chakrabarty, A. Senapati, and A. K. Chakraborty, "CuO@ NiO/polyaniline/MWCNT nanocomposite as high-performance electrode for supercapacitor," *Journal of Physical Chemistry C*, vol. 122, no. 48, pp. 27180–27190, 2018.

[160] D. Shao, G. Hou, J. Li, T. Wen, X. Ren, and X. Wang, "PANI/GO as a super adsorbent for the selective adsorption of uranium(VI)," *Chemical Engineering Journal*, vol. 255, pp. 604–612, 2014.

[161] B. Vellaichamy, P. Periakaruppan, and S. K. Ponnaiah, "A new in-situ synthesized ternary CuNPs-PANI-GO nano composite for selective detection of carcinogenic hydrazine," *Sensors and Actuators B: Chemical*, vol. 245, pp. 156–165, 2017.

[162] J. Zhang, H. Bi, G. He, Y. Zhou, and H. Chen, "Fabrication of Ag_3PO_4–PANI–GO composites with high visible light photocatalytic performance and stability," *Journal of Environmental Chemical Engineering*, vol. 2, no. 2, pp. 952–957, 2014.

[163] S. Palsaniya, H. B. Nemade, and A. K. Dasmahapatra, "Hierarchical PANI-RGO-ZnO ternary nanocomposites for symmetric tandem supercapacitor," *Journal of Physics and Chemistry of Solids*, vol. 154, article 110081, 2021.

[164] L. Wang, Q. Yao, H. Bi, F. Huang, Q. Wang, and L. Chen, "PANI/graphene nanocomposite films with high thermoelectric properties by enhanced molecular ordering," *Journal of Materials Chemistry A*, vol. 3, no. 13, pp. 7086–7092, 2015.

[165] S. Zhang, B.-Q. Li, and J.-B. Zheng, "An electrochemical sensor for the sensitive determination of nitrites based on Pt–PANI–graphene nanocomposites," *Analytical Methods*, vol. 7, no. 19, pp. 8366–8372, 2015.

[166] S. Xiong, F. Yang, H. Jiang, J. Ma, and X. Lu, "Covalently bonded polyaniline/fullerene hybrids with coral-like morphology for high-performance supercapacitor," *Electrochimica Acta*, vol. 85, pp. 235–242, 2012.

[167] J. Zhu, M. Chen, H. Qu et al., "Interfacial polymerized polyaniline/graphite oxide nanocomposites toward electrochemical energy storage," *Polymer*, vol. 53, no. 25, pp. 5953–5964, 2012.

[168] C. Meng, O. Z. Gall, and P. P. Irazoqui, "A flexible supercapacitive solid-state power supply for miniature implantable medical devices," *Biomedical Microdevices*, vol. 15, no. 6, pp. 973–983, 2013.

[169] J. H. Park, O. O. Park, K. H. Shin, C. S. Jin, and J. H. Kim, "An electrochemical capacitor based on a $Ni(OH)_2$/activated carbon composite electrode," *Electrochemical and Solid-State Letters*, vol. 5, no. 2, p. H7, 2002.

[170] A. S. Arico, P. Bruce, B. Scrosati, J.-M. Tarascon, and W. Van Schalkwijk, "Nanostructured materials for advanced energy conversion and storage devices," *Materials for Sustainable Energy*, pp. 148–159, 2010.

[171] G. Wang, L. Zhang, and J. Zhang, "A review of electrode materials for electrochemical supercapacitors," *Chemical Society Reviews*, vol. 41, no. 2, pp. 797–828, 2012.

[172] D. S. Dhawale, A. Vinu, and C. D. Lokhande, "Stable nanostructured polyaniline electrode for supercapacitor application," *Electrochimica Acta*, vol. 56, no. 25, pp. 9482–9487, 2011.

[173] V. Gupta and N. Miura, "Electrochemically deposited polyaniline nanowire's network: a high-performance electrode material for redox supercapacitor," *Electrochemical and Solid-State Letters*, vol. 8, no. 12, p. A630, 2005.

[174] H. Guan, L.-Z. Fan, H. Zhang, and X. Qu, "Polyaniline nanofibers obtained by interfacial polymerization for high-rate supercapacitors," *Electrochimica Acta*, vol. 56, no. 2, pp. 964–968, 2010.

[175] P. Bandyopadhyay, T. Kuila, J. Balamurugan, T. T. Nguyen, N. H. Kim, and J. H. Lee, "Facile synthesis of novel sulfonated polyaniline functionalized graphene using m-aminobenzene sulfonic acid for asymmetric supercapacitor application," *Chemical Engineering Journal*, vol. 308, pp. 1174–1184, 2017.

[176] J. Shen, C. Yang, X. Li, and G. Wang, "High-performance asymmetric supercapacitor based on nanoarchitectured polyaniline/graphene/carbon nanotube and activated graphene electrodes," *ACS Applied Materials & Interfaces*, vol. 5, no. 17, pp. 8467–8476, 2013.

[177] D. Li, Y. Li, Y. Feng, W. Hu, and W. Feng, "Hierarchical graphene oxide/polyaniline nanocomposites prepared by interfacial electrochemical polymerization for flexible solid-state supercapacitors," *Journal of Materials Chemistry A*, vol. 3, no. 5, pp. 2135–2143, 2015.

[178] M. Zhang, X. Wang, T. Yang et al., "Polyaniline/graphene hybrid fibers as electrodes for flexible supercapacitors," *Synthetic Metals*, vol. 268, article 116484, 2020.

[179] M. N. Rantho, M. J. Madito, and N. Manyala, "High-performance symmetric supercapacitor device based on carbonized iron-polyaniline/nickel graphene foam," *Journal of Alloys and Compounds*, vol. 819, article 152993, 2020.

[180] A. Jayakumar, Y.-J. Yoon, R. Wang, and J.-M. Lee, "Novel graphene/polyaniline/MnO_x 3D-hydrogels obtained by controlled morphology of MnO_x in the graphene/polyaniline matrix for high performance binder-free supercapacitor electrodes," *RSC Advances*, vol. 5, no. 114, pp. 94388–94396, 2015.

[181] A. Gupta, S. Sardana, J. Dalal et al., "Nanostructured polyaniline/graphene/Fe_2O_3 composites hydrogel as a high-performance flexible supercapacitor electrode material," *ACS Applied Energy Materials*, vol. 3, no. 7, pp. 6434–6446, 2020.

[182] H. Su, T. Wang, S. Zhang et al., "Facile synthesis of polyaniline/TiO_2/graphene oxide composite for high performance supercapacitors," *Solid State Sciences*, vol. 14, no. 6, pp. 677–681, 2012.

[183] B. Dong, B.-L. He, C.-L. Xu, and H.-L. Li, "Preparation and electrochemical characterization of polyaniline/multi-walled carbon nanotubes composites for supercapacitor," *Materials Science and Engineering B*, vol. 143, no. 1–3, pp. 7–13, 2007.

[184] K. R. Prasad and N. Miura, "Polyaniline-MnO_2 composite electrode for high energy density electrochemical capacitor," *Electrochemical and Solid-State Letters*, vol. 7, no. 11, p. A425, 2004.

[185] Y. Huang, S. Bao, and J. Lu, "Flower-like MnO_2/polyaniline/hollow mesoporous silica as electrode for high-performance all-solid-state supercapacitors," *Journal of Alloys and Compounds*, vol. 845, article 156192, 2020.

[186] Z.-A. Hu, Y.-L. Xie, Y.-X. Wang, L.-P. Mo, Y.-Y. Yang, and Z.-Y. Zhang, "Polyaniline/SnO_2 nanocomposite for supercapacitor applications," *Materials Chemistry and Physics*, vol. 114, no. 2–3, pp. 990–995, 2009.

[187] M.-H. Bai, T.-Y. Liu, F. Luan, Y. Li, and X.-X. Liu, "Electrodeposition of vanadium oxide–polyaniline composite nanowire electrodes for high energy density supercapacitors," *Journal of Materials Chemistry A*, vol. 2, no. 28, pp. 10882–10888, 2014.

[188] K.-J. Huang, L. Wang, Y.-J. Liu, H.-B. Wang, Y.-M. Liu, and L.-L. Wang, "Synthesis of polyaniline/2-dimensional graphene analog MoS_2 composites for high-performance supercapacitor," *Electrochimica Acta*, vol. 109, pp. 587–594, 2013.

[189] M. A. Arvizu, F. J. González, A. Romero-Galarza, F. J. Rodríguez-Varela, C. R. Garcia, and M. A. Garcia-Lobato, "Symmetric supercapacitors of PANI coated RuO_2/TiO_2 macroporous structures prepared by electrostatic spray deposition," *Journal of the Electrochemical Society*, vol. 169, no. 2, p. 20564, 2022.

[190] A. G. Tabrizi, N. Arsalani, Z. Naghshbandi, L. S. Ghadimi, and A. Mohammadi, "Growth of polyaniline on rGO-Co_3S_4 nanocomposite for high-performance supercapacitor energy storage," *International Journal of Hydrogen Energy*, vol. 43, no. 27, pp. 12200–12210, 2018.

[191] A. K. Das, S. K. Karan, and B. B. Khatua, "High energy density ternary composite electrode material based on polyaniline (PANI), molybdenum trioxide (MoO_3) and graphene nanoplatelets (GNP) prepared by sono-chemical method and their synergistic contributions in superior supercapacitive performance," *Electrochimica Acta*, vol. 180, pp. 1–15, 2015.

[192] L. E. Kreno, K. Leong, O. K. Farha, M. Allendorf, R. P. Van Duyne, and J. T. Hupp, "Metal–organic framework materials as chemical sensors," *Chemical Reviews*, vol. 112, no. 2, pp. 1105–1125, 2012.

[193] S. I. Abd Razak, I. F. Wahab, F. Fadil, F. N. Dahli, A. Z. Md Khudzari, and H. Adeli, "A review of electrospun conductive polyaniline based nanofiber composites and blends: processing features, applications, and future directions," *Advances in Materials Science and Engineering*, vol. 2015, p. 19, 2015.

[194] M. D. Shirsat, M. A. Bangar, M. A. Deshusses, N. V. Myung, and A. Mulchandani, "Polyaniline nanowires-gold nanoparticles hybrid network based chemiresistive hydrogen sulfide sensor," *Applied Physics Letters*, vol. 94, no. 8, p. 83502, 2009.

[195] J.-S. Do and W.-B. Chang, "Amperometric nitrogen dioxide gas sensor based on PAn/Au/Nafion® prepared by constant current and cyclic voltammetry methods," *Sensors and Actuators B: Chemical*, vol. 101, no. 1–2, pp. 97–106, 2004.

[196] S. G. Pawar, M. A. Chougule, S. Sen, and V. B. Patil, "Development of nanostructured polyaniline–titanium dioxide gas sensors for ammonia recognition," *Journal of Applied Polymer Science*, vol. 125, no. 2, pp. 1418–1424, 2012.

[197] X. Liu, N. Chen, B. Han et al., "Nanoparticle cluster gas sensor: Pt activated SnO_2 nanoparticles for NH_3 detection with ultrahigh sensitivity," *Nanoscale*, vol. 7, no. 36, pp. 14872–14880, 2015.

[198] N. J. Pineau, S. D. Keller, A. T. Güntner, and S. E. Pratsinis, "Palladium embedded in SnO_2 enhances the sensitivity of flame-made chemoresistive gas sensors," *Microchimica Acta*, vol. 187, no. 1, pp. 1–9, 2020.

[199] M. Parthibavarman, B. Renganathan, and D. Sastikumar, "Development of high sensitivity ethanol gas sensor based on Co-doped SnO_2 nanoparticles by microwave irradiation technique," *Current Applied Physics*, vol. 13, no. 7, pp. 1537–1544, 2013.

[200] L. Wang, H. Huang, S. Xiao et al., "Enhanced sensitivity and stability of room-temperature NH_3 sensors using core–shell CeO_2 nanoparticles@cross-linked PANI with p–n heterojunctions," *ACS Applied Materials & Interfaces*, vol. 6, no. 16, pp. 14131–14140, 2014.

[201] N. R. Tanguy, M. Thompson, and N. Yan, "A review on advances in application of polyaniline for ammonia detection," *Sensors and Actuators B: Chemical*, vol. 257, pp. 1044–1064, 2018.

[202] I. Fratoddi, I. Venditti, C. Cametti, and M. V. Russo, "Chemiresistive polyaniline-based gas sensors: a mini review," *Sensors and Actuators B: Chemical*, vol. 220, pp. 534–548, 2015.

[203] A. L. Kukla, Y. M. Shirshov, and S. A. Piletsky, "Ammonia sensors based on sensitive polyaniline films," *Sensors and Actuators B: Chemical*, vol. 37, no. 3, pp. 135–140, 1996.

[204] P. Lobotka, P. Kunzo, E. Kovacova et al., "Thin polyaniline and polyaniline/carbon nanocomposite films for gas sensing," *Thin Solid Films*, vol. 519, no. 12, pp. 4123–4127, 2011.

[205] A. Roy, A. Ray, P. Sadhukhan et al., "Polyaniline-multiwalled carbon nanotube (PANI-MWCNT): room temperature resistive carbon monoxide (CO) sensor," *Synthetic Metals*, vol. 245, pp. 182–189, 2018.

[206] J.-H. Lim, N. Phiboolsirichit, S. Mubeen, M. A. Deshusses, A. Mulchandani, and N. V. Myung, "Electrical and gas sensing properties of polyaniline functionalized single-walled carbon nanotubes," *Nanotechnology*, vol. 21, no. 7, p. 75502, 2010.

[207] T. Sen, N. G. Shimpi, and S. Mishra, "Room temperature CO sensing by polyaniline/Co_3O_4 nanocomposite," *Journal of Applied Polymer Science*, vol. 133, no. 42, 2016.

[208] S. G. Pawar, S. L. Patil, M. A. Chougule et al., "New method for fabrication of CSA doped PANi-TiO_2 thin-film ammonia sensor," *IEEE Sensors Journal*, vol. 11, no. 11, pp. 2980–2985, 2011.

[209] N. G. Deshpande, Y. G. Gudage, R. Sharma, J. C. Vyas, J. B. Kim, and Y. P. Lee, "Studies on tin oxide-intercalated polyaniline nanocomposite for ammonia gas sensing applications," *Sensors and Actuators B: Chemical*, vol. 138, no. 1, pp. 76–84, 2009.

[210] D. Zhang, Z. Wu, and X. Zong, "Flexible and highly sensitive H_2S gas sensor based on in-situ polymerized SnO_2/rGO/PANI ternary nanocomposite with application in halitosis diagnosis," *Sensors and Actuators B: Chemical*, vol. 289, pp. 32–41, 2019.

[211] Y. Li, Y. Wang, X. Jing, and R. Zhu, "Early stage pH profile: the key factor controlling the construction of polyaniline micro/nanostructures," *Journal of Polymer Research*, vol. 18, no. 6, pp. 2119–2131, 2011.

[212] J. Qi, X. Xu, X. Liu, and K. T. Lau, "Fabrication of textile based conductometric polyaniline gas sensor," *Sensors and Actuators B: Chemical*, vol. 202, pp. 732–740, 2014.

[213] X. L. Huang, N. T. Hu, Y. Y. Wang, and Y. F. Zhang, "Ammonia gas sensor based on aniline reduced graphene oxide," *Advanced Materials Research*, vol. 669, pp. 79–84, 2013.

[214] A. A. Athawale and P. P. Katre, "Ag dispersed conducting polyaniline nanocomposite as a selective sensor for ammonia," *Journal of Metastable and Nanocrystalline Materials*, vol. 23, pp. 323–326, 2005.

[215] J.-S. Do and S.-H. Wang, "On the sensitivity of conductimetric acetone gas sensor based on polypyrrole and polyaniline conducting polymers," *Sensors and Actuators B: Chemical*, vol. 185, pp. 39–46, 2013.

[216] H.-D. Zhang, C. C. Tang, Y. Z. Long et al., "High-sensitivity gas sensors based on arranged polyaniline/PMMA composite fibers," *Sensors and Actuators A: Physical*, vol. 219, pp. 123–127, 2014.

[217] H. Tai, Y. Jiang, G. Xie, and J. Yu, "Preparation, characterization and comparative NH_3-sensing characteristic studies of PANI/inorganic oxides nanocomposite thin films," *Journal of Materials Science and Technology*, vol. 26, no. 7, pp. 605–613, 2010.

[218] V. V. Chabukswar, S. Pethkar, and A. A. Athawale, "Acrylic acid doped polyaniline as an ammonia sensor," *Sensors and Actuators B: Chemical*, vol. 77, no. 3, pp. 657–663, 2001.

Hindawi
International Journal of Polymer Science
Volume 2022, Article ID 5252528, 13 pages
https://doi.org/10.1155/2022/5252528

Research Article

Development of Lightweight Polymer Laminates for Radiation Shielding and Electronics Applications

S. Vignesh[1], **J. T. Winowlin Jappes**[1], **S. Nagaveena**[2], **R. Krishna Sharma**[3], **M. Adam Khan**[1], **Chaitali V. More**[4], **N. Rajini**[1] and **Temel Varol**[5]

[1]*Department of Mechanical Engineering, Kalasalingam Academy of Research and Education, 626126, Tamilnadu, India*
[2]*Department of Nanoscience and Nanotechnology, S.T. Hindu College, 629002, Nagercoil, Tamilnadu, India*
[3]*Department of Physics, S.T. Hindu College, 629002, Nagercoil, Tamilnadu, India*
[4]*Nuclear Physics Research Laboratory, Dr. B.A.M. University, 431004, Aurangabad, India*
[5]*Department of Metallurgical and Materials Engineering, Karadeniz Technical University, Trabzon, Turkey*

Correspondence should be addressed to J. T. Winowlin Jappes; winowlin@klu.ac.in

Received 29 June 2022; Accepted 3 September 2022; Published 8 October 2022

Academic Editor: Wen Shyang Chow

The present study portrays the development of lightweight epoxy laminates filled with boron carbide (B_4C) and lead (Pb) particles through a novel layered molding and curing route. Six different laminates of single and tri-layers were prepared with varying compositions and were subjected to thermal, radiation shielding, and dielectric studies. Radiation shielding test were done using a narrow beam setup with six different sources such as Cobalt-57 (Co^{57}-122 keV), Barium-133 (Ba^{133}-356 keV), Sodium-22 (Na^{22}-511 and 1275 keV), Cesium-137 (Cs^{137}-662 keV), Manganese-54 (Mn^{54}-840 keV), and Cobalt-60 (Co^{60}-1170 and 1330 keV). The dielectric studies were done to understand the dielectric constant, dielectric loss factor, and AC conductivity at different temperature and frequency ranges. From the characterizations, it was found that the thermal stability of the single-layered sample increased with respect to the addition of B_4C and Pb particles, which may be due to the thermally stable nature of the particles. The radiation shielding study of the samples witnessed the superior characteristics and radiation shielding ability of sample D (40% Pb) and sample E with Pb cladding at incident gamma radiation energy of 662 keV. The dielectric constant of the samples increased significantly at higher temperatures and the dielectric loss factor increased with an increase in temperature and decreased with an increase in frequency. The AC conductivity of the samples increased with respect to an increase in temperature and frequency.

1. Introduction

The ionizing radiation finds a great place in various industrial sectors such as medical, spacecraft, nuclear power sectors, and not limited to these. Exposure to ionizing radiation leads to harmful effects on both biotic and abiotic species around the globe. It is obvious that these mentioned sectors have to find a precautionary measure to shield these harmful radiations as well. Lead (Pb), a traditionally used shielding material, suits the purpose of shielding. However, due to its toxic nature, high density, and poor mechanical strength, there is a huge demand for alternative materials [1, 2]. Polymer composites have nowadays become a potential alternative for lead-based radiation shielding materials. Several researchers have focused on the development of particle-filled shielding materials based on rubber, epoxy, polyethylene glycol, and unsaturated polyester resins and reported their suitability for the radiation attenuation applications [3, 4]. Similarly, in microelectronics, the replacement of passive electronic components with passive embedded components attracts researchers due to the minimal utilization of size, reduction in cost, and flexibility in the circuit design. Particularly, in conductive polymer electronics, the need for a thin layer of dielectrics with good dielectric constant, loss factor, and conductivity makes researchers think toward a positive alternative [5].

Epoxy, a capable hinderer of radiation, is studied extensively by researchers due to its good characteristics such as

density, mechanical property, and stability. Moreover, it could be manufactured easily when compared with metal matrix composites. Also, epoxy possesses good dimensional stability, good adhesion properties, high resistance to heat, and good chemical stability. Additionally, the presence of an aromatic ring in its chemical composition makes it suitable for gamma and neutron radiation shielding applications [6]. Boron carbide (B_4C) among ceramic materials is nowadays a promising replacement for Pb owing to its superior hardness, neutron absorption capability, and high melting point [7–10]. Several B_4C-based radiation-shielding materials were developed recently for neutron radiation-shielding applications [11–14]. However, works are limited to the fabrication of layered composite laminates for radiation shielding. On the other hand, epoxy displays a very low dielectric constant, which is less than 10 and is unfit for practical electronics applications. However, an increase in the dielectric constant can be achieved by adding filler particles to the epoxy matrix. This, in turn, leads to a detrimental effect on the mechanical properties of the material. Hence, proper care must be ensured for enhancing the dielectric constant by precisely altering the filler particle content [15]. Some works support the suitability of Pb and B_4C filled in the epoxy matrix for X-ray attenuation and found an improvement in shielding efficiency with increased addition of particles [16].

Hence, in this work, efforts are made to manufacture single- and tri-layered epoxy-based laminates dispersed with B_4C and Pb filler particles via a layered molding and curing route for shielding radioactive rays and to attempt the development of conductive polymeric laminates for electronics applications. The prepared laminates were subjected to gamma radiation, dielectric characterization, and the shielding characteristics, and electrical properties were studied.

2. Materials and Methods

2.1. Materials. Epoxy (Grade LY566) and the corresponding hardener (Grade HY951) used for this work were procured from Herenba Resins Pvt. Ltd., Chennai. Commercially available metallic particles B_4C (99.9%) with particle size 10 μm were purchased from Neena Metal Mart, New Delhi, and the powdered lead (Pb) particles (99.9%) of particle size 10 μm were purchased from Alpha Chemika, Mumbai. The confirmation of the powdered particles was done by SEM equipped with an electro dispersive spectrum analyzer using JEOL-JSM-5600LV under 20 kV and exposure time of 50 seconds and is depicted in Figures 1(a) and 1(b).

2.2. Experimental Methods. The composite laminates for radiation shielding were effectively prepared through a layered molding and curing route [17, 18], and are depicted in Figure 1(c). Rectangular molds of dimension 300 mm × 130 mm × 15 mm were used for making the laminates for radiation shielding. Four different samples of various compositions for single-layered studies and two different samples with three layers were made, and the properties of the prepared laminates were tabulated in Table 1. Initially, the epoxy matrix was taken in the beaker and the B_4C and Pb filler particles were added. The particles were mixed thoroughly for 30 minutes using mechanical stirring to eliminate the formation of voids and for ensuring proper dispersion of particles. The procedure is followed by the addition of hardener in the epoxy–hardener weight ratio of 2 : 1, which is then mixed mechanically for 20 minutes. After thorough mixing, the solution was poured into the glass mold and was allowed to cure for 24 hours. Similarly, layered samples were made at a definite interval of 45 minutes after the pouring of the first and the subsequent layers. The same procedure was followed for the preparation of all the layered samples. The samples were allowed to cure for 24 hours before removing from the mold. Proper care and safety measures were ensured during the handling and preparation of lead samples. The samples prepared were as shown in Figure 1(d). The samples were powdered for studying the thermal degradation and the samples with dimensions 15 mm × 15 mm × 9 mm were made for studying the radiation-shielding properties. The samples were cut with dimensions 10 mm × 10 mm × 3 mm for performing the dielectric studies. The thermographs of the samples were recorded using a Thermogravimetric Analyzer (TGA-Q500TA Instruments, USA) with a range of 30–800°C in Nitrogen atmosphere at a heating rate of 20°C/min. Furthermore, the samples were subjected to density measurements through the Archimedes method utilized with calibrated single pan electrical balance and ethanol solution. The experimental apparent density is measured using the following equation for 3 samples for each composition:

$$\rho_s = \frac{m_1}{m_2 - m_3}\rho_e, \tag{1}$$

where ρ_s and ρ_e are the density of the sample and ethanol, respectively, m_1 and m_2 and m_3 are the mass of the sample weighed in the balance, mass of the sample hanging on the arm of the balance in the air, and mass of the sample hanging on the arm of the balance immersed in an ethanol solution, respectively.

2.3. Shielding Parameters. Mass attenuation coefficient (μ_m) is the predominant parameter, which witnesses the shielding capacity of the material, explained as the ratio of linear attenuation coefficient and the density of the sample. It is measured through the narrow beam good setup. Furthermore, various parameters such as linear attenuation coefficient (μ), half value layer (HVL), tenth value layer (TVL), and mean free path (MFP) were calculated using the basic relations as shown in the equations.

$$\mu = \mu_m \rho, \tag{2}$$

$$\mathrm{HVL} = \frac{\ln 2}{\mu}, \tag{3}$$

$$\mathrm{TVL} = \frac{\ln 10}{\mu}, \tag{4}$$

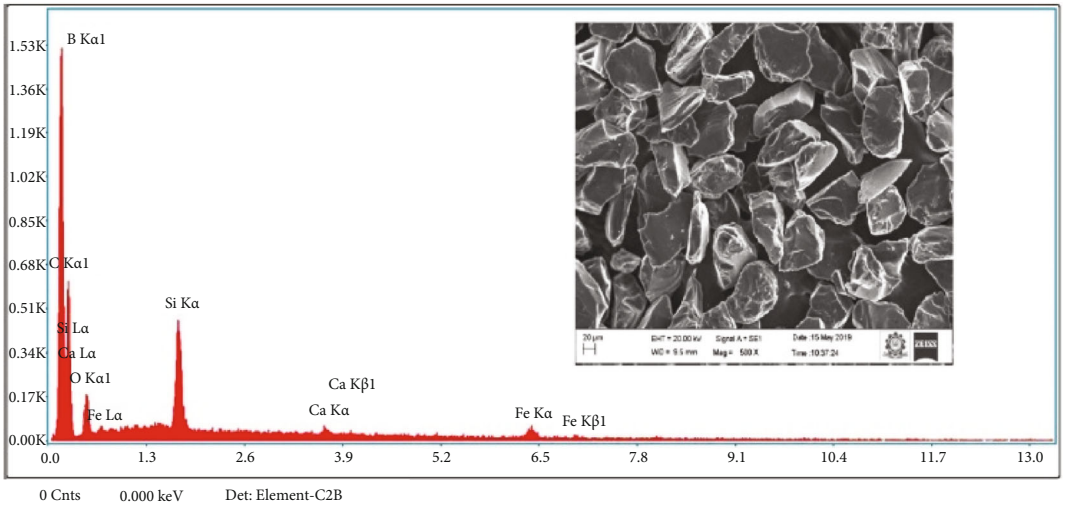

(a)

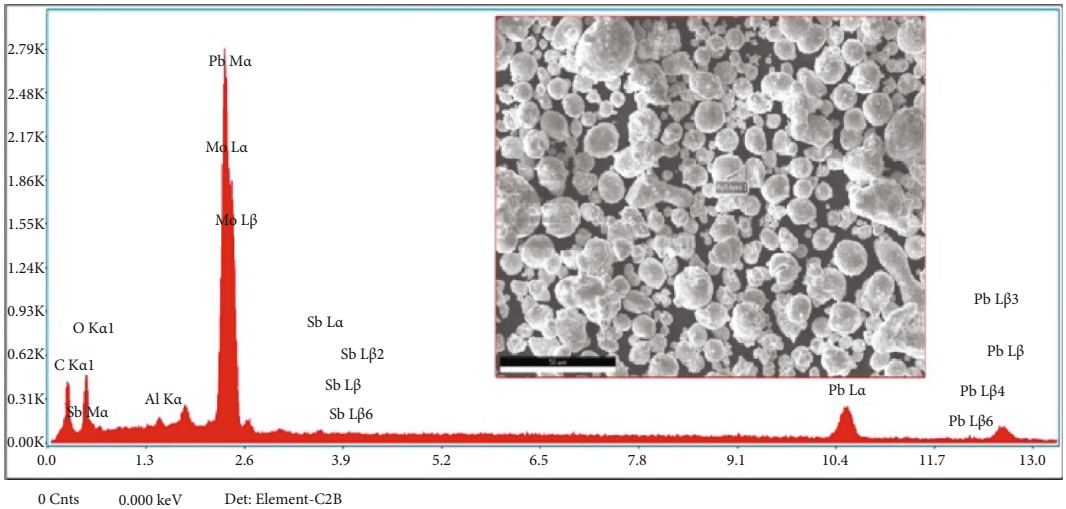

(b)

Figure 1: Continued.

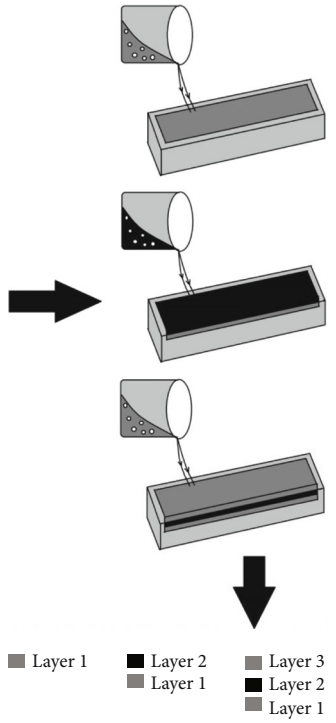

(c)

(d)

Figure 1: (a) SEM-EDS confirmation of B4C particles; (b) SEM-EDS confirmation of Pb particles; (c) manufacturing route-layered molding and curing, and (d) as-prepared samples for mechanical and radiation shielding studies.

Table 1: Composition of the samples.

Samples	Composition of single-layered composites (wt%)		Density (g/cm^3)	
	B_4C	*Pb*	*Theoretical*	*Experimental*
A	20	10	1.389	1.345 ± 0.005
B	20	20	1.557	1.520 ± 0.012
C	20	30	1.788	1.712 ± 0.003
D	20	40	1.995	1.956 ± 0.006
Composition of tri-layered samples (wt%)				
Samples	**Layer 1**	**Layer 2**	**Layer 3**	*Theoretical*	*Experimental*
E	*Pb-20*	*B_4C-20*	*Pb-20*	2.099	1.998 ± 0.003
F	*B_4C*-20	*Pb*-20	*B_4C*-20	1.858	1.802 ± 0.010

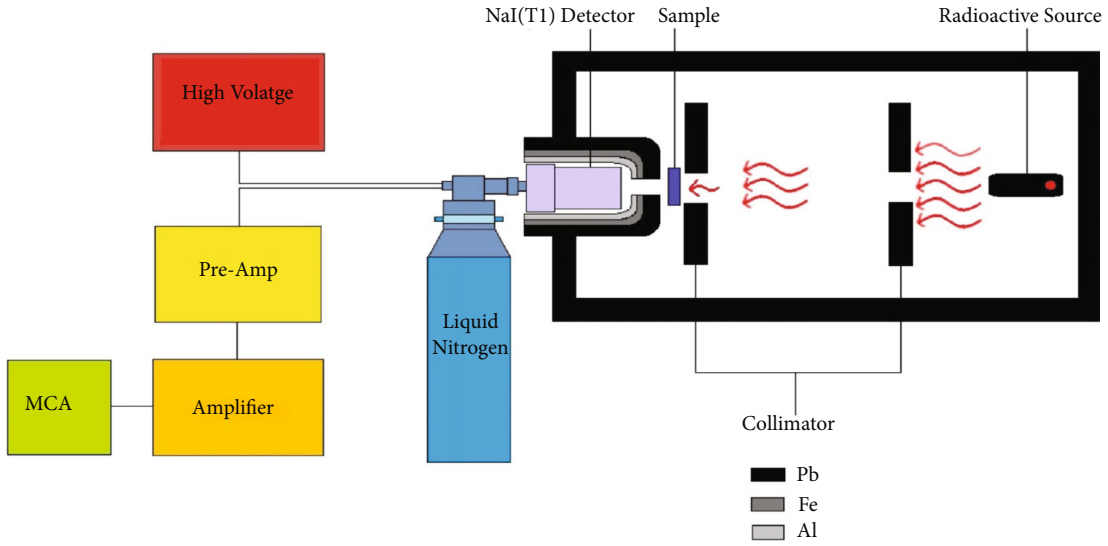

Figure 2: Narrow beam setup for radiation studies.

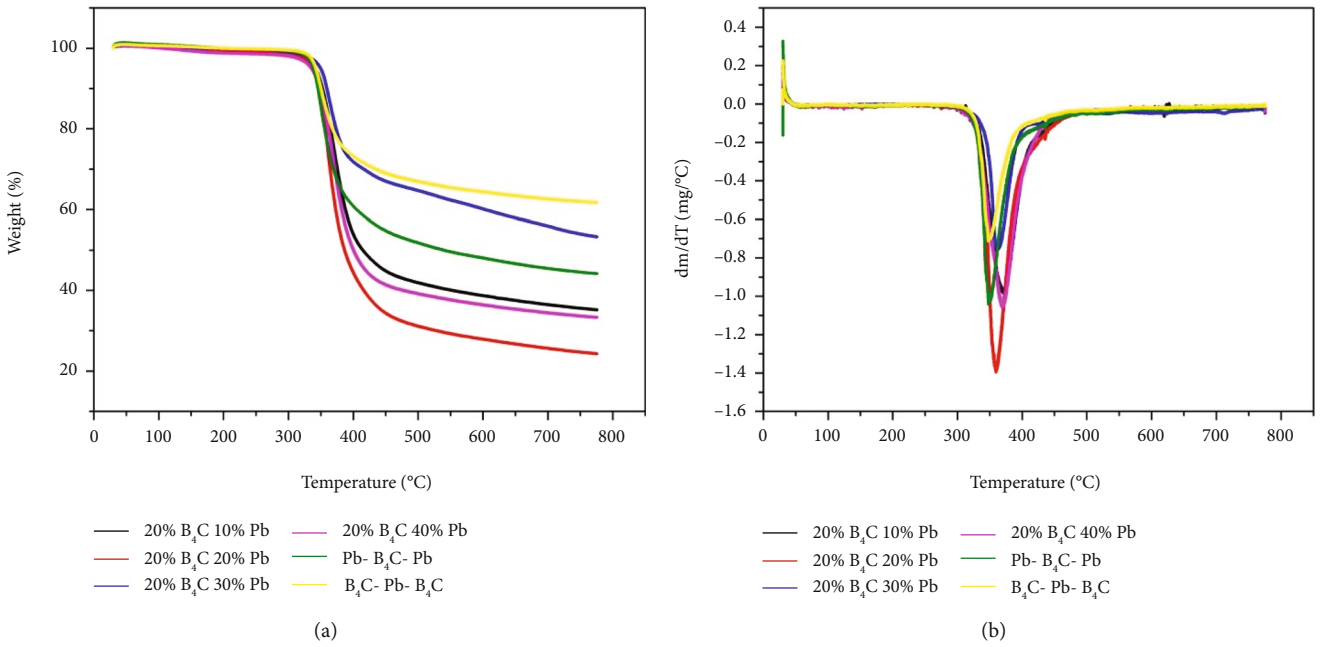

Figure 3: (a) Primary thermograms of samples and (b) derivative thermograms of samples.

$$\mathrm{MFP} = \frac{1}{\mu}. \tag{5}$$

The HVL and TVL are defined as the average distance required for attenuating the incident gamma radiation flux by a half and a tenth of its value, respectively. MFP could be understood as the average distance traversed by a gamma ray of given energy in a medium until it interacts with the same medium [19].

2.4. Radiation-shielding Studies. The prepared single- and tri-layered composite laminates were subjected to

Table 2: Degradation temperature of the samples.

Sample nomenclature	Degradation temperature (°C)		
	Onset	Inflection	End-set
A	341	377	452
B	338	386	467
C	349	388	487
D	357	411	512
E	338	356	486
F	342	365	495

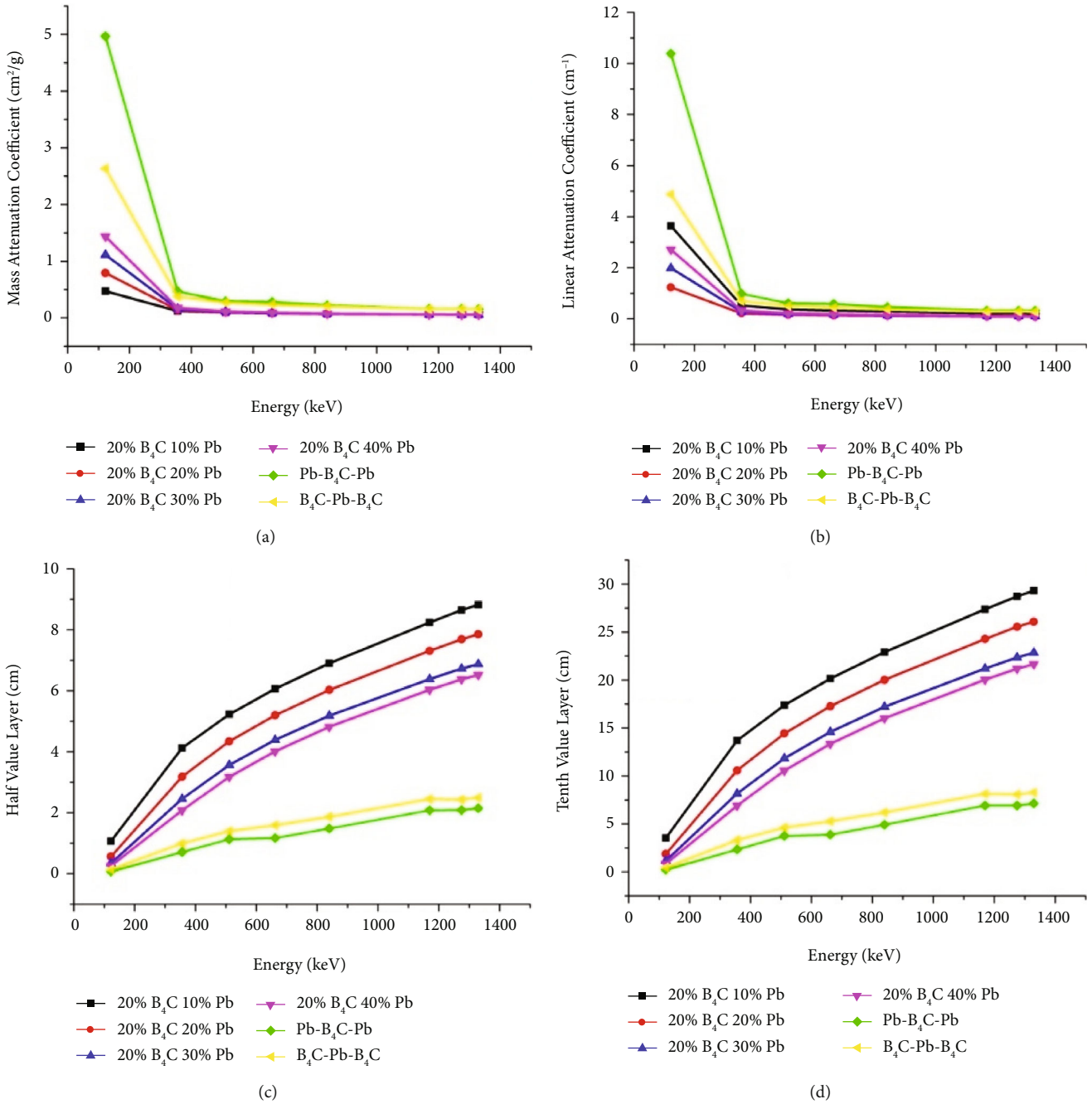

Figure 4: Continued.

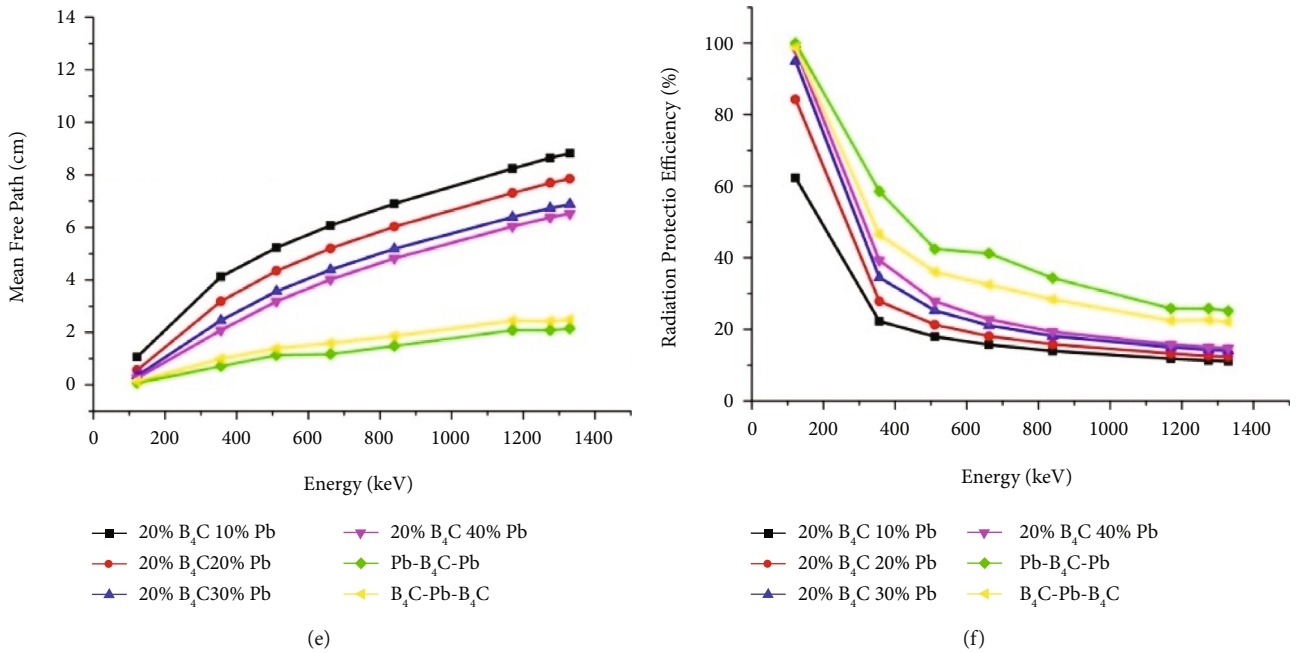

FIGURE 4: (a) Mass attenuation coefficient vs gamma radiation energy. (b) Linear attenuation coefficient vs gamma radiation energy; (c) half value layer (HVL) vs gamma radiation energy; (d) tenth value layer vs gamma radiation energy (TVL); (e) mean free path (MFP) vs gamma radiation energy, and (f) radiation protection efficiency vs gamma radiation energy.

radiation-shielding studies through the narrow beam good geometry setup as depicted in Figure 2. Co^{57} (122 keV), Ba^{133} (356 keV), Na^{22} (511 and 1275 keV), Cs^{137} (662 keV), Mn^{54} (840 keV), and Co^{60} (1170 and 1330 keV) are the six different sources of radioactive radiation. The NaI (Tl) scintillation detector was used to detect the gamma radiations. The signals from the detector (8.2% energy resolution at 662 keV) were recorded in an EG & GORTEC-13 bit plug-in card coupled with a PC/AT. The setup was checked for its stability and reproducibility prior to and after every set of runs.

2.5. Electrical Characterization. The samples prepared were subjected to electrical characterization to understand the various dielectric behaviors such as the capacitance C_p and dielectric loss factor tanδ. The studies were conducted at various temperatures ranging from 40°C to 150°C and also with a range of frequencies from 100 Hz, 1 kHz, 10 kHz, 100 kHz, and 1 MHz. LCR Meter Aglient 4284A through the parallel plate capacitor method was used for the study. The samples were subjected to annealing in the sample holder at 160°C prior to observations. The temperature was in a controlled environment with an accuracy of ±0.5°C and the readings were taken during the cooling process of the sample. The air capacitance C_a was measured and the dielectric constant of the samples was calculated using the formula $\varepsilon_r = C_p/C_a$. It should be also noted that the AC conductivity of the prepared samples was determined by the following relation:

$$\sigma_{AC} = \varepsilon_0 \varepsilon_r \omega \tan \delta, \quad (6)$$

where ε_0 is the permittivity of free space and ω is the angular frequency and is given by $\omega = 2\pi f$, and f is the applied frequency.

3. Results and Discussion

3.1. Thermal Studies. Figures 3(a) and 3(b) depicted above clearly elucidates the thermal stability of the as-prepared samples through primary and derivative thermograms. It is evident from Figure 3(a) that single-step degradation is observed in all the samples in a Nitrogen environment. The degradation temperatures (onset, inflection, and end-set) of the samples are tabulated in Table 2. The initial degradation temperature (onset) was determined at 5% weight loss of the samples. The inflection temperature and the end-set temperature were determined at the moment of sudden steep in weight loss and at the end of attaining constant degradation of the sample, respectively. It could be understood from Figure 3(a) that the onset temperatures of all the samples are between 330°C and 360°C. The inflection temperature ranges from 377°C to 411°C in the case of single-layered samples and is 356°C and 365°C for tri-layered samples. The initial decomposition of the samples could be resulted due to the degradation of polymer chains in the epoxy matrix [20]. The rise in inflection temperature could be attributed to the addition of thermally stable metallic particles such as B_4C and Pb. The derivative thermogram depicted in Figure 3(b) illustrates the shift in the plateau corresponding to sample D to the right side, which could be obviously due to the better thermal stability of the sample. On the other hand, the tri-layered sample with B_4C cladding has shown improved thermal stability when compared to

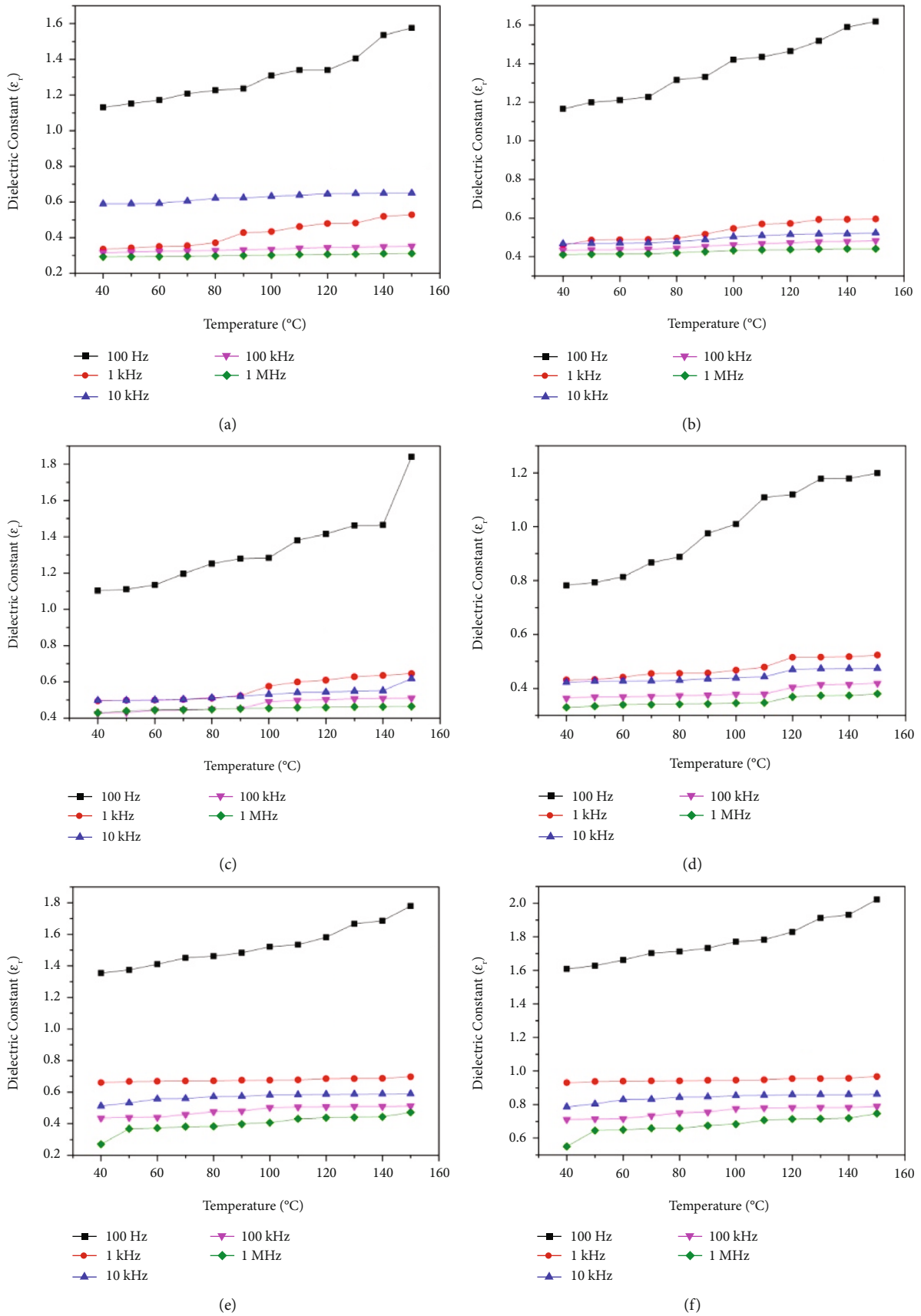

Figure 5: Dielectric constant as a function of temperature and frequency for (a) sample A, (b) sample B, (c) sample C, (d) sample D, (e) sample E and (f) sample F.

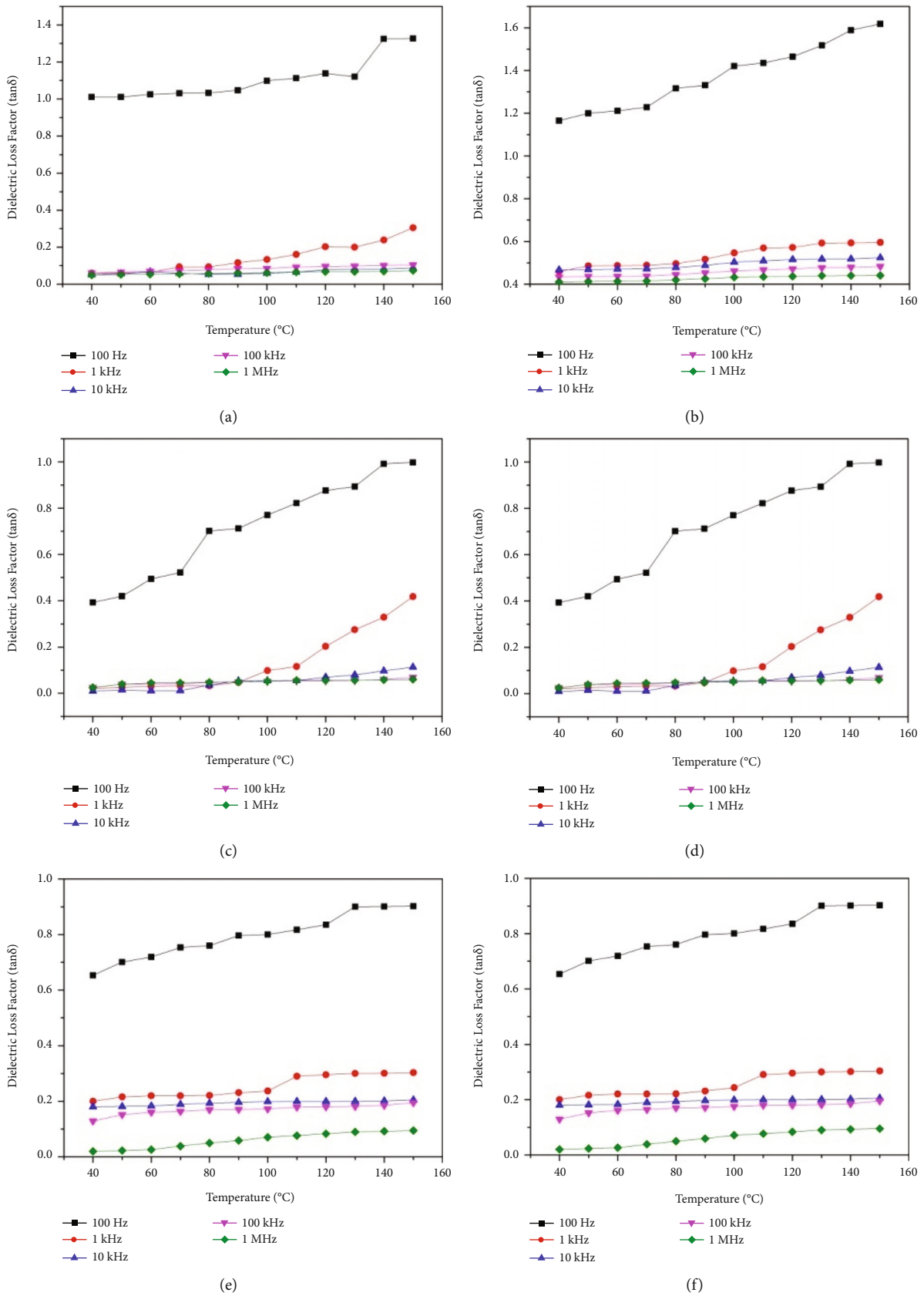

Figure 6: Dielectric loss factor as a function of temperature and frequency for (a) sample A, (b) sample B, (c) sample C, (d) sample D, (e) sample E, and (f) ample F.

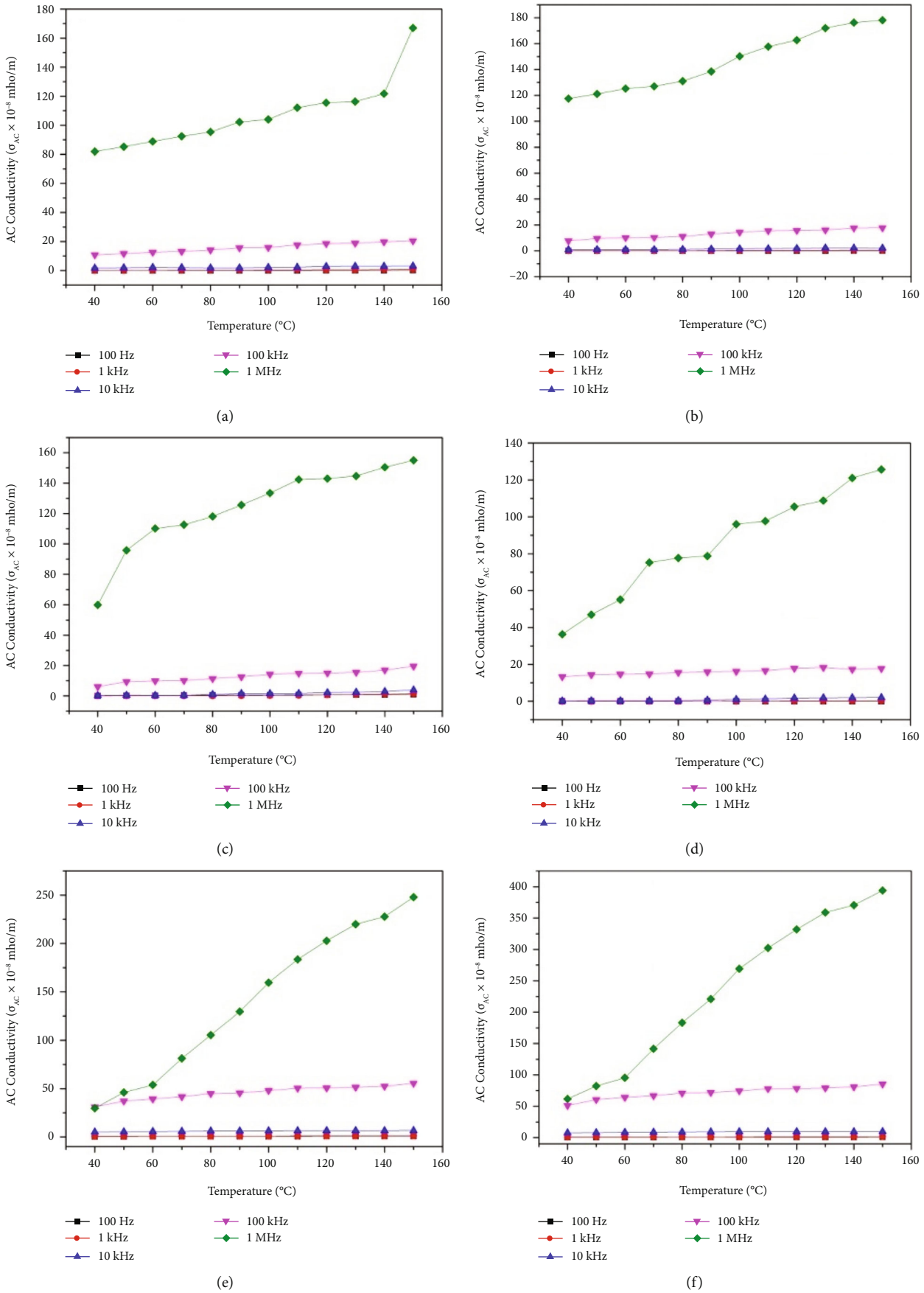

Figure 7: AC conductivity as a function of temperature and frequency for (a) sample A, (b) sample B, (c) sample C, (d) sample D, (e) sample E, (f) sample F.

that of the Pb cladding. The resulting thermal stability throughout the as-prepared samples could be resulted owing to the hindering effect of B_4C and Pb on the mobility of polymer chain due to the inert characteristics of B_4C and Pb [20].

3.2. Radiation-shielding Studies. Figure 4(a) shows the mass attenuation coefficient (μ_m) of the samples with respect to the incident radiation energy. It is evident from the graph that μ_m for all the samples (both single and tri-layered) decreases with an increase in incident gamma energy. However, μ_m of the tri-layered sample showed exemplary results at low gamma energies. Particularly, the sample with Pb cladding has a very good mass attenuation coefficient (5 cm^2/g). On the other hand, the sample with B_4C cladding showed a mass attenuation value of 2.85 cm^2/g, which is nearly half that of the Pb cladding. The reason for the phenomenon is obvious that the thickness of the sample plays a vital role in accessing the radiation-shielding performance [20]. However, the thickness beyond 10 mm reduced the dependency of shielding efficiency on the thickness of the samples [6]. Moreover, the decrease in μ_m values is attributed to Compton scattering, which is predominant in higher energy ranges [6]. The linear attenuation coefficient calculated by using the formula mentioned in equation (2) is in accordance with the measure of μ_m and the density of the samples and is depicted in Figure 4(b). It should be noted that HVL, TVL, and MFP are the other predominant parameters, which provide valid information about the penetration of radiation in a material and its shielding capabilities. The above parameters for the as-prepared samples are depicted in Figures 4(c)–4(e) and are obvious that these parameters increase with an increase in incident gamma energy. This could be ascribed due to the notion that an increase in incident energy leads to a decrease in the chance of interactions between the photons in the material [19]. Moreover, it is well known that the sample with lower HVL, TVL, and MFP values results in extraordinary shielding capabilities due to the shorter distance between two interactions of the radiation [19]. From Figures 4(c)–4(e), the performance of tri-layered samples is obvious owing to the above notions. However, among the single-layered samples, the one with 40% Pb (sample D) shows better shielding properties when compared with the other as-prepared samples. This could be attributed by the increased addition of Pb.

Radiation protection efficiency (RPE) is the measure of percentage effectiveness in shielding the incident gamma radiations. The RPE of as-prepared samples is illustrated in Figure 4(f), and it is obvious from the graph that all the samples showcase a similar trend in shielding radiation, that is, efficiency decreases with an increase in incident gamma energy. Among the samples, the tri-layered samples with Pb cladding showcases better shielding efficiency of nearly 50% at 662 keV owing to the increased presence of Pb. Moreover, the presence of Pb-epoxy layer could result in in-elastic and elastic scattering leading to increased radiation shielding. However, the mid layer with B_4C-epoxy could result in photoelectric absorption and elastic scattering leading to shield low-energy gamma rays emerged from layer 1 [21]. On the other hand, the single-layered sample with 10% Pb displays poorer RPE owing to the reduced addition of Pb.

3.3. Dielectric Properties. Figures 5(a)–5(f) depicts the dielectric constant of sample A to sample F with respect to the temperature and frequency. It is obvious from the figure that dielectric constant increases significantly to a considerable extent with respect to temperature. The segmental mobility of polymer chains could be the possible phenomenon behind the increase in dielectric constant with respect to temperature. It is obvious that the enhancement of orientation of dipole due to segmental mobility leads to the increase in dielectric constant [22]. Moreover, at low frequencies, thermal activation predominates the dipole orientation and segmental mobility, resulting in increased dielectric constant. On the other hand, at higher frequencies, the molecular dipoles could not trace the increment in the frequency owing to lower thermal activation resulting in a lower dielectric constant in all the as-prepared samples. Nevertheless, an increase in particle addition (Pb addition up to 30%) led to an increase in the dielectric constant of the samples. This is because of the fact that the incorporation of conducting fillers in the conductor-insulator composites results in the formation of electrically heterogeneous material. Similarly, the sample with Pb core has showcased significant improvement in dielectric constant when compared to that of the B_4C core. Furthermore, the improvement in dielectric constant due to particle addition could be attributed due to the increase in interfacial polarization [23, 24]. The samples invariably displayed a similar trend in the case of the dielectric loss factor ($\tan\delta$) which is much obvious from Figures 6(a)–6(f). The dielectric loss factor found to increase with an increase in temperature and decrease with an increase in frequency and is owing to the thermal independence at higher frequencies. This is due to the inability of the molecular dipoles to follow the high frequency [25]. Figures 7(a)–7(f) illustrates the AC conductivity of the samples with respect to temperature and frequency. It is clear from Figures 7(a)–7(f) that the AC conductivity of the samples increases with respect to the increase in temperature and frequency. Here, both the single- and tri-layered samples exhibit enhanced AC conductivity when the particle composition is increased. The sample with Pb core displayed better AC conductivity than that of the B_4C core. This could be owing to the fact that in conductor-insulator composites, electron tunneling, a phenomenon in which the electrons will tunnel in between clusters separated by insulated polymeric layers, is the very obvious reason for the enhancement in AC conductivity [25–28].

4. Conclusion

In this work, six different laminates of epoxy matrix dispersed with B_4C and Pb particles were developed through a layered molding and curing route. The samples were subjected to radiation-shielding, thermal stability, and dielectric studies, and the results are concluded as below.

(i) The thermal stability of the single-layered sample increased with respect to the addition of B_4C and Pb particles, which may be due to the thermally stable nature of the particles. Similarly, the tri-layered samples with B_4C cladding portrayed better thermal stability compared to that of Pb cladding owing to the inert characteristics of B_4C that hinders the mobility of epoxy polymer chain due to the thermal effect.

(ii) The radiation shielding study of the samples witnesses the superior characteristics and radiation-shielding ability of sample D (40% Pb) and sample E with Pb cladding at incident gamma radiation energy of 662 keV.

(iii) At lower energies, all the samples possessed nearly 100% RPE and, at 662 keV, sample E possessed nearly 42% which is much higher than that of all the samples. This results in the usage of the as-prepared sample for radiation-shielding application of low-energy radiation involved in spent fuel caskets and containers.

(iv) The dielectric constant of the samples increased significantly at higher temperatures, which could be due to the segmental mobility of polymer chains.

(v) On the other hand, at higher frequencies, the molecular dipoles could not trace the increment in the frequency owing to lower thermal activation resulting in a lower dielectric constant in all the as-prepared samples.

(vi) The dielectric loss factor found to increase with an increase in temperature and decrease with an increase in frequency and is owing to the thermal independence at higher frequencies.

(vii) The AC conductivity of the samples increased with respect to an increase in temperature and frequency, which could be owing to the phenomenon of tunneling of electrons.

Data Availability

None of the data are available elsewhere.

Conflicts of Interest

The authors declare that there are no conflicts of interest regarding the publication of this paper.

Acknowledgments

The authors greatly thank the All India Council of Technical Education (AICTE), India for supporting this project under Research Promotion Scheme (RPS) 8-64/FDC/RPS (POLICY-1)/2019-20.

References

[1] N. Abbasova, Z. Yüksel, E. Abbasov, H. Gülbiçim, and M. Ç. Tufan, "Investigation of gamma-ray attenuation parameters of some materials used in dental applications," *Results in Physics*, vol. 12, pp. 2202–2205, 2019.

[2] A. E.-S. Abdo, M. A. M. Ali, and M. R. Ismail, "Natural fibre high-density polyethylene and lead oxide composites for radiation shielding," *Radiation Physics and Chemistry*, vol. 66, no. 3, pp. 185–195, 2003.

[3] C. V. More, Z. Alsayed, M. Badawi, A. Thabet, and P. P. Pawar, "Polymeric composite materials for radiation shielding: a review," *Environmental Chemistry Letters*, vol. 19, no. 3, pp. 2057–2090, 2021.

[4] R. Frano, G. P. Lo, and G. Forasassi, "Thermal analysis of a spent fuel cask in different transport conditions," *Energy*, vol. 36, no. 4, pp. 2285–2293, 2011.

[5] B. Wetzel, P. Rosso, F. Haupert, and K. Friedrich, "Epoxy nanocomposites–fracture and toughening mechanisms," *Engineering Fracture Mechanics*, vol. 73, no. 16, pp. 2375–2398, 2006.

[6] R. Adeli, S. P. Shirmardi, and S. J. Ahmadi, "Neutron irradiation tests on B_4C/epoxy composite for neutron shielding application and the parameters assay," *Radiation Physics and Chemistry*, vol. 127, pp. 140–146, 2016.

[7] S.-Y. Fu, X.-Q. Feng, B. Lauke, and Y.-W. Mai, "Effects of particle size, particle/matrix interface adhesion and particle loading on mechanical properties of particulate–polymer composites," *Composites Part B: Engineering*, vol. 39, no. 6, pp. 933–961, 2008.

[8] B. Bittmann, F. Haupert, and A. K. Schlarb, "Preparation of TiO_2 epoxy nanocomposites by ultrasonic dispersion and resulting properties," *Journal of Applied Polymer Science*, vol. 124, no. 3, pp. 1906–1911, 2012.

[9] A. Yasmin, J.-J. Luo, and I. M. Daniel, "Processing of expanded graphite reinforced polymer nanocomposites," *Composites Science and Technology*, vol. 66, no. 9, pp. 1182–1189, 2006.

[10] M. S. Goyat, S. Ray, and P. K. Ghosh, "Innovative application of ultrasonic mixing to produce homogeneously mixed nanoparticulate-epoxy composite of improved physical properties," *Composites Part A: Applied Science and Manufacturing*, vol. 42, no. 10, pp. 1421–1431, 2011.

[11] J. Kim, B.-C. Lee, Y. R. Uhm, and W. H. Miller, "Enhancement of thermal neutron attenuation of nano-B_4C,-BN dispersed neutron shielding polymer nanocomposites," *Journal of Nuclear Materials*, vol. 453, no. 1–3, pp. 48–53, 2014.

[12] Ü. Kara, H. O. Tekin, A. Calik, and I. Akkurt, "Performance of boron-carbide as radiation shielding," *Acta Physica Polonica A*, vol. 128, no. 2B, p. B-335, 2015.

[13] C. Tan, R. James, B. Dong et al., "Characterization of a boron carbide-based polymer neutron sensor," *Nuclear Instruments and Methods in Physics Research Section A: Accelerators, Spectrometers, Detectors and Associated Equipment*, vol. 803, pp. 82–88, 2015.

[14] Z. Soltani, A. Beigzadeh, F. Ziaie, and E. Asadi, "Effect of particle size and percentages of boron carbide on the thermal neutron radiation shielding properties of HDPE/B_4C composite: experimental and simulation studies," *Radiation Physics and Chemistry*, vol. 127, pp. 182–187, 2016.

[15] B. Samanta, P. Kumar, and C. Prakash, "Effect of sintering temperature and Cu-rich secondary phase on dielectric

properties of microwave processed $CaCu_3Ti_4O_{12}$ ceramics," *Ferroelectrics*, vol. 517, no. 1, pp. 46–57, 2017.

[16] S. A. Hashemi, S. M. Mousavi, R. Faghihi, M. Arjmand, S. Sina, and A. M. Amani, "Lead oxide-decorated graphene oxide/epoxy composite towards X-ray radiation shielding," *Radiation Physics and Chemistry*, vol. 146, pp. 77–85, 2018.

[17] S. Vignesh, J. T. Jappes, K. M. Adam, and T. Varol, "Mechanical loading and tribological studies on boron carbide (B_4C) and lead (Pb) particles dispersed epoxy-based multilayered composites," *Advances in Materials Science and Engineering*, p. 8 , 2022.

[18] S. Vignesh, P. Jothiraj, J. T. Winowlin Jappes et al., "Investigation on mechanical behavior of B_4C dispersed advanced novel composites fabricated through molding and curing," *Materials Today: Proceedings*, vol. 46, pp. 7639–7642, 2021.

[19] C. V. More, R. M. Lokhande, and P. P. Pawar, "Effective atomic number and electron density of amino acids within the energy range of 0.122–1.330 MeV," *Radiation Physics and Chemistry*, vol. 125, pp. 14–20, 2016.

[20] M. K. Lee, J. K. Lee, J. W. Kim, and G. J. Lee, "Properties of B_4C–PbO–Al (OH) 3-epoxy nanocomposite prepared by ultrasonic dispersion approach for high temperature neutron shields," *Journal of Nuclear Materials*, vol. 445, no. 1–3, pp. 63–71, 2014.

[21] G. Hu, H. Huasi, Q. Yang, Y. Bo, and W. Sun, "Study on the design and experimental verification of multilayer radiation shield against mixed neutrons and γ-rays," *Nuclear Engineering and Technology*, vol. 52, no. 1, pp. 178–184, 2020.

[22] X. Sui, W. Zhou, L. Dong et al., "Epoxy composites with added aluminum with binary particle size distribution for enhanced dielectric properties and thermal conductivity," *Journal of Electronic Materials*, vol. 45, no. 11, pp. 5974–5984, 2016.

[23] V. Singh, A. R. Kulkarni, and T. R. Rama Mohan, "Dielectric properties of aluminum–epoxy composites," *Journal of Applied Polymer Science*, vol. 90, no. 13, pp. 3602–3608, 2003.

[24] S. Nagaveena and C. K. Mahadevan, "Preparation by a facile method and characterization of amorphous and crystalline nickel sulfide nanophases," *Journal of Alloys and Compounds*, vol. 582, pp. 447–456, 2014.

[25] B. Samanta, P. Kumar, D. Nanda, and R. Sahu, "Dielectric properties of epoxy-Al composites for embedded capacitor applications," *Results in Physics*, vol. 14, article 102384, 2019.

[26] Z. M. Elimat, A. M. Zihlif, and G. Ragosta, "Study of ac electrical properties of aluminium–epoxy composites," *Journal of Physics D: Applied Physics*, vol. 41, no. 16, article 165408, 2008.

[27] Z. Wang, W. Zhou, X. Sui et al., "Dielectric studies of al nanoparticle reinforced epoxy resin composites," *Polymer Composites*, vol. 39, no. 3, pp. 887–894, 2018.

[28] S. Vignesh, J. T. Winowlin Jappes, S. Nagaveena, K. Sankaranarayanan, R. Krishna Sharma, and N. C. Brintha, "A study on mechanical and dielectric properties of B_4C and Al dispersed single-layered epoxy-based polymer composites fabricated through molding and curing route," *Materials Physics & Mechanics*, vol. 48, no. 3, 2022.

Hindawi
International Journal of Polymer Science
Volume 2022, Article ID 8331886, 10 pages
https://doi.org/10.1155/2022/8331886

Research Article

Characterization and Performance Evaluation of PIN Diodes and Scope of Flexible Polymer Composites for Wearable Electronics

Sonia Sharma,[1] **Rahul Rishi**,[1] **Chander Prakash**,[2] **Kuldeep K. Saxena**,[3] **Dharam Buddhi**,[4] **and N. Ummal Salmaan**[5]

[1]*University Institute of Engineering and Technology, Maharshi Dayanand University, Rohtak 124001, India*
[2]*School of Mechanical Engineering, Lovely Professional University, Phagwara, Punjab 144411, India*
[3]*Department of Mechanical Engineering, GLA University, Mathura, Uttar Pradesh 281406, India*
[4]*Division of Research & Innovation, Uttaranchal University, Dehradun, Uttarakhand 248007, India*
[5]*Department of Automotive Engineering, Aksum University, Axum, Ethiopia*

Correspondence should be addressed to N. Ummal Salmaan; ummalsalmaan90@gmail.com

Received 9 June 2022; Revised 28 June 2022; Accepted 22 July 2022; Published 13 September 2022

Academic Editor: Adam Khan M

Different semiconductor materials have been used for the fabrication of PIN diodes such as Si, Ge, GaAs, SiC-3C, SiC-4H, and InAs. These different semiconductor materials show different characteristics and advantages such as SiC-4H is ultrafast switch. But, when flexible polymers composites like Si-nanomembranes, polyethylene terephthalate (PET), and biodegradable polymer composite like carbon nanotubes (CNT) are used for fabrication, the device has the capability to switch from rigid electronic devices to flexible and wearable electronic devices. These polymer composites' outstanding characteristics like conductivity, charge selectivity, flexibility, and lightweight make them eligible for their selection in fabrication process for wearable electronics devices. In this article, the performance of PIN diodes (BAR64-02) as an RF switch is investigated from 1 to 10 GHz. PIN diodes can control large amounts of RF power at very low DC voltage, implying their suitability for RF applications. In this paper, the benefit of using plastic polymer composites for the fabrication of PIN diodes, capacitors, and antennas is thoroughly described. Along with this, individual characterization, fabrication, and testing of all biasing components are also done to analyze the individual effect of each biasing component on the performance of PIN diodes. The complete biasing circuitry for the PIN diode is modeled in the HFSS software. When a PIN diode is inserted in between 50 Ω microstrip line, it introduces 1 dB insertion loss and 20 dB isolation loss from 1 to 7 GHz. Finally, a PIN diode is integrated in a reconfigurable antenna to study the actual effect. The transmission loss in the RF signal is nearly 1 dB from 1 to 7 GHz in the presence of biasing components.

1. Introduction

The exclusive properties and features of flexible electronics like high elasticity, durability, stability, being extremely lightweight, and the ability to be fabricated on rough surfaces make them a splendid aspirant for extensive applications. The areas of flexible electronics have been continuously advancing every single day, from new research in compatible materials to new procedures for fabricating such devices in alternative shapes, in a quicker, economical, and more handy manner [1–2]. Flexible electronics interact with surroundings in ways that were not possible earlier. Many consumer applications, including folding phones, rollable large-area displays, electronic textiles, biomedical sensors, and flexible integrated circuits, are only possible due to the advancement in fabrication techniques. These advanced fabrication processes introduce the ultra-downscaling capability of silicon [1–4], which convert rigid wafers into single-crystal Si-nanomembranes (SiNMs). Therefore, silicon attracts researchers' interest for its incorporation into flexible electronics area. The ultrathin and transferrable single-crystal Si can be easily released from SOI and easily integrated on plastic polymer substrate using an elastomer stamp [5–6]. A large number of semiconductor materials such as amorphous silicon, polycrystalline silicon, organics, and polymers have been used for low-frequency flexible electronics because they suffer low crystalline quality

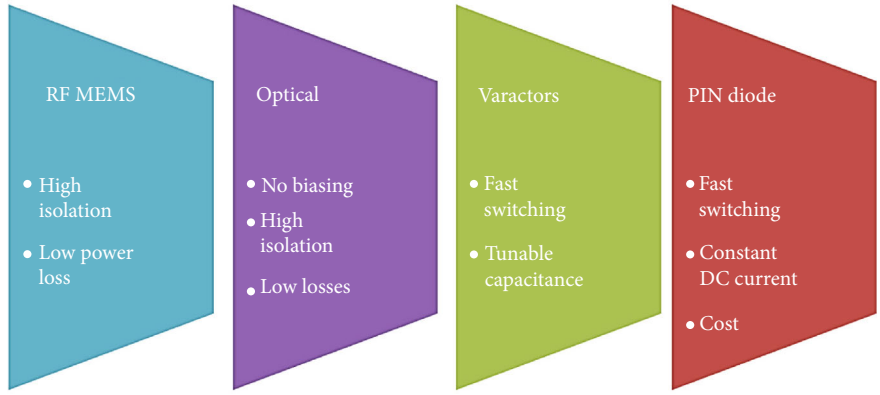

Figure 1: Performance comparison of various switches.

and low carrier mobilities. On the other hand, flexible low-cost polyethylene terephthalate (PET) substrates and single-crystal Si-nanomembranes (SiNMs) offer high carrier mobilities so these materials are well suited for microwave applications [5–8]. In the literature, a lot of flexible plastic substrates are available to realize flexible electronics like PET, polyethylene naphthalate (PEN), polycarbonate (PC), polyethersulfone (PES), and polyimide (PI). Nowadays, many compound semiconductors could also be released into thin membrane forms to attain mechanical flexibility while maintaining their outstanding electronic properties. Hence, semiconductor properties like high electron mobility (GaAs, InGaAs, InAs, GaN), wide bandgap (GaN), and high breakdown electric field (GaN) are maintained along with additional mechanical flexibility [9–12]. Many printing technologies have been already advanced like roll-to-roll, inkjet, screen-printing, vacuum-based deposition, and polydimethylsiloxane (PDMS)-assisted transfer printing techniques, which can transfer semiconductor properties on a plastic polymer substrate [10–17].

RF switches are key component for controlling the linking between different circuits in a reconfigurable device [18] at RF frequencies. A perfect RF switch provides negligible resistance in the ON state and very high resistance in the OFF state to the signal flow. However, practical RF switch provides definite values of impedance in the ON and OFF state. Several types of RF switches like MEMS, optical, and semiconductor are reported in the literature for altering the performance of a reconfigurable system [19–21]. All of these switches have certain advantages and drawbacks. The MEMS switching devices have the advantage of very high isolation with minimum power loss, but certain disadvantages such as high operating voltage (20–100 V), very low switching speed (1–200 seconds), high cost, and lower reliability restrict the use of MEMS switches [22–25]. The optical switches provide very high isolation and require no DC bias for their activation. They can be simply incorporated into a device without any DC bias lines hence eliminate redundant interference and radiation pattern alteration [26–28]. However, optical switches have lossy performance and very complex activation procedure. Various semiconductor switches like varactor [29–32], PIN are usually used in the reconfigurable system because they are a faster and more compact substitute to RF-MEMS [33–37]. The advantages of semiconductor switches include fast switching, high isolation, low power consumption, and low operating voltage (0–10 V). Different switches are selected depending on the suitable application. For example, a fast and discrete switching response requires PIN diode [34], while a continuous tuning response requires a varactor diode [31]. The PIN diode offers high switching speed (1–100 ns) and high isolation compared to other semiconductor switches. Reconfigurable antennas using PIN diodes [38–41] have more degrees of freedom in choosing different reconfiguration states. Researches can choose the appropriate switch for specific application by keeping the individual performance of switch in their mind. Figure 1 depicts an illustration that compares the different properties of the different switching mechanism for operation. PIN diode is best option among semiconductor switches if cost, switching speed, and isolation are concerned. If a microwave PIN diode is fabricated using a flexible material like SiNM and PET polymers, then high semiconductor performance can be achieved along with attractive mechanical features. In this paper, working operation and characterization of microwave PIN diode as an RF switch and different techniques and materials used to fabricate flexible PIN diode are presented.

2. PIN Diode: Preface

PIN diodes can be fabricated using different combinations of semiconductor materials like Ge and Si. If a wide-band-gap material is used for fabrication, then the PIN diode can handle high operating voltage as well as extreme temperature surroundings. SiC PIN diodes can handle high voltage and offer very high speed, whereas InGaAs on InP substrates give lower turn-on voltage for PIN diode. If a PIN diode is fabricated using an SOI substrate, then it gives high-voltage-handling capability and high reverse breakdown voltage. Also compound semiconductors have played crucial roles in high-frequency electronics because of their extraordinary material properties like high electron mobility (GaAs, InGaAs, InAs, GaN), wide bandgap (GaN), high breakdown electric field (GaN), and high thermal stability (GaN). These compound semiconductors can also be released into thin membrane forms to achieve mechanical elasticity while maintaining their electronic properties.

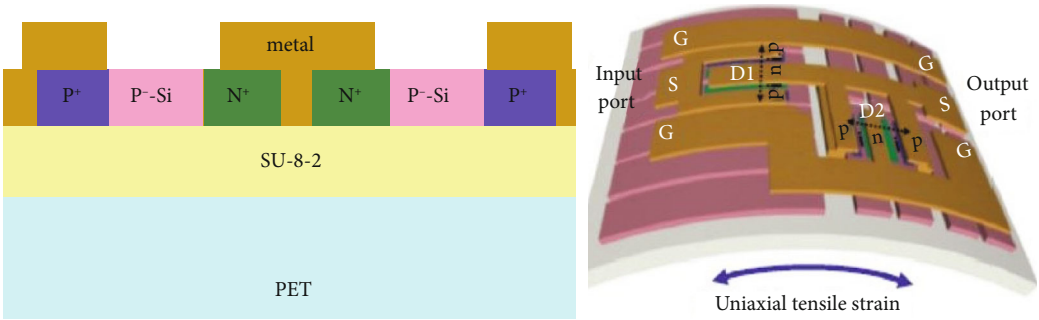

Figure 2: Schematic cross section of Si nanomembrane PIN diodes on a flexible PET substrate [12].

PIN diode can be fabricated using flexible single-crystal SiNM, which can be easily integrated on a low-cost plastic substrate for high performance [16–17]. The fabrication process of the flexible PIN diodes on a plastic substrate by using the SiNM transfer technique is entirely well matched with that used to fabricate flexible thin film transistors. The fabrication process starts with a lightly doped p-type Si (0 0 1) UNIBOND SOI substrate with a 200 nm Si top layer and a 200 nm buried oxide (BOX) layer. Optical photolithography is used to define the heavily doped n- and p-type regions in the top Si layer. The flexible single-crystal Si PIN diodes that are monolithically integrated on a low-cost, low-temperature, PET substrate [12] as shown in Figure 2. Flexible and stretchable passive components like inductors and capacitors are essential elements for RF filters, bias networks, power dividers, and impedance matching networks. Flexible inductors and capacitors can also be fabricated not only on plastic substrate but also on biodegradable carbon nanofiber (CNF) (polymer composite) substrates for environmental-friendly applications [10, 13]. The polymer composite CNFs gives excellent mechanical properties along with high electrical conductivity.

The semiconductor device PIN diode is used as an RF switch and its performance mainly depends on the layout, dimensions, and the temperament of the semiconductor material used in fabricated prototype. The sketch of a PIN diode is depicted in Figure 3. It is fabricated by inserting a wide region of intrinsic semiconductors among p-type and n-type semiconductors. In this, heavy doping of p- and n-type regions is done to get good ohmic contacts. On the other hand, the central I layer is lightly doped and wider in nature compared to p and n layers. Therefore, due to the wide I layer, PIN diodes have low junction capacitance, very high carrier lifetime and very high breakdown voltage. PIN diodes perform as switches due to the high-level injection. When the diode is in the OFF state, it is non-conductive. But when the PIN diode is in the ON state, high-level injection takes place and it behaves as a variable resistor. When it is forward-biased, the concentration of charge carrier in the p and n regions is higher than the intrinsic concentration in the I region. Therefore, E field expands on the whole length of the I region because of high-level injection. This extended E field increases the speed of transportation for charge carriers from p to n layers. As a consequence of this, the diode has faster operation and hence best suitable for high-speed RF applications.

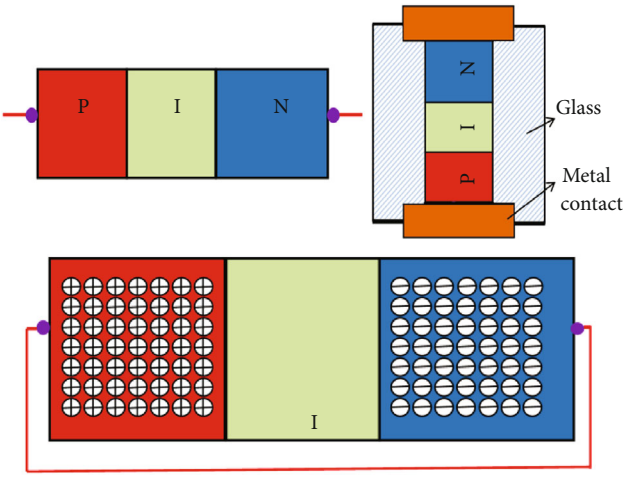

Figure 3: Layout of a basic PIN diode.

At low frequency, the PIN diode tracks the ordinary PN diode equation. Its *I-V* characteristic (Figure 4(a)) determines the forward voltage (V_F) and reverse voltage (V_R). At RF frequencies, during forward bias, the diode is ON for both positive and negative cycles. As in negative half cycle, the charge carriers in the I layer are not entirely cleared by the input signal, as there is not adequate time. Therefore, diode is continuously ON in the negative as well as positive RF cycle. When the diode is reverse-biased, very high impedance and low capacitance oppose the flow of RF signal. PIN diode acts as a current controlled resistor under forward bias conditions. Under this condition, equivalent model comprises of series combination of resistance (R_s) and a very low inductance (L) as shown in Figure 4(b). Under reverse bias, equivalent circuit of a PIN diode is shown in Figure 4(c), which comprises parallel connection of resistance (R_p) and capacitance (C_T).

3. Characterization of PIN as Switch

The low-cost silicon PIN diode is a powerful RF switch because it provides good return loss, high linearity, and high switching speed. The operating parameters that define PIN diode's switch characteristics are mainly insertion loss and isolation loss. The insertion loss is the amount of signal loss through the physical layout in the ON state, whereas

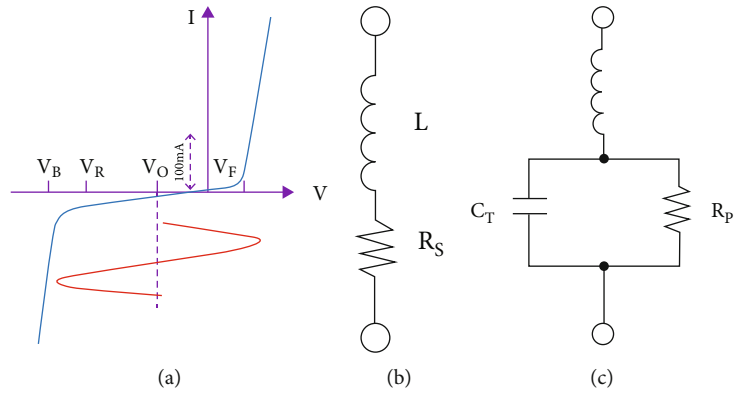

Figure 4: (a) *V-I* characteristic of PIN diode. (b, c) Equivalent model under forward and reverse bias.

isolation loss is the measure of how efficiently a switch is in OFF state. The biasing of PIN diode must be done precisely to get a good separation between DC power supply and RF signal. If proper biasing is not done RF current can flow in the DC biased signal, which degrades the effective operation of DC power supply. The DC signal can be easily separated from the RF signal by putting a series RF inductor and a shunt capacitor in the DC bias line. The equivalent model of Infineon diode is done in ADS software to study the actual effect of practical diode as shown in Figure 5. The insertion loss and isolation are calculated from equations (1) and (2). Under forward bias, the PIN diode is modeled as a series combination of resistance (2.1 Ω) and inductance (0.6 μH) as shown in Figure 5(b), and in reverse bias, it is modeled as a parallel combination of resistance (3 kΩ) and capacitance (0.17 pF) as shown in Figure 5(c).

$$\text{Insertion loss} = 20\log_{10}\left(1 + \frac{R_S}{2Z_0}\right). \quad (1)$$

$$\text{Isolation loss} = 10\log_{10}\left(1 + (4\pi f C Z_0)^{-2}\right). \quad (2)$$

From the simulated parameter, it is found that insertion loss is 0.1 dB from 1–8 GHz under switch in ON condition as shown in Figure 5(d). Also, it is observed that when diode is in switch OFF condition; insertion loss is better than 19 dB. Therefore, it shows very high impedance and there will be no transmission of signal from source to load. These are only simulated parameters, but when PIN diode is actually placed in a fabricated prototype, it encounters microstrip line, bias voltage, and bias lines. In this paper, PIN diode is used for closing or opening a connection between a microstrip lines. The PIN diode is properly biased using an SMD capacitor and an inductor. So first, the performance of a microstrip line is evaluated. Then characterization of RF inductor and RF capacitor is also done to study the amount of insertion loss introduced by them. To find out the response of these components, some prototype has been fabricated and tested successfully.

4. Performance Evaluation of Biasing Component

Fabrication of all prototypes is done on a $20 \times 20\,\text{mm}^2$ sized FR4 substrate using the MITS PCB prototyping machine. The relative dielectric constant of FR4 $\varepsilon_r = 4.4$, and the height is 1.57 mm. Here, Infineon BAR64-02 PIN diodes, Coil Craft Inductors, and Murata SMD Ceramic Capacitors are used during fabrication. The measurement of *S* parameters is done using an Agilent N5222A Vector Network Analyzer.

4.1. Microstrip Line (50 Ω) Structure. A 50 Ω transmission line is designed and tested here. The schematic for microstrip line, measurement setup, and the fabricated structure are revealed in Figure 6(a) and 6(b). The measured parameter of the microstrip line and E field distribution are shown in Figure 6(c) and 6(d). Ideally, the 50 Ω microstrip structure has 0 dB insertion loss, but actually insertion loss is not negligible. The simulated value of insertion loss is 0.5 dB over 1–10 GHz, whereas measured value of insertion loss is 0.1 dB from 1 to 6 GHz and 0.4 dB from 6 to 9 GHz.

4.2. RF Bypass Element: SMD Capacitor. A DC block capacitor plays a major role when the biasing components of PIN diode are designed. It is used to provide isolation between RF signal and DC signal. DC block capacitor also helps to isolate two or more different DC regions distinctly to bias more than two diodes independently. The value of RF bypass/DC Block capacitor is chosen to provide minimum impedance for RF signal and maximum impedance for DC signal. Ideally, DC blocking capacitor should behave as a short circuit at operating frequency. Usually $X_C = 1/\omega C = 1/2\pi f C$ should be less than 2 ohms at operating frequency. So, when a capacitor is positioned in between the 50-ohm line, the signal should bypass with least insertion loss. To find out the insertion loss of a 30 pF SMD multilayer capacitor; it is placed in 0.5 mm wide gap of 50-ohm transmission line as depicted in Figure 7. During HFSS simulation, a capacitor is modeled as 30 pF using lumped boundary condition. The proposed structure, measurement setup, and the fabricated prototype are shown in Figure 7(a) and 7(b). Simulated and measured S parameters and electric field distribution are shown in

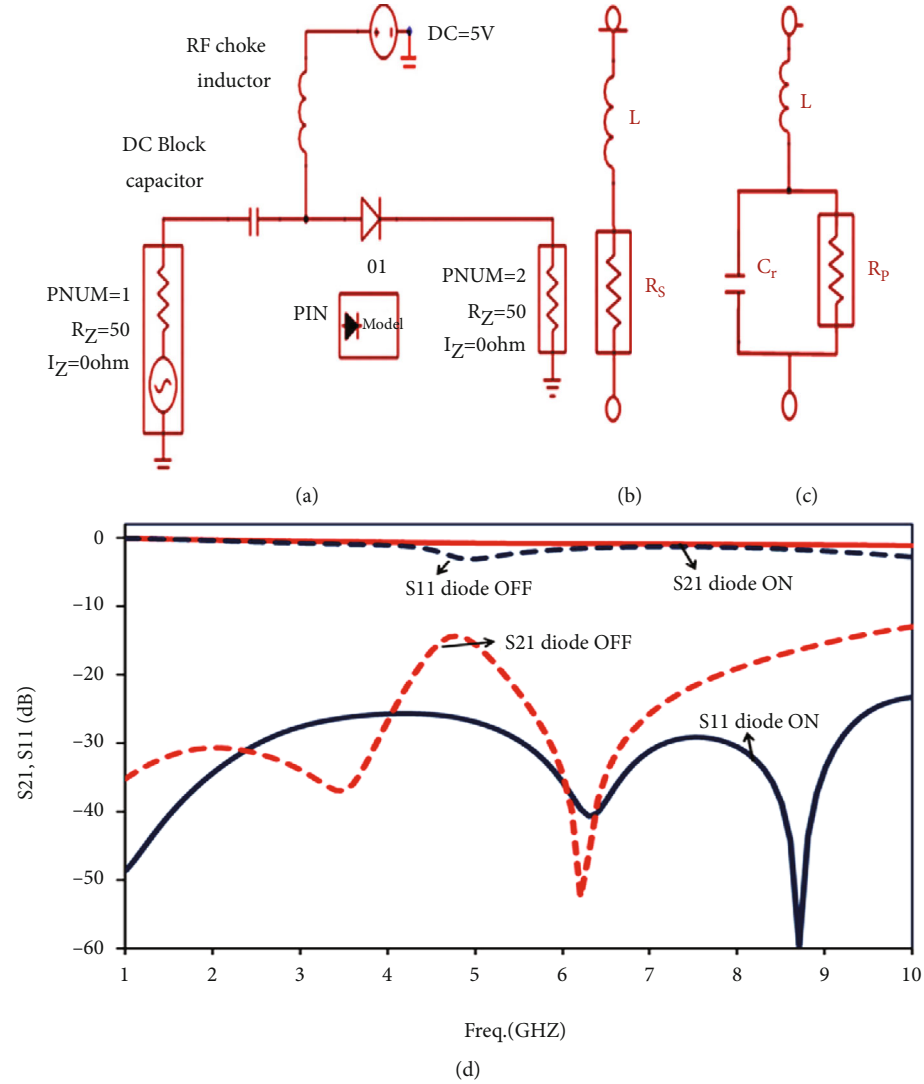

Figure 5: (a) The biasing circuit; (b, c) equivalent model in ON and OFF states; (d) S parameter vs. frequency.

Figure 7(c) and 7(d). Simulated value of S_{21} is 0.5 dB from 1–7 GHz whereas measured value is 0.2 dB from 1–7 GHz.

4.3. Testing of RF Choke Element: RF Inductor. The RF choke coil is designed for blocking or decoupling higher frequencies. RF choke coil provides large impedance to RF signal while minimum impedance to DC. Generally, the choke coil reactance $X_L = \omega L$ should be greater than 5 kΩ at operating frequency, where ω = angular frequency in Hz, L is the inductance measured in henry. As choking and blocking means providing high impedance to that signal. It is clear that we want to isolate the DC signal and the RF signal to reduce the interference. In this regards capacitor and inductor plays an important role. The values of both components are chosen so that they have least influence of RF and DC signals. Here inclusion of capacitors and inductor in a circuit are checked in the presence of DC power supply. For this, a prototype is designed and fabricated as shown in Figure 8(a) and 8(b). The layout consists of SMD capacitor of value 0.3 nF and inductor of value 0.3 uH. When DC signal is applied, the capacitor should bypass the RF signal and should offer very high impedance to the DC signal. The measured results shown in Figure 8(c) indicate that S_{21} is better than 2 dB and S_{11} is better than 13 dB from 1 to 7 GHz. The E filed distribution is given in Figure 8(d).

5. Performance of PIN Diode: An RF Switch

For the characterization PIN diode, a prototype has been fabricated and tested as depicted in Figure 9. For proper biasing, an Infineon BAR64-02 PIN diode, 2 RF inductors, and 2 SMD capacitors are used. When we apply +1.1 V on the DC pad, the diode is forward-biased. At this time, diode should offer very low impedance to the flow of RF signal, and hence S_{21} should be minimum. The results shown in Figure 10(a) indicate that S_{21} is better than 2.5 dB for 1–6.5 GHz. At the time of reverse bias, the diode should block RF by giving maximum impedance. The results shown in Figure 10(b) indicate that isolation loss is better than

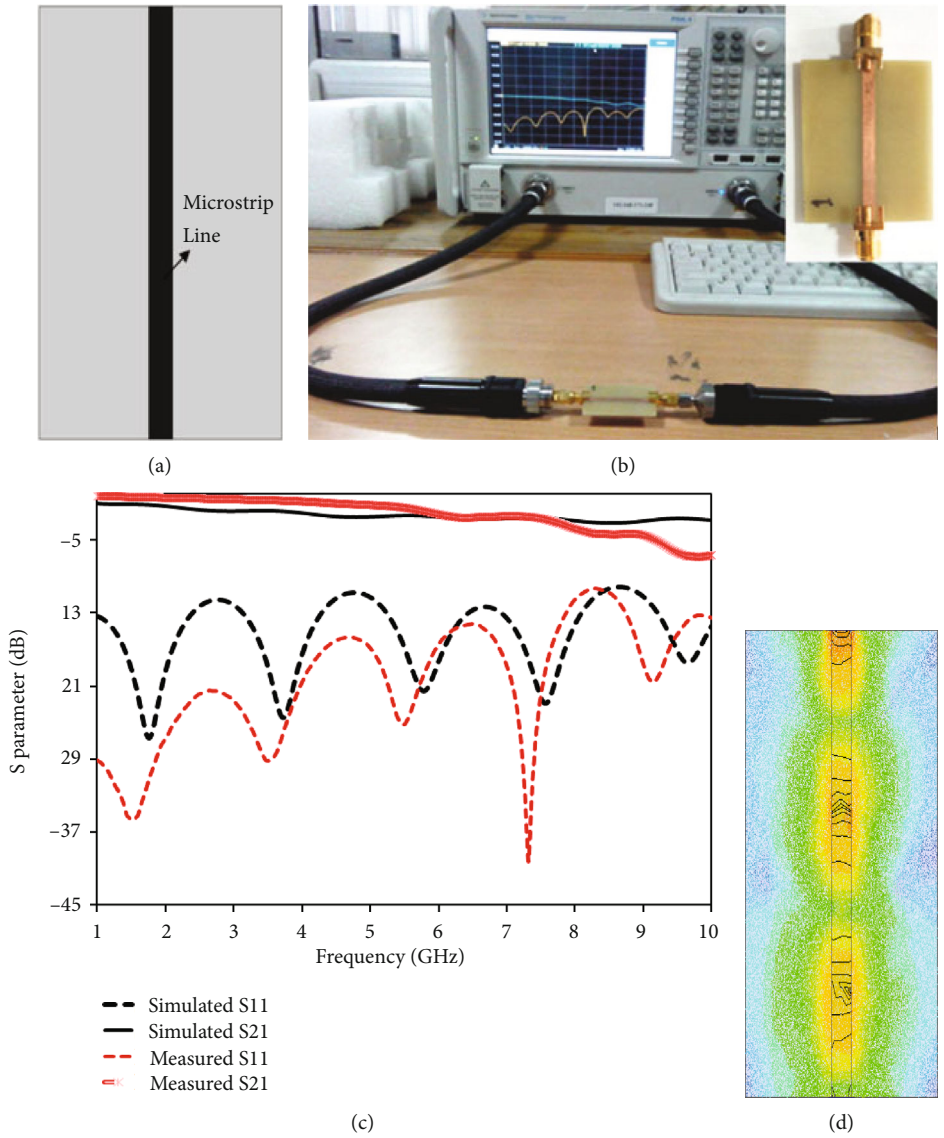

Figure 6: (a) Microstrip line; (b) measurement setup; (c) S parameter vs. frequency; (d) E field distribution.

18 dB. As S_{11} parameter gets distorted after 7 GHz, its operating bandwidth should not exceed after 7 GHz.

6. Implantation of PIN Diode in a Reconfigurable Antenna

Flexible antennas are fabricated on substrates such as Kapton, PET, and liquid crystal polymer (LCP) substrates. Dielectric constant and loss tangent are important material parameters to design low cost and compact flexible antenna for wearable devices. A reconfigurable antenna was designed and tested as shown in Figure 11. In the proposed antenna [38], a reconfigurable feeding structure is used to switch its operating bands among multiple narrow bands. Here, five PIN diodes are implanted in the feed structure to control different stub positions autonomously. The implantation of PIN diode into antenna structure offer very low insertion loss of 1 dB up to frequency 7 GHz. These unique features are beneficial for space and aviation applications compared with the current bulky and surface mounting antenna modules since they can minimize weight and drag-force during high-speed motion.

7. Conclusion

PIN diodes have been used as a microwave switch in a lot of microwave circuits. With the advancement in fabrication technology, we are shifting to flexible and wearable electronics. The flexible devices can be fabricated on such polymers, which not only have excellent electrical properties like high carrier mobilities, dielectric constant, and low loss tangent but also have excellent mechanical features like high elasticity, durability, stability, and being extremely lightweight. The flexible PIN diode can be fabricated not only on polymer substrate like PET, polyethylene naphthalate (PEN), polycarbonate (PC), polyethersulfone (PES), and polyimide

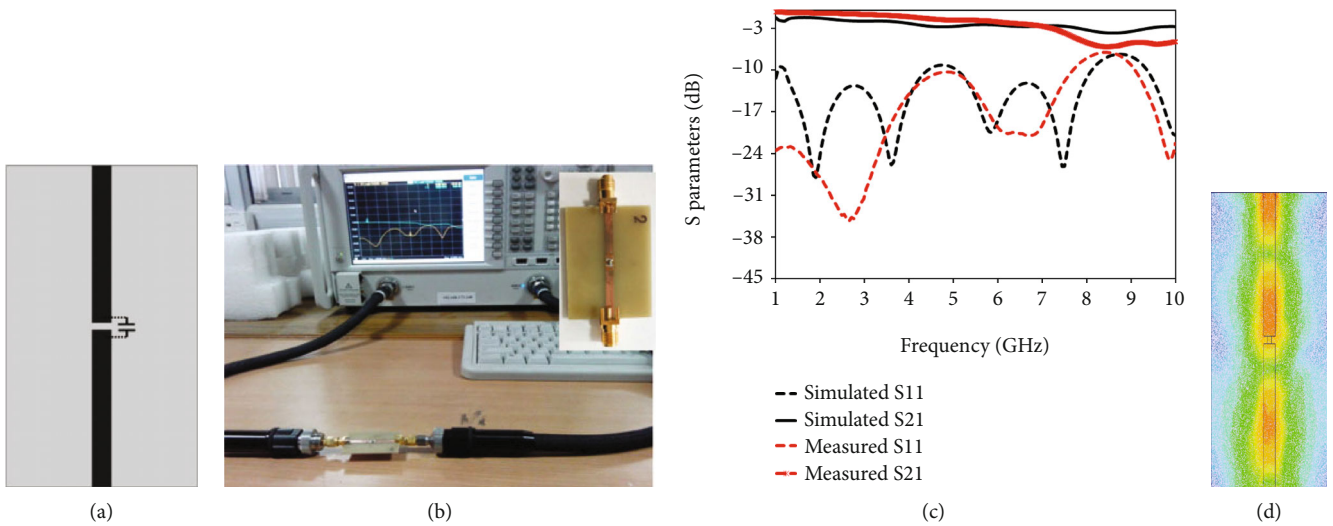

Figure 7: (a) Layout for RF bypass capacitor; (b) measurement setup; (c) S parameter vs. frequency; (d) field distribution.

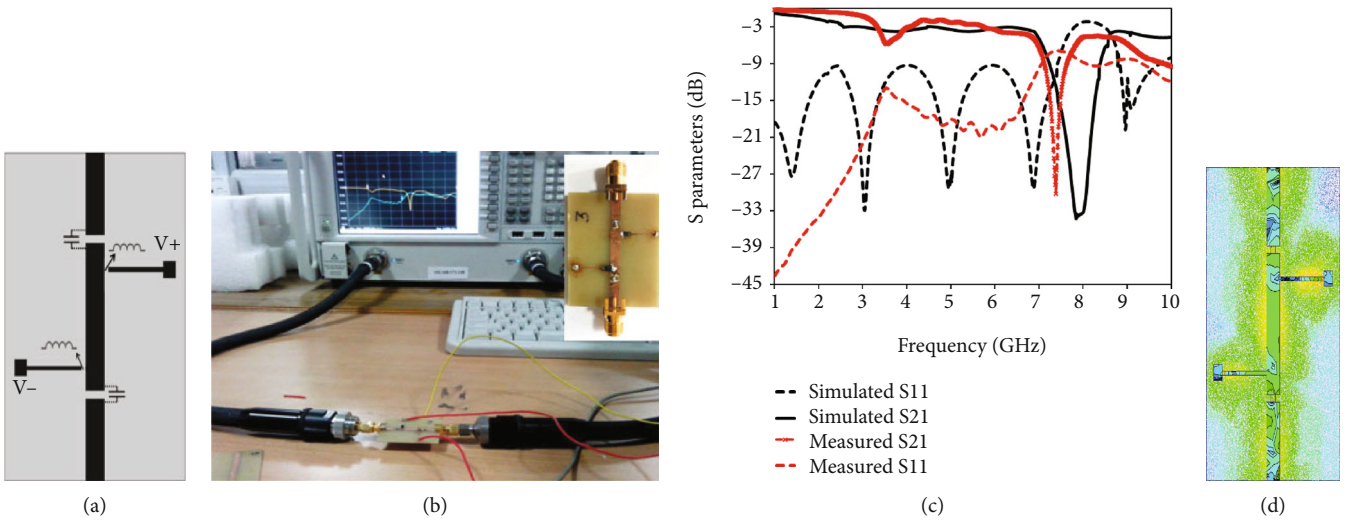

Figure 8: (a) RF choke under test; (b) measurement setup; (c) S parameter vs. frequency; (d) E field distribution.

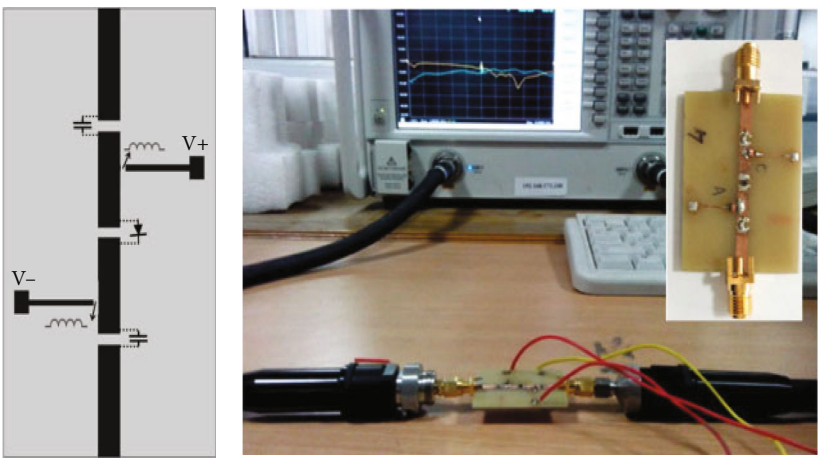

Figure 9: (a) Characterization of PIN diode; (b) experimental setup.

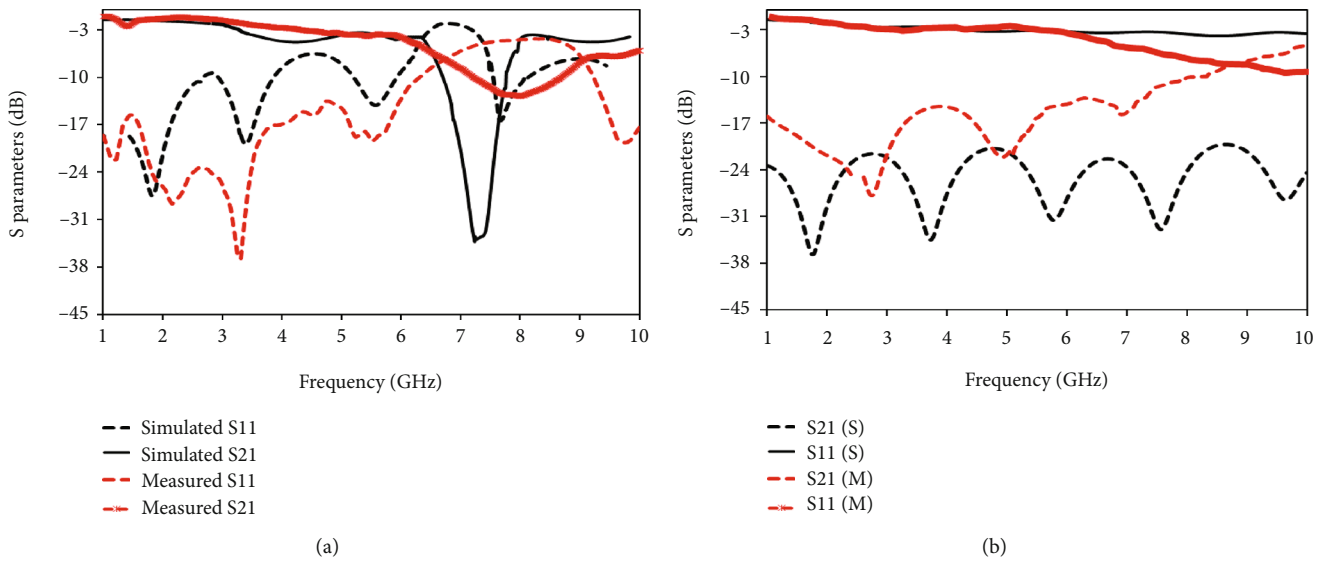

Figure 10: *S* parameter vs. frequency of PIN diode in (a) ON state and (b) OFF state.

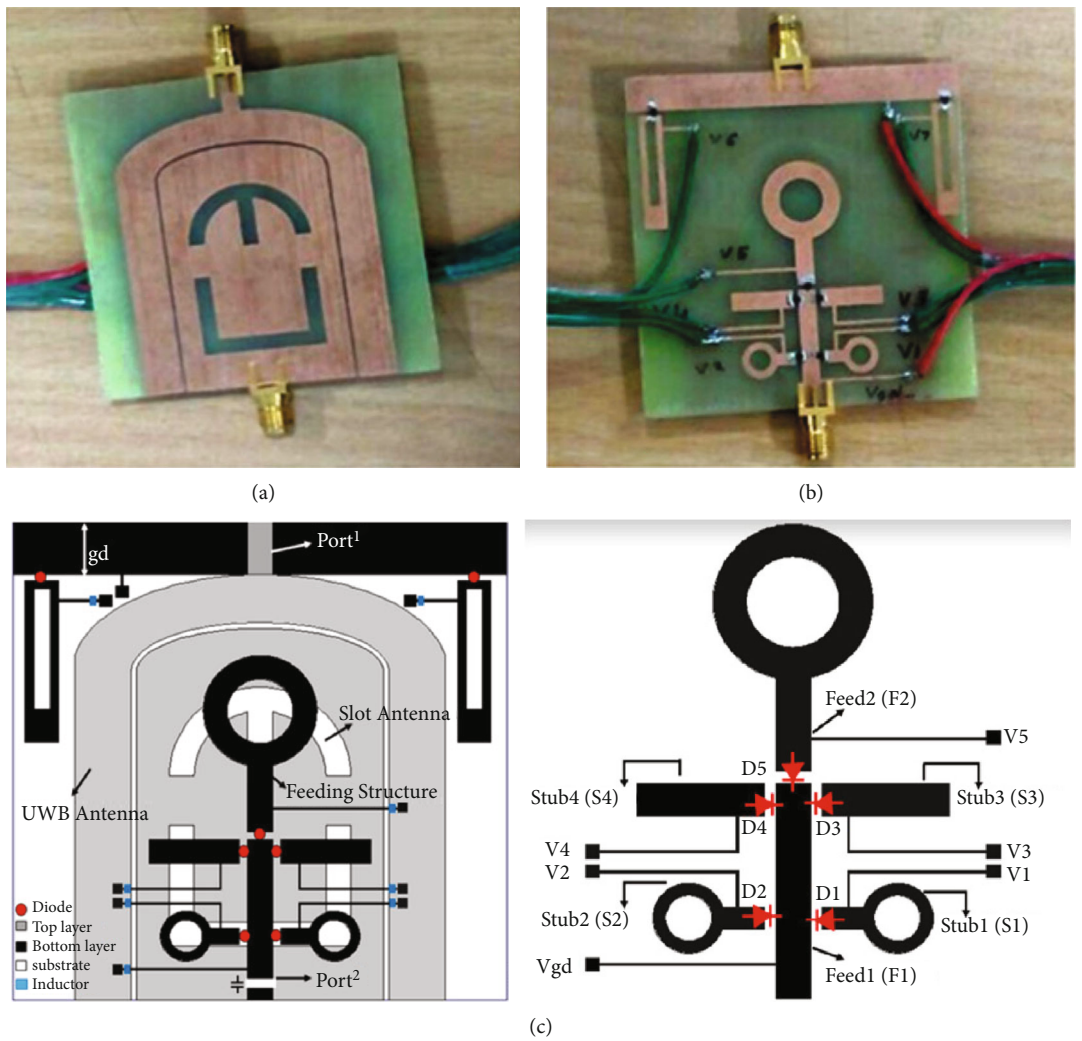

Figure 11: Fabricated layout of reconfigurable antenna using PIN diode: (a) top view; (b) bottom view; (c) measurement setup.

(PI), but also on biodegradable polymer composite carbon nanofiber CNF substrates for environmental-friendly small footprint applications. Some points need to be addressed during fabrication. The fabricated device should give low series resistance and capacitance in order to be able to achieve high-frequency operation. The polymer substrate material is chosen so that device should maintain its performance over repeated bending operations. The performance of PIN diode has been successfully investigated by testing a reconfigurable antenna. Each biasing component, i.e., SMD inductor, SMD capacitor, and PIN diode is implanted individually in the microstrip line structure to study the insertion and isolation loss. After fabrication of prototypes, measurement for transmission parameters was successfully done. It is concluded that the PIN diode is an ideal choice for high RF power applications because of high switching speed and low power dissipation. From the observed performance parameters of PIN diode, it is concluded that the transmission loss of RF signal is nearly 1 dB, and the isolation loss is better than 20 dB from 1 to 7 GHz in the presence of biasing components.

Conflicts of Interest

The authors declare that they have no conflicts of interest.

Authors' Contributions

S.S. and R.R.: Conceptualization and writing—original draft preparation; C.P. and D.B: methodology; K.K.S. and N.U.S: writing—review and editing.

References

[1] D. Corzo, G. Tostado-Blázquez, and D. Baran, "Flexible electronics: status, challenges and opportunities," *Frontiers in Electronics*, vol. 1, article 594003, 2020.

[2] R. Wei, X. Hua, and Z. Xiong, "Polymers and polymeric composites with electronic applications," *International Journal of Polymer Science*, vol. 2018, 2018.

[3] H. C. Yuan and Z. Ma, "Microwave thin-film transistors using Si nanomembranes on flexible polymer substrate," *Applied Physics Letters*, vol. 89, no. 21, article 212105, 2006.

[4] J. Bitenieks, R. M. Meri, J. Zicans, and K. Buks, "Dynamic mechanical, dielectrical, and rheological analysis of polyethylene terephthalate/carbon nanotube nanocomposites prepared by melt processing," *International Journal of Polymer Science*, vol. 2020, 7 pages, 2020.

[5] G. Qin, H.-C. Yuan, G. K. Celler, W. Zhou, and Z. Ma, "Flexible microwave PIN diodes and switches employing transferrable single-crystal Si nanomembranes on plastic substrates," *Journal of Physics D: Applied Physics*, vol. 42, no. 23, article 234006, 2009.

[6] H.-C. Yuan, Z. Ma, and G. K. Celler, "Flexible RF/microwave switch-PIN diodes using single-crystal Si-nanomembranes," in *2007 IEEE/MTT-S International Microwave Symposium*, pp. 1027–1030, IEEE, 2007.

[7] B. A. Alshammari, A. N. Wilkinson, and G. Almutairi, "Electrical, thermal, and morphological properties of poly(ethylene terephthalate)-graphite nanoplatelets nanocomposites," *International Journal of Polymer Science*, vol. 2017, 9 pages, 2017.

[8] O. Rodríguez-Uicab, A. May-Pat, F. Avilés, P. Toro, and M. Yazdani-Pedram, "Influence of processing method on the mechanical and electrical properties of MWCNT/PET composites," *Journal of Materials*, vol. 2013, Article ID 656372, 10 pages, 2013.

[9] S.-T. Schmitz-Hertzberg, R. Liese, C. Terjung, and F. F. Bier, "Towards a smart encapsulation system for small-sized electronic devices: a new approach," *International Journal of Polymer Science*, vol. 2014, 12 pages, 2014.

[10] A. Kaur, X. Yang, and P. Chahal, "CNTs and graphene-based diodes for microwave and millimeter-wave circuits on flexible substrates," *IEEE Transactions on Components, Packaging and Manufacturing Technology*, vol. 6, no. 12, pp. 1766–1775, 2016.

[11] J. Semple, D. G. Georgiadou, G. Wyatt-Moon, G. Gelinck, and T. D. Anthopoulos, "Flexible diodes for radio frequency (RF) electronics: a materials perspective," *Semiconductor Science and Technology*, vol. 32, no. 12, article 123002, 2017.

[12] G. Qin, H.-C. Yuan, Y. Qin et al., "Fabrication and characterization of flexible microwave single-crystal germanium nanomembrane diodes on a plastic substrate," *IEEE Electron Device Letters*, vol. 34, no. 2, pp. 160–162, 2013.

[13] Z. Spitalsky, D. Tasis, K. Papagelis, and C. Galiotis, "Carbon nanotube-polymer composites: chemistry, processing, mechanical and electrical properties," *Progress in Polymer Science*, vol. 35, no. 3, pp. 357–401, 2010.

[14] S. B. Aziz, M. H. Hamsan, M. F. Z. Kadir, and H. J. Woo, "Design of polymer blends based on chitosan: POZ with improved dielectric constant for application in polymer electrolytes and flexible electronics," *Advances in Polymer Technology*, vol. 2020, 2020.

[15] M. Shamsuyeva, O. Hansen, and H.-J. Endres, "Review on hybrid carbon/flax composites and their properties," *International Journal of Polymer Science*, vol. 2019, 17 pages, 2019.

[16] Iqra Masroor, Jamshed A. Ansari, Amrees Pandey, and Piyush K. Mishra, "Design and Analysis of Multiband Fractal Reconfigurable Antenna Using PIN Diodes for Smart Wireless Communications," *Progress In Electromagnetics Research C*, vol. 120, pp. 209–222, 2022.

[17] X. Yang, A. Kaur, and P. Chahal, "Embedded diodes for microwave and millimeter wave circuits," in *2014 IEEE 64th Electronic Components and Technology Conference (ECTC)*, pp. 2144–2150, IEEE, 2014.

[18] J. F. White, *Microwave Semiconductor Engineering*, J. F. White Publications, Massachusetts, 1995.

[19] S. Sharma and C. C. Tripathi, "Frequency reconfigurable U-slot antenna for SDR application," *Progress in Electromagnetics Research Letters*, vol. 55, pp. 129–136, 2015.

[20] A. Petosa, "An overview of tuning techniques for frequency-agile antennas," *Antennas and Propagation Magazine IEEE*, vol. 54, no. 5, pp. 271–296, 2012.

[21] C. L. Goldsmith, Z. Yao, S. Eshelman, and D. Denniston, "Performance of low-loss RF MEMS capacitive switches," *IEEE Microwave and Wireless Components Letters*, vol. 8, no. 8, pp. 269–271, 1998.

[22] H. S. Newman, J. L. Ebel, D. Judy, and J. Maciel, "Lifetime measurements on a high-reliability RF-MEMS contact switch," *IEEE Microwave and Wireless Components Letters*, vol. 18, no. 2, pp. 100–102, 2008.

[23] G. H. Huff and J. T. Bernhard, "Integration of packaged RF MEMS switches with radiation pattern reconfigurable square spiral microstrip antennas," *IEEE Transactions on Antennas and Propagation*, vol. 54, no. 2, pp. 464–469, 2006.

[24] C. Jung, M. Lee, G. P. Li, and F. D. Flaviis, "Reconfigurable scan-beam single-arm spiral antenna integrated with RF-MEMS switches," *IEEE Transactions on Antennas and Propagation*, vol. 54, no. 2, pp. 455–463, 2006.

[25] R. Kumar, "A review on RF micro-electro-mechanical-systems (MEMS) switch for radio frequency applications," *Microsystem Technologies*, vol. 27, no. 7, pp. 2525–2542, 2021.

[26] Y. Tawk, A. R. Albrecht, S. Hemmady, G. Balakrishnan, and C. G. Christodoulou, "Optically pumped frequency reconfigurable antenna design," *IEEE Antennas and Wireless Propagation Letters*, vol. 9, pp. 280–283, 2010.

[27] H. Sekiguchi, T. Kurahashi, L. Zhu, K. Kawaguchi, and K. Morito, "Compact and low power operation optical switch using silicon-germanium/silicon hetero-structure waveguide," *Optics Express*, vol. 20, no. 8, pp. 8949–8958, 2012.

[28] G. Jin, L. Li, W. Wang, and S. Liao, "A wideband polarization reconfigurable antenna based on optical switches and C-shaped radiator," *Microwave and Optical Technology Letters*, vol. 62, no. 6, pp. 2415–2422, 2020.

[29] A. Smida, A. Iqbal, M. Selmi, A. A. Althuwayb, and N. K. Mallat, "Varactor diode-based dual-band frequency tunable multiple-input multiple-output antenna," *International Journal of RF and Microwave Computer-Aided Engineering*, vol. 31, no. 2, article e22519, 2021.

[30] O. Se-Keon, H.-S. Yoon, and S.-O. Park, "A PIFA-type varactor-tunable slim antenna with a PIL patch feed for multiband applications," *IEEE Antennas and Propagation Letters*, vol. 6, pp. 103–105, 2007.

[31] M.-C. Tang, H. Wang, T. Deng, and R. W. Ziolkowski, "Compact planar ultrawideband antennas with continuously tunable, independent band-notched filters," *IEEE Transactions on Antennas and Propagation*, vol. 64, no. 8, pp. 3292–3301, 2016.

[32] N. Behdad and K. Sarabandi, "Dual-band reconfigurable antenna with a very wide tunability range," *IEEE Transactions on Antennas and Propagation*, vol. 54, no. 2, pp. 409–416, 2006.

[33] B. T. P. Madhav, P. Nadh, A. Kumar, P. Pardhasaradhi, M. C. Rao, and P. Lakshman, "Frequency reconfigurable Split ring antenna for LTE and WiMAX applications," *International Journal of Electronics and Telecommunications*, vol. 66, no. 2, pp. 255–260, 2020.

[34] C. C. Sonia Sharma and R. R. Tripathi, "A versatile reconfigurable antenna with integrated sensing mechanism," *International Journal of Microwave and Wireless Technology*, pp. 1–10, 2017.

[35] S. Sharma and C. C. Tripathi, "A wide Spectrum sensing and frequency reconfigurable antenna for cognitive radio," *Progress in Electromagnetics Research C*, vol. 67, pp. 11–20, 2016.

[36] S. Sharma and C. C. Tripathi, "Wideband to concurrent triband frequency reconfigurable microstrip patch antenna for wireless communication," *International Journal of Microwave and Wireless Technologies*, vol. 9, no. 4, pp. 915–922, 2019.

[37] A. A. Palsokar and S. L. Lahudkar, "Frequency and pattern reconfigurable rectangular patch antenna using single PIN diode," *AEU-International Journal of Electronics and Communications*, vol. 125, article 153370, 2020.

[38] S. Sharma and C. C. Tripathi, "An integrated frequency reconfigurable antenna for cognitive radio application," *Radioengineering*, vol. 26, no. 3, pp. 746–754, 2017.

[39] M. Kim, J.-G. Yang, and K. Yang, "Switched transmission-line type Q-band 4-bit MMIC phase shifter using InGaAs pin diodes," *Electronics Letters*, vol. 46, no. 3, pp. 219–220, 2010.

[40] S. Sharma and C. C. Tripathi, "A versatile reconfigurable antenna for cognitive radio," *Asia Pacific Microwave Conference, APMC-2016, 5–9 Dec. New Delhi, India*, 2016.

[41] S. Sharma and C. C. Tripathi, "A novel reconfigurable antenna with separate sensing mechanism for CR system," *Progress in Electromagnetics Research C*, vol. 72, pp. 187–196, 2017.

Hindawi
International Journal of Polymer Science
Volume 2022, Article ID 3963188, 12 pages
https://doi.org/10.1155/2022/3963188

Research Article

Design of Polymer-Based Trigate Nanoscale FinFET for the Implementation of Two-Stage Operational Amplifier

Jami Venkata Suman,[1] **Kusma Kumari Cheepurupalli**,[2] **and Haiter Lenin Allasi**[3]

[1]*Department of ECE, GMR Institute of Technology (Autonomous), Rajam, India*
[2]*Department of ECE, Gayatri Vidya Parishad College of Engineering (Autonomous), Visakhapatnam, India*
[3]*Department of Mechanical Engineering, WOLLO University, Kombolcha Institute of Technology, Kombolcha, Ethiopia Post Box No. 208*

Correspondence should be addressed to Jami Venkata Suman; venkatasuman.j@gmrit.edu.in
and Haiter Lenin Allasi; drahlenin@wu.edu.et

Received 24 June 2022; Accepted 8 July 2022; Published 28 July 2022

Academic Editor: JT Winowlin Jappes

The major motivation behind transistor scaling is the requirement for high-speed transistors with lower fabrication costs. When the fin thickness or breadth is smaller than 10 nm in a trigate FET, charges travel in a nonconfined fashion, resulting in the creation of energy subbands and causing volume inversion. In comparison to the carrier near a surface inversion layer, volume inversion experiences less interface scattering. In large-scale integrations, we have focused on developing a 3D model for surface potential by establishing the three-dimensional Poison's equation and building a unique fin field-effect transistor (FinFET) structure. In this context, there is a growing interest in developing a low-cost, simple solution that combines plastic (polymer) as a substrate and organic materials to create electronics such as monitors and sensors. The research examines characteristics such as silicon width, oxide thickness, doping concentration, metal work-function about gate, and various surface potentials. For different circuit configurations, it also examines the DC and AC characteristics of the FinFET structure. A differential amplifier is built for RF application based on the device specifications. This work is aimed at improving the semiconductor design structure by adjusting device parameters, analyzing the results, establishing the best FinFET device preferences, and selecting an application for the optimized device. The 3D Poisson's equation may be used to create an analytical model of a trigate nanosize FinFET, which can then be tested using a TCAD simulator. By constructing such a FinFET, we can structure and analyze various electrostatic parameters. To facilitate the creation of FinFET-based circuits, including product development, a novel transistor needs a creative device basis. The infrastructure's support denotes a computationally advantageous numerical model that accurately depicts a FinFET. The work presents a compact model for semiconductor manufacturing that permits separate IC productions while achieving higher levels of excellence and using less power. The design outperforms the CMOS by 22.7% in gain, 31.48% in power consumption, and 12.72% in CMRR, while operating at a 5 GHz unity gain frequency.

1. Introduction

Over the last few decades, integrated circuit manufacturers have steadily shortened the physical length of planar silicon metal-oxide-semiconductor field-effect transistors (MOSFET) to improve their power efficiency, speed, and manufacturing cost per transistor. As a result, an undesired impact known as the second-order effect has developed parallel. The leakage current and, as a result, the dissipation of the leakage (static) power are growing due to short channel effects (SCE) [1].

Traditional bulk MOSFET scaling is nearing its conclusion, not just because of manufacturing problems but also because further scaling would not lower power dissipation but would likely raise it dramatically. But then again, Dennard law of scaling still holds good. This law states that, as

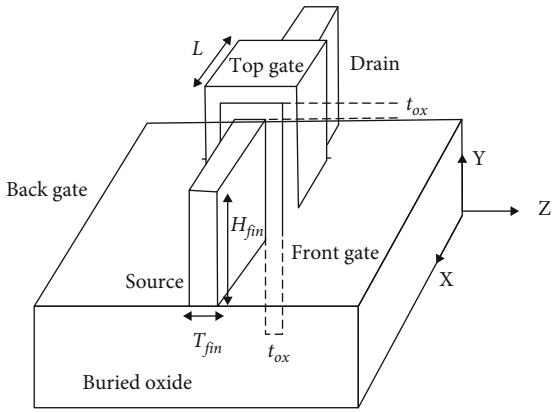

Figure 1: Structure of a basic 3D FinFET.

transistors get smaller, their power density stays constant, so that the power use stays in proportion with area, both voltage and current scale (downward) with length. On the other hand, leakage current poses a great challenge which leads to chip heat up and also leads to power dissipation. With currently available commercial microprocessors operating in the gigahertz range, shrinking the device's size also leads to an increase in operating frequencies [2]. The manufacture of complementary metal oxide semiconductors (CMOS) is now the industry standard. It is also the universal enabler of a staggering number of electronic credentials that have the potential to recast our daily lives [3]. Lower operating power, more performance, and lower standby power are the foundations for future technologies. High-performance logic is associated with significant, sophisticated integrated circuits that require high clock rates and low power consumption, such as a microprocessor system. Static leakage accounts for roughly half of the dissipated power with each chip when using traditional planar, bulk MOSFET scaling. Conventional bulk MOSFET scaling is nearing its conclusion, not only because of manufacturing problems but also because further scaling would significantly increase power dissipation [4–6]. When transistors are scaled down, a new generation of technology or node emerges. Deeper integration, lower energy consumption and higher performance are the parameters to be addressed when the devices are decided to scaled-down [7]. With currently available commercial microprocessors working in the gigahertz range, shrinking the device's size likewise boosts operating frequencies. As a result, every new generation of semiconductor technology streamlines circuit performance and power consumption, allowing the realization of increasingly complex systems [8].

Transistors are linked and correlated towards the top metal layers to attain output power outwardly. Apart from integrating, the connected transistors are used in differential common-source compensated amplifier steps. The neutralization capacitor improves the transistor's stability and maximum possible gain by utilizing the gate-to-drain capacitor's feedback effect. Unit cells were used in the design and a system MOM-cap for neutralization during the input, operator, and output stages. Self-heating due to the centre fins causes a microscopic unit-cell transistor to change quickly, and fingers are gently implanted, resulting in more dependable heat dissipation. Furthermore, the small transistors with quick fan-out to top metals allow adhering to the requisite electromigration criteria easy [9].

Because of the current decrease in MOSFET scaling, new technologies are absolutely necessary. There are two options for getting to the various approaches. The first is to create novel materials that have improved carrier transport characteristics. Second, the new transistor architectures (nonclassical multigate MOSFETs) with superior electrostatics and performance metrics allow for even more device scaling. In multigate, the current drive is determined by the total currents of the gate electrode interfaces if the carriers have equal mobility on all interfaces. Since charge sharing has ramifications inside the surrounding gates, premature inversion rises around the corners of SOI devices. Corner effects are fully parasitic in traditional single gate; however, in multigate, the corners are intrinsic transistors. To ease the creation of FinFET-based circuits, a novel transistor needs a creative device basis. The infrastructure's compliance denotes a computationally advantageous numerical model that accurately depicts a FinFET. A compressed model, on the other hand, is referred to as a spice standard. The paper presents a compact paradigm for semiconductor production that permits separate IC manufactures while achieving higher efficiency and using less power. The investigation's goal is to improve the semiconductor design structure by adjusting device parameters, studying the results, establishing the best FinFET device preferences, and selecting an application for the optimized device. Moreover, the methods for fabricating standard size circuits with SWCNTs (single-walled carbon nanotubes) and organic polymers are not compatible with manufacturing techniques like silicon-based semiconductors. Due to the absence of clearly identifiable on/off behavior, grapheme with polymer's almost zero band-gap semimetallic feature restricts its promise for electronic innovations, making it more ideal for radio-frequency (RF) applications with FinFETs [10, 11].

The objectives of this paper are to (i) examine and evaluate the usability of standard electron transport models used in commercial TCAD simulators for modelling the behavior of nanoscale channel lengths, (ii) develop an analytical model of a trigate nanoscale FinFET using 3-D Poisson's equation, (iii) evaluate the result using a TCAD simulator, and (iv) construct analog/RF circuits with FinFETs that have the best device characteristics and compare their performance to CMOS Analog Circuit Design.

2. Related Works

A 30 nm SOI FinFET Berkeley short-channel IGFET and conventional multigate architecture for OP-Amp design are proposed in [12]. To achieve compactness and lower power consumption in sensor and biomedical applications, researchers used a study technique against subthreshold control using FinFET developed OTA. It denoted, examined, and reasoned that OTA gain is independent of current in the weak inversion region; however, it is dependent in the vital

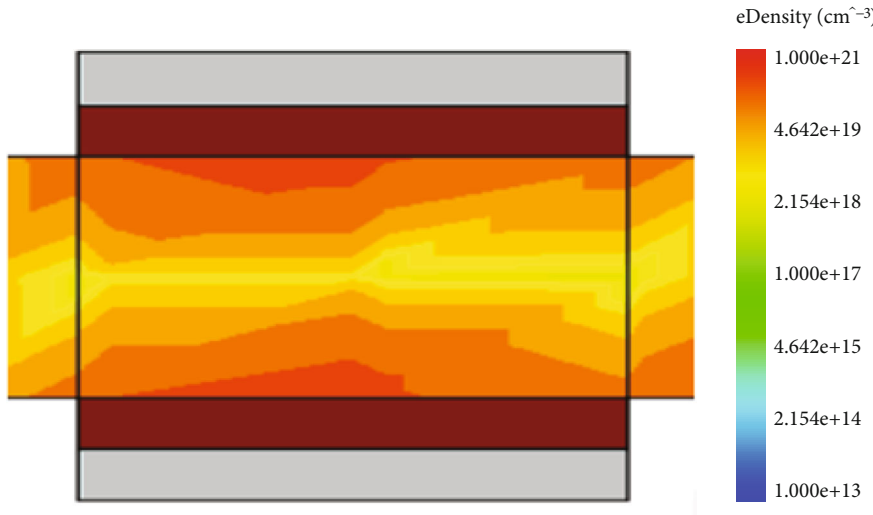

Figure 2: Electrostatic potential within the channel.

inversion region. Thanks to the compensation capacitor, the unity gain margin and slew rate have improved. A sophisticated electrostatic channel potential mathematical model to analyze lightly doped multigate FinFETs and debated how the larger k dielectric material affects the SCE is introduced in [13]. A subthreshold surface potential analytical modeling and the threshold voltage and subthreshold swing using a triple material trigate FinFET are proposed in [14].

In contrast to TCAD simulated outcomes, analytical model validation is obtained and proved to be more precise. The inherent advantages of applying the source side (dual-kS) and drain side (dual-kD) alone to boost these analog/RF figures of merit (FOM) toward low power performance at a channel length of 20 nm are discussed in [15]. The results show that a FinFET device with a dual-k spacer (inside spacer high k) boosts specific gate fringe field coupling across a specified underlap area on the source side. A bulk FinFET structure with high k spacer Si_3N_4 and low k spacer SiO_2 with a gate length of less than 10 nm is proposed in [16]. The device's DC and AC performances are examined and compared, revealing that spacer material increases the parasitic capacitance and delays through device scaling. The impact of HFin and WFin modifications on various performance indicators is discussed in [17]. Static and dynamic figures of merit (FOM) and specific DC and AC FOMs are all included. Because cut-off frequency (f_T), gate capacitance (C_g), inherent delay, and output resistance (R_O) are offered regularly by the adjustment concerning device geometry guideline, the fixed or low-frequency concerts plus active or high-frequency enforcement are presented constantly. The findings can aid designers in creating 3-D designs that are practically tailored to their needs.

A quantum model of the trigate n-FinFET device using the Bohm quantum potential framework is proposed in [18]. This included quantum confinement effects during specific simulations. Substantial scaling capabilities of FinFET transistors were examined, and the channel length was calculated conservatively. Short channel effects may be achieved by simply altering fin width and gate work function. This research demonstrates that the n-FinFET in the presence of ZrO_2 is a viable device for the CMOS industry's future. The study underlines the importance of doping level in determining the electrical properties of a FinFET channel. Designed an inverted T (IT) FinFET structure and discovered that a fin width (WFin) of less than 10 nm is required for robust gate controllability; otherwise, punch through occurs. Although the resistance to short-channel impact is significantly lower than that of SOI FinFET at significantly scaled L_g, an ideally outlined IT FinFET may deliver a higher current and confirm reduced intrinsic delay discussed in [19]. The Junction less inverted T-shaped gate FET construction and found that I_{ON} rose as channel capacity and fin width grew, and thin thickness suffered greater degradation in threshold voltage. With the same ITSB width, the significant height of fins is required to withstand SCEs and reduce threshold voltage deterioration as channel length decreases proposed in [20].

The transistor's external resistance (R_{ext}) is aggressively affected by the extension doping indicated during a specific inclination of the epitaxial expanded S/D. The continued doping orientation varies across external resistance for various threshold voltage (V_{th}) models, including ultralow V_{th}, low V_{th}, ordinary V_{th}, and variable transistor supply voltages (V_{dd}). The channel's electrostatic gate switch is represented as a subthreshold swing (SS_{sat}) with a high drain voltage (V_d). Some SS_{sat} for peak I_{eff} declines with enormous V_{th} essence, including a strategy for FinFET evolution on the scaling domain and a more moderate operation V_{dd} well discussed in [21]. FinFET devices at 14 nm technology node dimensions with and without LDD insertion are proposed in [22]. The V_{tsat} discrepancy between n-MOSFET transistors in neither LDD should drop by 20% if HCI's incorporated design authenticity connected with components among LDD is taken into account. The results show that, in addition to no LDD, FinFET architecture with a more constrained mask delivers greater cost-effectiveness, exciting accomplishment, and area scalability than designs with LDD as major performance and lower power systems.

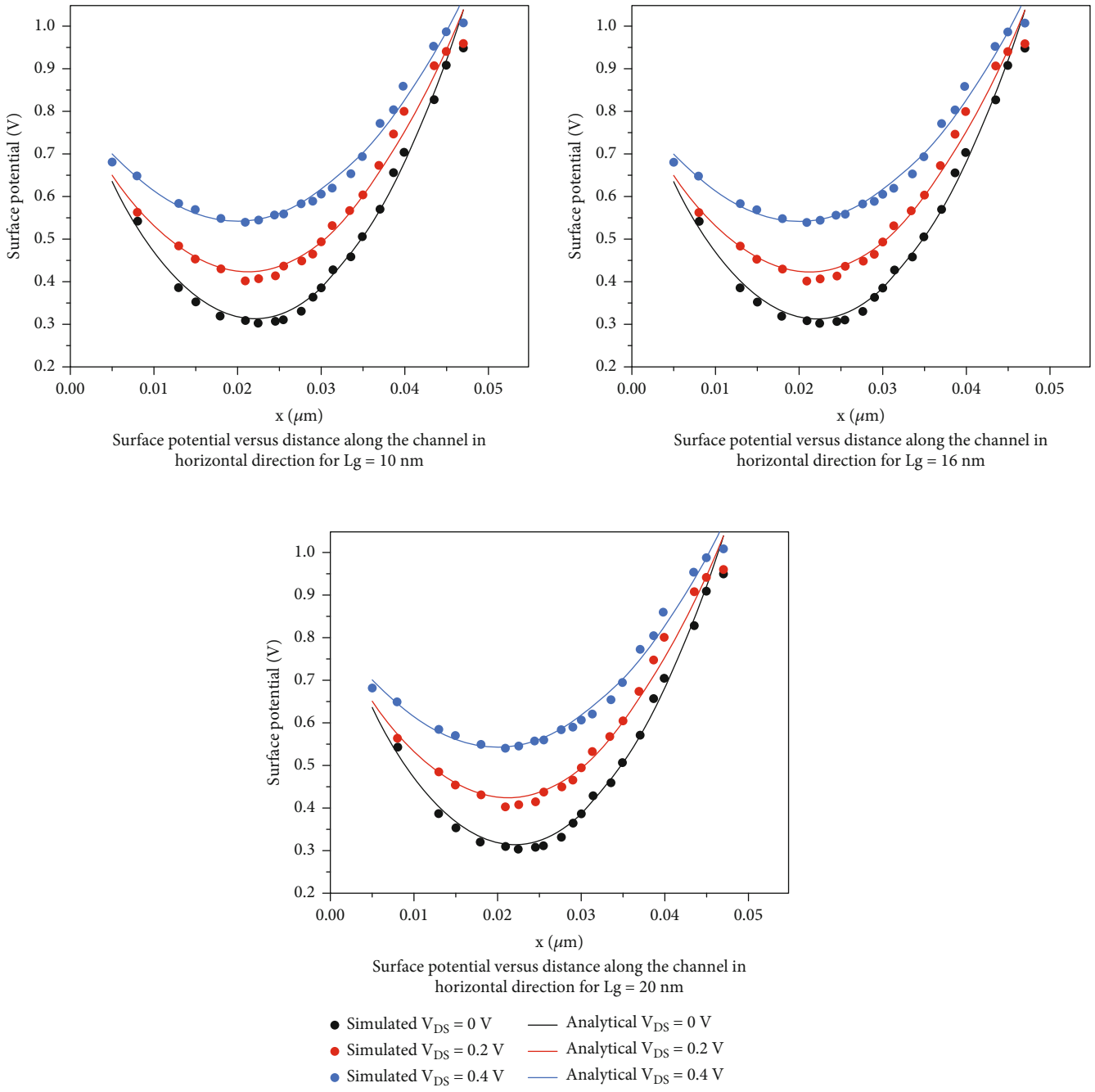

Figure 3: Surface potential vs. distance along the horizontal channel.

Totally depleting dual-material double-gate (DMDG) MOSFET as a surface potential 2D model is proposed in [23]. This model takes into account the effect of temperature as well as the impression of interface charge density. This model has also taken into account the effects of a large dielectric constant element like HfO_2, predicting that the surface potential on this channel will play a step role that will exceed multiple SCE. As a consequence, the model specifies that the oxide thickness using HfO_2 should be larger than SiO_2 in order to perceive this associated estimation regarding surface potential. Drain current and surface potential models for a physical-based double halo MOSFET in the subthreshold regime are introduced in [24]. Margins with unequal doping were used to regulate the depletion layer extent against pseudo-two-dimensional Poisson's equation. By monitoring each surface potential and draining current models, this classic silicon-dioxide (SiO_2) balances among a dielectric, hafnium oxide (HfO_2).

Because of the complexity associated with transistor scaling down and the emergence of new carrier transport mechanics, standard models can no longer be utilized to simulate such nanoscale devices, as stated above. As a result, particular care should be taken in selecting the appropriate simulation model. In this paper, we have focused on

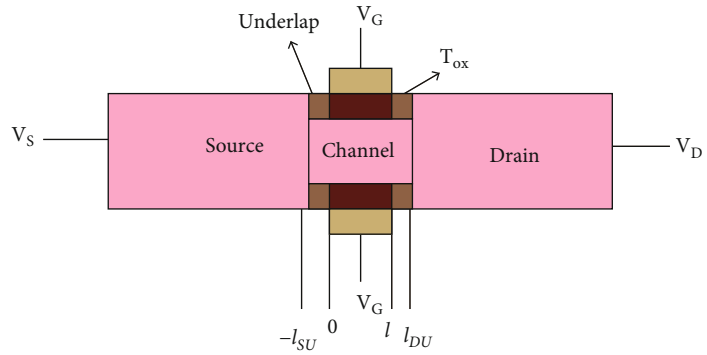

Figure 4: Two-dimensional underlap FinFET structure.

developing a 3D model for surface potential by establishing the three-dimensional Poison's equation and building a unique fin field-effect transistor (FinFET) structure. Further we proposed two-stage operational amplifier for RF application based on the device specifications.

3. Trigate Nanoscale FinFET

The fundamental impetus for transistor scaling is the need for high-speed transistors with lower fabrication costs. This decrease in transistor size or length shrinks circuits, increasing the number of transistors on integrated circuits. Due to the current lack of MOSFET scalability, novel technologies or methodologies are required. There are two options for getting to the various methods: creating a novel material with improved carrier transport properties. Second, the new transistor architectures (nonclassical multigate MOSFETs) with superior electrostatics and performance metrics allow even more device scaling. In multigate, the current drive is determined by the total currents of the gate electrode interfaces if the carriers have equal mobility on all interfaces.

In a trigate FET with a fin thickness or width less than 10 nm, charges can pass in a nonconfined way, resulting in the creation of energy subbands, which causes volume inversion. Compared to the carrier near a surface inversion layer, volume inversion experiences less interface scattering. As a result, the multigate structure has improved mobility and transconductance. Calculating and virtually implementing the channel charge density through a particular representation can result in a simple and compact mathematical model for trigate FinFET, as illustrated in Figure 1. Without interfering with the mobile charge densities at the source and drain, the model expression's drain current can be expressed. It is simple to derive a well-matching mathematical and corresponding 3D mathematical simulation. Through compressed modeling, a mobile deterioration that is expected across velocity overshoots and the scattering mechanism that is part of SCE can be constructed as an outspread version.

The analytical model of trigate FinFET is derived from the solution of Poisson's equation, which implies a little doping concentration in the channel. Due to the strong nonlinearity of the equation across the short channel, the perturbation approach is employed to compute the channel potential based on the three-dimensional Laplace solution. An electrostatic potential expression is retrieved from FinFETs in a doped channel area, recognizing relevant boundary limitations. The three-dimensional Poisson equation has been solved analytically; using the technique of splitting variables about the boundary stands to realize the 3D channel's potential. It is not possible to make fractions of fins due to quantized device width. Therefore, designers can only define the dimensions of the devices in multiples of complete fins. The entire fin area is considered analogous to calculate and formulate the effective silicon fin height (H_{eff}) and effective silicon fin thickness (T_{eff}).

$$T_{\text{eff}} = T_{\text{fin}} + \left(\frac{2S_{\text{si}}}{S_{\text{ox}}}\right) T_{\text{ox}},$$
$$H_{\text{eff}} = H_{\text{fin}} + \left(\frac{S_{\text{si}}}{S_{\text{ox}}}\right) T_{\text{ox}}, \quad (1)$$

where S_{si} is silicon dielectric permittivity and S_{ox} is the dielectric permittivity of SiO_2. The summation of the channel potential due to top (ψ_{tg}), front (ψ_{fg}), and back gates (ψ_{bg}); source (ψ_{s}); and drain (ψ_{d}) expresses the 3D surface channel potential function (ψ_{3D}):

$$\psi_{3\text{D}} = \psi_{\text{tg}} + \psi_{\text{fg}} + \psi_{\text{bg}} + \psi_{\text{s}} + \psi_{\text{d}}. \quad (2)$$

To validate the analytical model, the 3-dimensional simulator device "Sentaurus TCAD" was utilized to examine the potential surface distribution inside thin-film silicon. We used $V_{\text{sub}} = 0\,\text{V}$, $N_A = 11020\,\text{cm}^3$, $t_{\text{ox}} = 1.5\,\text{nm}$, $V_{\text{ds}} = 0.5\,\text{V}$, and $\varphi M = 4.7\,\text{eV}$ to calculate the surface potential along the channel. Here, $V_{\text{sub}} = 0\,\text{V}$ is used, and the charge density $Q_0 = 0$ is used. The electrostatic potential along the channel is illustrated in Figure 2.

The computed and simulated surface potential values for channel lengths of 10, 16, and 20 nm are graphed in the x -direction with a horizontal distance along the channel. At a fixed drain voltage of 0.4 V_{ds}, the electrostatic charge density increases as the channel X direction is changed. Given that the threshold voltage is determined by the minimal level surface potential near the source junction, it is easier to forecast the proper threshold voltage range for the trigate

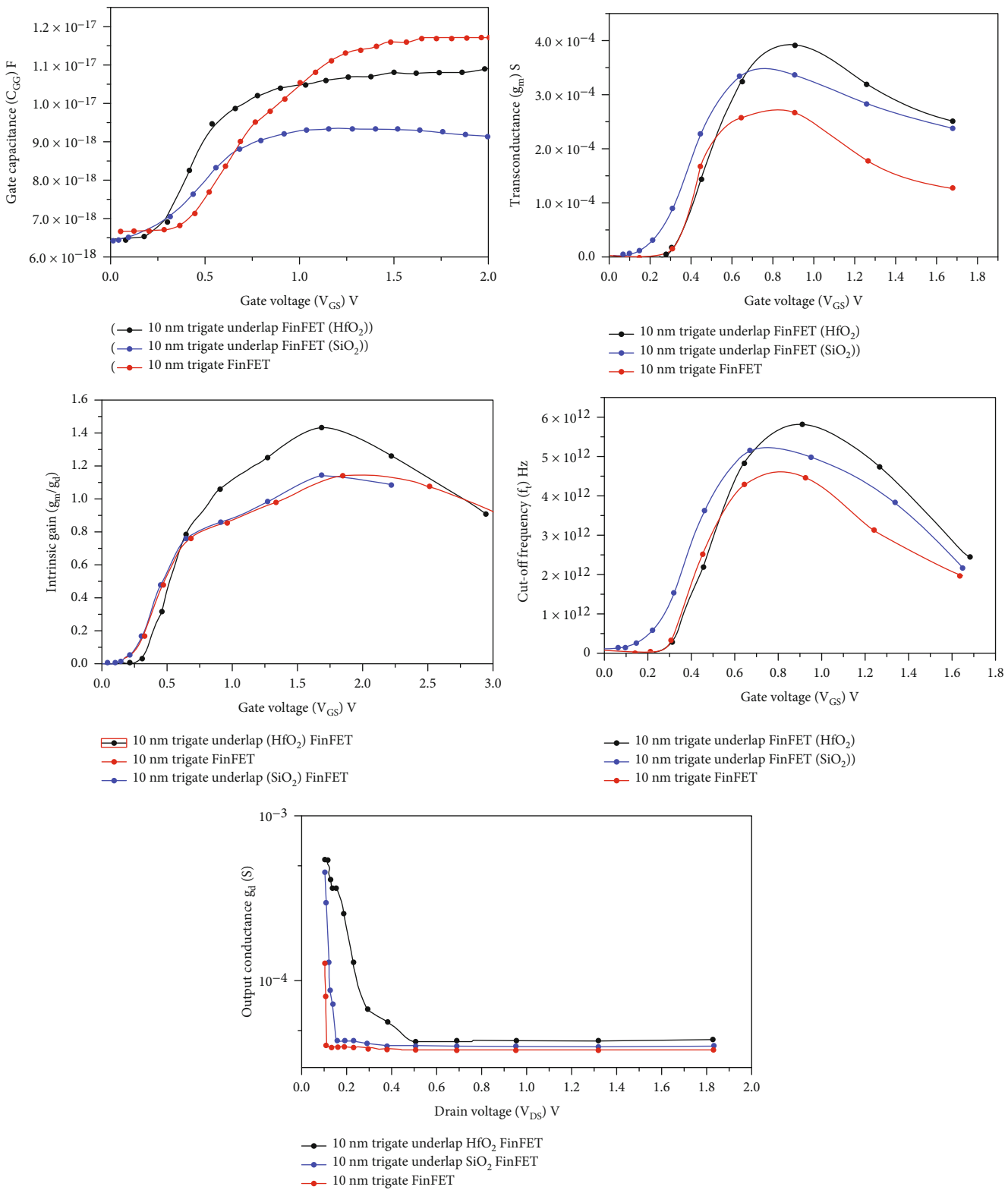

Figure 5: Performance analysis of the FinFET.

FinFET device. The device's performance is slowed by a high threshold voltage, whereas a lower threshold voltage tends to increase the OFF-state leakage current as illustrated in Figure 3. FinFET of 10 nm will have enough electrostatic control because of sufficient gate length which provides good electrostatic control. But beyond 5 nm, it will not have enough electrostatic control.

Quantum mechanical (QM) confinement occurs across the channel of charge carriers in FinFET devices with a very thin fin thickness (10 nm). Both structural and electrical

Table 1: Comparison of analog performance parameters for *n*-type 10 nm FinFET device.

Parameter	Ref. [29]	10 nm FinFET	Proposed trigate underlap (HfO_2) FinFET	Proposed trigate underlap (SiO_2) FinFET
Transconductance (μS)	352	262	390	315
Output conductance e(S)	7.54×10^{-4}	2.84×10^{-3}	8.37×10^{-4}	7.84×10^{-4}
Intrinsic gain (A_{VO})	1.09	1.07	1.4	1.02
Parasitic gate capacitance (F)	1.04×10^{-15}	1.18×10^{-17}	1.05×10^{-17}	0.85×10^{-17}
Cut-off frequency (THz)	0.05390	3.54	5.92	5.90

Table 2: Analog performance parameters towards *n*-type 16 nm SOI FinFET structure.

Parameter	Bias condition	*n*-FinFET
ON current (I_{ON})	$V_{ds} = 0.4$ V	334 (μA/μm)
OFF current (I_{OFF})	$V_{ds} = 0.4$ V	3.19*E*-6 (μA/μm)
Transconductance	$V_{ds} = 0.4$ V	408.2 μS
Threshold voltage	$V_{ds} = 0.4$ V	0.29 V
Subthreshold slope	$V_{ds} = 0.4$ V	77.6 mV/decade
Output resistance	$V_{ds} = 0.4$ V	1.92×10^5 Ω
Intrinsic gain	$V_{ds} = 0.4$ V	1.6
Parasitic gate capacitance	$V_{ds} = 0.4$ V	1.1×10^{-17} F

confinement show the source of these confined carriers [25]. The threshold voltage varies in response to the influence of QM (V_{th}, QM), which may be measured as a function of the carrier's effective mass to free-electron mass as well as the thickness of the silicon film in the confinement direction [26]. When the drain-source voltage V_d is increased beyond the saturation voltage $V_{dsat} = V_g - V_t$, a pinch-off occurs in the channel travelling from the drain to the source. This effect, referred to as channel length modulation (CLM), causes the channel to be slightly shorter than its physical length L [27].

$$L^{\iota} = L - \Delta L, \tag{3}$$

where L' is the gate electrical length due to drain-source voltage V_d and ΔL relates to the difference between L and the pinch-off. λ_{eff} is the effective natural length of trigate FinFET.

$$\Delta L = \lambda_{eff}\, V_{dpinch}. \tag{4}$$

Calculating the channel charge density, which is essentially a specific representation originating from the whole surface and core potential models yields a concise mathematical model for trigate FinFETs. The mobile charge densities at the source and drain are used to create the drain current expression. The mathematically modeled components and the three-dimensional mathematical simulations are well-matched. The compressed model is an outspread design that considers SCE, such as mobility loss due to scattering mechanisms, velocity overshoot, and quantum effects.

FinFETs are widely regarded as the most effective way to achieve higher OFF-state leakage current (I_{OFF}) and drain-induced barrier lowering (DIBL). FinFET technology is widely used in both analogue and digital circuit applications. FOM analogue, transconductance, early voltage, intrinsic DC gain, output conductance, and cut-off frequency are all affected by SCE. It also depends on the gate's influence on electrostatic integrity (EI) in the channel region. Practically, FinFETs are not completely robust to short channel effects but FinFETs have ability to mitigate the short channel effects because FinFETs contain gate all around the fin architecture which gives complete control to gate over the channel which reduces the short channel effects. But the channel control becomes difficult in FinFET. Even though underlap FinFET has a series parasitic rise, downscaling the structure aids in analogue realization. Underlap creation in FinFET structures may limit source-drain junction misalignment and improve SCE immunity.

The electrostatic integration (EI) of the underlap FinFET is superior, and its performance is less immune to interdevice variability and parametric fluctuations [28]. The barrier near the underlap lengths of FinFET is accentuated by spacers in the underlap FinFET as illustrated in Figure 4. The primary reason of the barrier changes is an extension of the gate fringing field, which moves the lateral electric field toward the drain. By increasing intrinsic DC gain, this electric field shift improves transconductance (g_m) while degrading output conductance (g_d).

Because of the lateral electric field swing between the gate edge and the drain, the underlap zone improves gate control by reducing SCE. Analog FOM is considerably enhanced, along with cut-off frequency (f_t), Transconductance (g_m), early voltage ($V_{EA} = I_{ds}/g_d$), and intrinsic DC gain (A_{VO}) [29]. By comparing and plotting the different features of a FinFET, we can analyze the analogous performance for different spacers as illustrated in Figure 5.

HfO_2 and SiO_2 as spacers are used to evaluate the performance of trigate FinFET and underlap trigate. When compared to trigate FinFET without underlap, underlap FinFET has a better overall performance. The underlap trigate FinFET with HfO_2 as a spacer, in particular, overcomes the SCEs with a 14.20% increase in g_m and a 28.44% increase in intrinsic gain, as well as a 5.9 THz cut-off frequency. In the inversion zone, the results show a noticeable linear increase. Because of the improved g_m and cut-off frequency properties, this device compares favorably to regular FinFETs shown in Table 1. It is also well suited for analog/RF

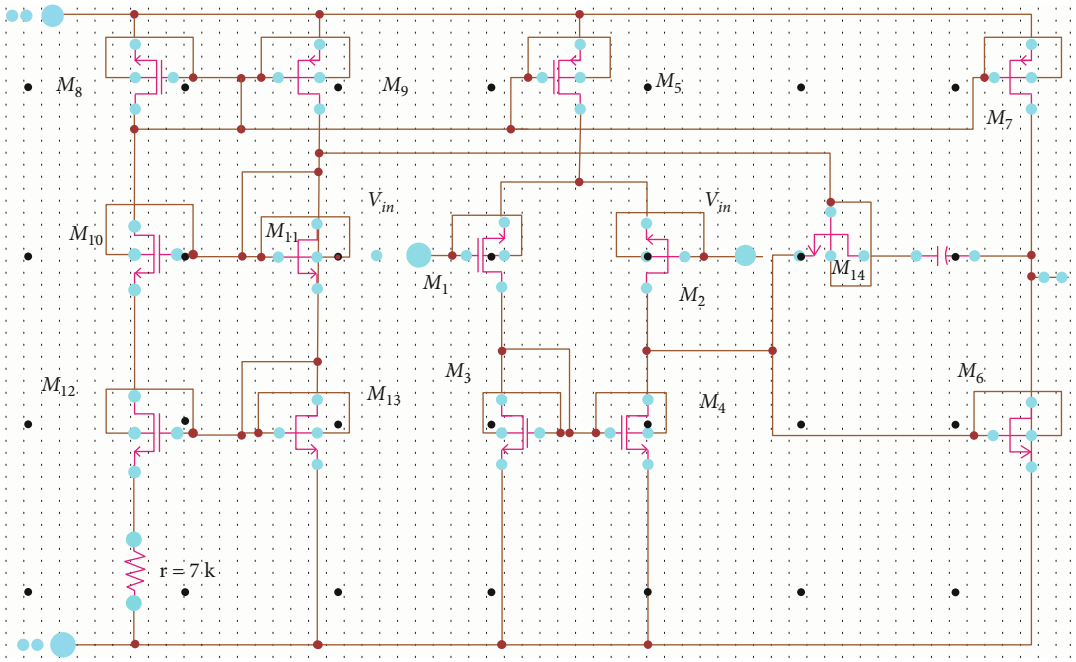

Figure 6: Two-stage differential amplifier block diagram.

applications. Both FinFETs and trigate are frequently seen as belonging to a larger category of devices known as multigate devices. The term trigate is that the channel has gates on three sides of it out of four, whereas FinFET is one of the tri-gate implementations. The orientation in the paper is to elevate the tri-gate-based device.

4. Two-Stage Operational Amplifier Design

Electromagnetic interference (EMI) caused by electronic devices increases noise in the analogue circuit. Because of its low electromagnetic interference capabilities, the OP-Amp is widely used in analogue and mixed-signal systems. Though EMI is added to the input signal and fed into the OP-Amp as an input, its output is either boosted as a common-mode component or rejected as a differential mode component. FinFET can be used instead of tiny CMOS to create an OP-Amp with high gain and low power especially, suitable for design of two-stage operational amplifier because FinFET-based two-stage operational amplifiers give enhanced performance at high voltage and a remarkable great performance at lower supply voltage compared to conventional MOSFET-based two-stage operational amplifiers.

The device's analogue performance is improved through the use of geometrical structure design to acquire optimum parameters [30]. Table 2 shows that subthreshold slope (SS), unity gain frequency, output conductance (g_d), intrinsic gain (A_{VO}), transconductance (g_m), and output resistance (R_O) are among the analogue optimal parameters' equations.

A differential amplifier is followed by a common source polymer-based amplifier in the two-stage OP-Amp, which improves gain and strengthens the output voltage swing. Differential amplifier generates a differential voltage between the inverting and noninverting terminals, which is amplified by the differential amplifier. The differential signal, which is fed as input to the current mirror circuit to create single-ended output voltage, provides active loads to the RF circuit. To improve the amplification, the common source amplifier is used as a buffer. With the help of a biasing circuit, all of the transistors operate in the saturation area. To run the OP-Amp with great stability and over a wider frequency range, a compensating circuit is used [31] as displayed in Figure 6.

Small signal analysis of a differential amplifier includes NMOS (M1 and M2) as the first stage's inverting and noninverting terminals and NMOS (M3 and M4) as the active load. A_{v1} is the voltage gain of the first stage of a differential amplifier. The common source amplifier for gain (A_{v2}) is used in the second stage, with an active load of NMOS (M6) and NMOS (M7) transistors.

$$\begin{aligned} A_{v1} &= G_{m1}R_1 = g_{m2}(r_{o2}\|r_{o4}), \\ A_{v2} &= -g_{m6}(r_{o6}\|r_{o7}). \end{aligned} \tag{5}$$

And the product of the first and second stages is the overall voltage gain:

$$A_0 = A_{v1}A_{v2} = -g_{m2}g_{m6}\,(r_{o2}\|r_{o4})(r_{o6}\|r_{o7}). \tag{6}$$

In the first stage, the total capacitance is (C_1), and in the second stage, the total capacitance is (C_2):

$$\begin{aligned} C_1 &= C_{GD2} + C_{DB2} + C_{GD4} + C_{DB4} + C_{GS6}, \\ C_2 &= C_{DB6} + C_{DB7} + C_{GD7} + C_L. \end{aligned} \tag{7}$$

To build a shunt feedback loop using the Miller capacitance, the drain of the NMOS (M6) transistor is linked to

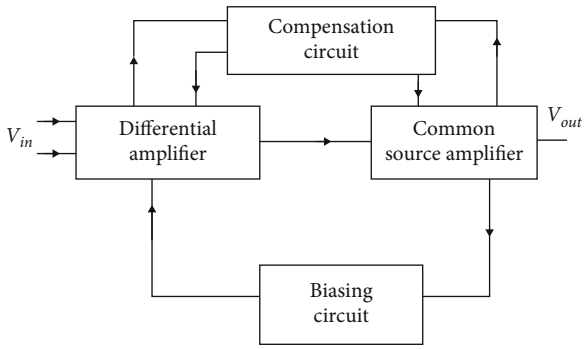

Figure 7: Two-stage differential amplifier design using FinFET.

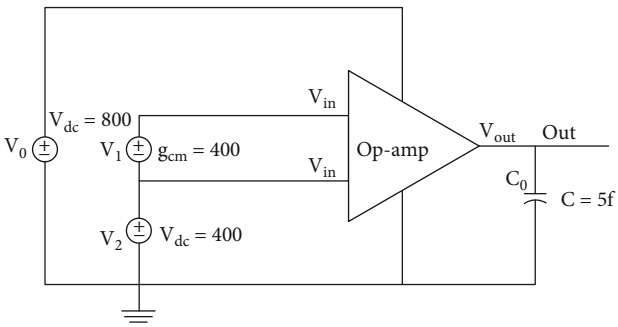

Figure 8: Two-stage OP-Amp with gain enhancement AC analysis.

the gate of the NMOS (M6) transistor (CC). For high-frequency operations, the feedback loop boosts stability. The dominating pole is calculated by combining the first and second stages of total capacitances. The frequency performance at first (f_d) and second poles (f_2) is as follows:

$$f_d = \frac{1}{2\pi R_1[C_1 + C_C(1 + g_{m2}R_2)]},$$
$$f_2 = \frac{G_{m2}C_c}{2\pi(C_1C_2 + C_1C_C(1 + C_2C_C))}. \quad (8)$$

The gain bandwidth product (GBW) at the first stage is expressed as

$$G_{\mathrm{BW}} = A_0 * f_d = \frac{G_{m1}}{C1} = \frac{1}{2\pi C_C}\mu_n C_{\mathrm{ox}}\left(\frac{W}{L}\right). \quad (9)$$

Miller capacitance (CC) increase is thought to aid in achieving improved stability and lowering the gain bandwidth product. Nonetheless, as compared to standard CMOS, the transconductance (g_m) of nano FinFET is high, resulting in better gain bandwidth and unity gain frequency. The two-stage differential FinFET OP-Amp has three phases, namely, the differential phase, common source gain phase, and biasing phase. FinFETs have turned the differential input signal into a single-ended output signal in the first phase (M1-M5). Noninverting and inverting FinFET gate terminals are M1 and M2, respectively. The differential phase gain determines how much the single-ended output is amplified. This phase gain is based on specific transconductance around the M1 FinFET, and it outputs total resistance to the M2 FinFET's drain terminal. The M3 and M4 FinFETs work as active load, single-ended conversion, and CMMR management by acting as a current mirror. The M5 FinFET is used to keep the differential pair's bias constant.

The common source gain phase amplifies the signal from the M2 FinFET using a common source M6 FinFET. This phase's active load will be transistor M7. The gain of the phase is determined by the specific transconductance around M6 FinFET and the total output load resistance toward M6 and M7. The gain improvement is achieved by giving output bias current to M6 and M7 FinFETs. With an active load inverter, this phase acts as a current sink. During the biasing phase, the M8-M13 FinFET transistors are used in current mirror architecture to provide a biasing network and also serve as a current source for the remarkable M5 and M7 FinFET transistors. The current sink for this phase will be the FinFET M5 plus M7 as illustrated in Figure 7.

In the RF region of operation, stray capacitances in the circuit generate an undesired phase shift, which makes the network unstable and difficult to remove. A frequency compensated capacitor (C0) is a series connected to the negative feedback network to maintain steady operation as illustrated in Figure 8. In a closed-loop design, an extra pole is formed during the amplification stage. As a result, if the dominating pole is greater than the new pole location, the phase falls. The C0 capacitor is a capacitor that rejects the effects of poles. To maintain good stability, an RC Miller adjusted circuit is used. The frequency response associated with gain enhancement technique is shown in the diagram below. It was discovered that the gain is 23 dB and that the frequency of unity gain is 5.07 GHz.

5. Results and Discussions

From Figure 9, it can be noticed that the phase has risen to 180 degrees, as can be seen. The RC compensated circuit can boost the unity gain bandwidth by increasing the bias current. When operating at 5 GHz, the circuit consumes a total of 537.1 μW.

The differential polymer-based amplifier is built using 16 nm FinFET technology, and its performance is compared to that of traditional MOSFETs. Using 16 nm FinFET technology, the overall gain increased to 22.7%. The FinFET's strong gm boosts the gain by a significant amount. The operational amplifier's unity gain frequency is 5 GHz, thanks to FinFET technology. FinFET minimizes power dissipation by 31.48% when compared to the reference circuit and provides an ideal bandwidth range. Using a 16 nm FinFET with a constant current bias and current mirror circuit, the CMRR was enhanced to 12.72%. When compared to ordinary MOSFETs, the FinFET OP-Amp produces better results. FinFET technology outperforms CMOS technology in terms of gain and unity gain frequency. The frequency of unity gain is 5.07 GHz, which is suitable for RF models. The same can be concluded by observing Table 3. This proposed novel model also provides scope for cost effective chip

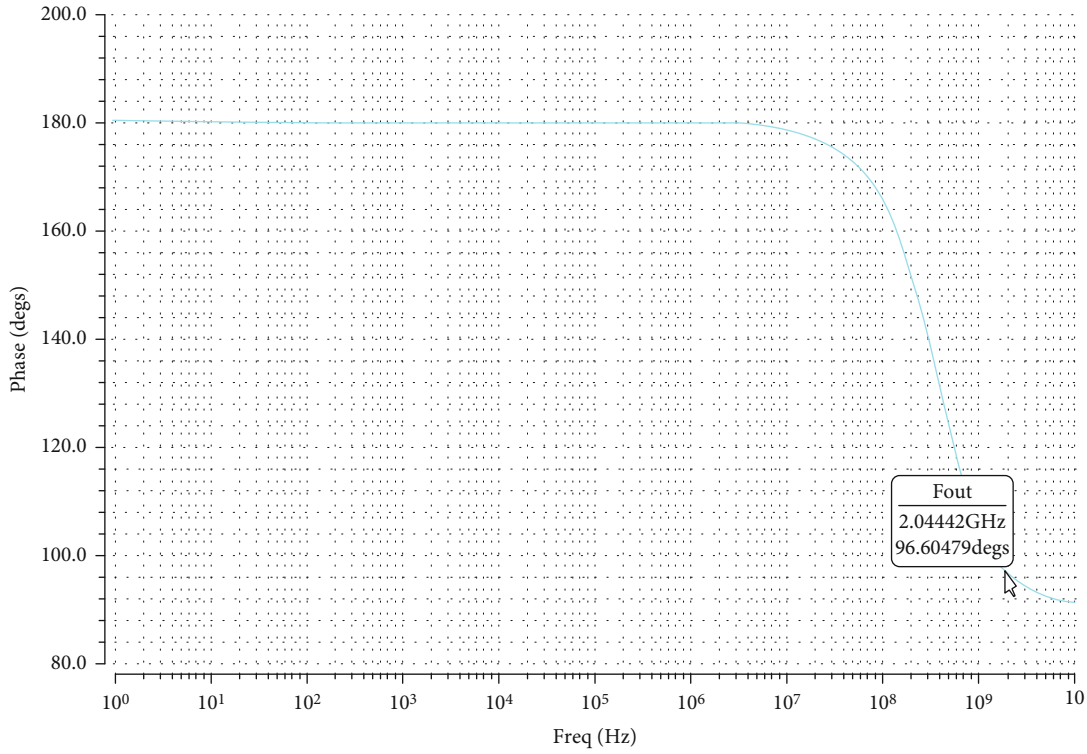

Figure 9: Phase plot of FinFET two-stage OP-Amp.

Table 3: Comparison table of polymer-based two-stage differential OP-Amp with CMOS and FinFET technology.

Parameter	Ref. [32]	Ref. [12]	Proposed method
Technology node	16 nm FinFET	30 nm CMOS	16 nm FinFET
Mode of operation	Saturation	Saturation	Saturation
VDD (V)	0.9	1.8	1
Gain (dB)	19.3	61.7	23.7
Unity gain frequency (GHz)	2.47	0.475	5.07
Power consumption (μW)	784	1258	537.1
CMRR (dB)	68	64.2	76.67

design, especially for low power, high speed, and area efficient applications.

6. Conclusions and Future Scope

CMOS scaling has emerged as the most important predictor of silicon technology advancement in terms of improving performance and incorporating more functions into a chip. The goal of this research was to develop a three-dimensional polymer-based trigate FinFET and a circuit utilizing the implemented compact model. FinFET is a three-dimensional structure that conducts channels around a vertical fin in three facets to improve driving current and functions as totally depleted for superior performance. With rising HFin, both I_{ON} and I_{OFF} increase. Because of its low electromagnetic interference capabilities, the OP-Amp is widely used in analogue and mixed-signal systems. With its 16 nm predictive technology model (PTM) FinFET, it is building a high gain and low-power FinFET polymer-based two-stage OP-Amp. Create a TCAD SPICE file with the FinFET device in it. The SPICE file has a lookup table-based model of the TCAD device. The design outperforms the CMOS by 22.7% in gain, 31.48% in power consumption, and 12.72% in CMRR, while operating at a 5 GHz unity gain frequency. Process variation in multigate devices is another issue that needs to be addressed in order to achieve device performance. The performance of the planned underlap FinFET is less immune to interdevice variability and parametric fluctuations, and it has better electrostatic integration (EI). In the future, new architectures such as negative capacitance, FETs that operate in the terahertz frequency range, and entirely depleted SOI for quantum computing are planned. As a result, greater gains in gate control over lower V_{DD} can be obtained.

Data Availability

There is no data availability statement for this manuscript.

Conflicts of Interest

The authors declare that they have no conflicts of interest.

References

[1] A. Razavieh, P. Zeitzoff, and E. J. Nowak, "Challenges and limitations of CMOS scaling for FinFET and beyond architectures," *IEEE Transactions on Nanotechnology*, vol. 18, pp. 999–1004, 2019.

[2] N. Boukortt, T. Lenka, S. Patanè, and G. Crupi, "Effects of varying the fin width, fin height, gate dielectric material, and gate length on the DC and RF performance of a 14-nm SOI FinFET structure," *Electronics*, vol. 11, no. 1, p. 91, 2022.

[3] A. Dixit, P. K. Kori, C. Rajan, and D. P. Samajdar, "Design principles of 22-nm SOI LDD-FinFETs for ultra-low-power analog circuits," *Journal of Electronic Materials*, vol. 51, no. 3, pp. 1029–1040, 2022.

[4] V. B. Sreenivasulu and V. Narendar, "A comprehensive analysis of junctionless tri-gate (TG) FinFET towards low-power and high-frequency applications at 5-nm gate length," *SILICON*, vol. 14, no. 5, pp. 2009–2021, 2022.

[5] R. K. Sharma, C. A. Dimitriadis, and M. Bucher, "A comprehensive analysis of nanoscale single- and multi-gate MOSFETs," *Microelectronics Journal*, vol. 52, pp. 66–72, 2016.

[6] A. Es-Sakhi and M. Chowdhury, "Analysis of device capacitance and subthreshold behavior of tri-gate SOI FinFET," *Microelectronics Journal*, vol. 62, pp. 30–37, 2017.

[7] N. E. Boukortt, B. Hadri, A. Caddemi, G. Crupi, and S. Patane, "Temperature dependence of electrical parameters of silicon-on-insulator triple gate N-channel fin field effect transistor," *Transactions on Electrical and Electronic Materials*, vol. 17, no. 6, pp. 329–334, 2016.

[8] K. P. Pradhan, S. K. Mohapatra, and P. K. Sahu, "Impact of channel and metal gate work function on GS-DG MOSFET: a linearity analysis," *ECS Journal of Solid State Science and Technology*, vol. 4, no. 9, pp. 393–P397, 2015.

[9] Philippe and P. Reynaert, "24.7 a 15dbm 12.8%-PAE compact D-band power amplifier with two-way power combining in 16nm FinFET CMOS," in *2020 IEEE International Solid-State Circuits Conference - (ISSCC)*, San Francisco, CA, USA, 2020.

[10] G. A. T. Sevilla, J. P. Rojas, H. M. Fahad et al., "Flexible and transparent silicon-on-polymer based sub-20 nm non-planar 3D FinFET for brain-architecture inspired computation," *Advanced Materials*, vol. 26, no. 18, pp. 2794–2799, 2014.

[11] C. Liao, M. Zhang, L. Niu, Z. Zheng, and F. Yan, "Organic electrochemical transistors with graphene-modified gate electrodes for highly sensitive and selective dopamine sensors," *Journal of Materials Chemistry B*, vol. 2, no. 2, pp. 191–200, 2014.

[12] R. Sonkusare, P. M. Pilankar, and S. S. Rathod, "Analysis of subthreshold SOI FinFET based two stage OTA for low power," *Analog Integrated Circuits and Signal Processing*, vol. 98, no. 2, pp. 277–289, 2019.

[13] V. Narendar and R. A. Mishra, "Analytical modeling and simulation of multigate FinFET devices and the impact of high-k dielectrics on short channel effects (SCEs)," *Superlattices and Microstructures*, vol. 85, pp. 357–369, 2015.

[14] S. P. Jani, A. S. Jose, C. Rajaganapathy, and M. A. Khan, "A polymer resin matrix modified by coconut filler and its effect on structural behavior of glass fiber-reinforced polymer composites," *Iranian Polymer Journal*, vol. 31, no. 7, pp. 857–867, 2022.

[15] G. Saini and S. Choudhary, "Asymmetric dual-K spacer trigate finfet for enhanced analog/RF performance," *Journal of Computational Electronics*, vol. 15, no. 1, pp. 84–93, 2016.

[16] A. B. Sachid, M.-C. Chen, and C. Hu, "Bulk FinFET with low-k spacers for continued scaling," *IEEE Transactions on Electron Devices*, vol. 64, no. 4, pp. 1861–1864, 2017.

[17] S. K. Mohapatra, K. P. Pradhan, D. Singh, and P. K. Sahu, "The role of geometry parameters and fin aspect ratio of sub-20nm SOI-FinFET: an analysis towards analog and RF circuit design," *IEEE Transactions on Nanotechnology*, vol. 14, no. 3, pp. 546–554, 2015.

[18] N. Boukortt, B. Hadri, S. Patanè, A. Caddemi, and G. Crupi, "Investigation on TG N-FinFET parameters by varying channel doping concentration and gate length," *SILICON*, vol. 9, no. 6, pp. 885–893, 2017.

[19] E. Yu, K. Heo, and S. Cho, "Characterization and optimization of inverted-T FinFET under nanoscale dimensions," *IEEE Transactions on Electron Devices*, vol. 65, no. 8, pp. 3521–3527, 2018.

[20] T.-K. Chiang, "A new threshold voltage model for short-channel junctionless inverted T-shaped gate FETs (JLITFET)," *IEEE Transactions on Nanotechnology*, vol. 15, no. 3, pp. 442–447, 2016.

[21] K. Zhang, Y. Liu, H. Zhu, C. Zhao, T. Ye, and H. Yin, "Doping profile optimisation in bulk FinFET channel and source/drain extension regions for low off-state leakage," *International Journal of Nanotechnology*, vol. 12, no. 1/2, p. 111, 2015.

[22] C.-J. Sun, M.-J. Tsai, S.-C. Yan et al., "Low Ge content ultra-thin fin width (5nm) monocrystalline SiGe n-type FinFET with low off state leakage and high I_{ON}/I_{OFF} ratio," *IEEE Journal of the Electron Devices Society*, vol. 8, pp. 1016–1020, 2020.

[23] H. Chakrabarti, R. Maity, and N. P. Maity, "Analysis of surface potential for dual-material-double-gate MOSFET based on modeling and simulation," *Microsystem Technologies*, vol. 25, no. 12, pp. 4675–4684, 2019.

[24] N. P. Maity, R. Maity, S. Dutta et al., "Effects of hafnium oxide on surface potential and drain current models for subthreshold short channel metal–oxide–semiconductor-field-effect-transistor," *Transactions on Electrical and Electronic Materials*, vol. 21, no. 3, pp. 339–347, 2020.

[25] H. R. Khan, D. Mamaluy, and D. Vasileska, "Simulation of the impact of process variation on the optimized 10-nm FinFET," *IEEE Transactions on Electron Devices*, vol. 55, no. 8, pp. 2134–2141, 2008.

[26] A. Razavieh, P. Zeitzoff, D. E. Brown, G. Karve, and E. J. Nowak, "Scaling challenges of FinFET architecture below 40nm contacted gate pitch," in *2017 75th Annual Device Research Conference (DRC)*, South Bend, IN, 2017.

[27] Z. Ramezani and A. A. Orouji, "Improving self-heating effect and maximum power density in SOI MESFETs by using the hole's well under channel," *IEEE Transactions on Electron Devices*, vol. 61, no. 10, pp. 3570–3573, 2014.

[28] Z. Sun, Z. Yu, Z. Zhang et al., "Investigation on the lateral trap distributions in nanoscale MOSFETs during hot carrier

stress," *IEEE Electron Device Letters*, vol. 40, no. 4, pp. 490–493, 2019.

[29] A. B. Sachid, M.-C. Chen, and C. Hu, "FinFET with high-κ spacers for improved drive current," *IEEE Electron Device Letters*, vol. 37, no. 7, pp. 835–838, 2016.

[30] R. A. Thakker, M. Srivastava, K. H. Tailor et al., "A novel architecture for improving slew rate in FinFET-based op-amps and OTAs," *Microelectronics Journal*, vol. 42, no. 5, pp. 758–765, 2011.

[31] Y.-G. Liaw, W.-S. Liao, M.-C. Wang et al., "A high aspect ratio silicon-fin FinFET fabricated upon SOI wafer," *Solid-State Electronics*, vol. 126, pp. 46–50, 2016.

[32] E.-S. H. Hesham and H. F. Hamed, "Design procedure for two-stage CMOS Opamp using GM/ID design methodology in 16 nm FinFET technology," in *2019 31st International Conference on Microelectronics (ICM)*, Cairo, Egypt, 2019.